Universidad de Burgos
Departamento de Ingeniería Civil

Royal Military Academy
Department Weapon Systems & Ballistics

IMPROVEMENT OF THE ROBUSTNESS OF BALLISTIC HELMETS TO RIFLE AMMUNITION

Angel MIRANDA-VICARIO

Brussels, November 2019

UNIVERSIDAD DE BURGOS
DEPARTAMENTO DE INGENIERÍA CIVIL

ROYAL MILITARY ACADEMY
DEPARTMENT WEAPON SYSTEMS & BALLISTICS

IMPROVEMENT OF THE ROBUSTNESS OF BALLISTIC HELMETS TO RIFLE AMMUNITION

Author:
ANGEL MIRANDA-VICARIO

Dissertation submitted to the Universidad de Burgos (Spain) and the Royal Military Academy (Belgium) for the degree of Doctor in Engineering Sciences

Thesis Directors:
PEDRO MIGUEL BRAVO DÍEZ
FREDERICK COGHE

Brussels, November 2019

A mis padres, Ángel y María Rosa

ACKNOWLEDGEMENTS

This research was done within the framework of the DYMASEC – DYnamic MAterial Behaviour and SECurity applications – research pole of the Royal Military Academy, Brussels, Belgium, and funded by the Department for Scientific and Technological Research of Defence of the Belgian Armed Forces (study DY-10) with the collaboration of the University of Burgos, Spain.

I would like to express my gratitude to all the people of both Departments involved in this project and specially my fellow colleagues from the ABAL laboratory.

I would like to thanks also all the people that concurred to make possible this text.

IMPROVEMENT OF THE ROBUSTNESS OF BALLISTIC HELMETS TO RIFLE AMMUNITION

Abstract

The ballistic protection of the head through the helmets is lower than the protection available for the rest of the body, despite the great importance for the survival of the user. This is due to the significant weight limitations the head and neck can withstand, as well as the fragility of the skull and brain; that reduce the load they can bear. This has been an impassable barrier that has caused the helmets worn by police and armies around the world to only be able to safely stop pistol bullets. Rifle bullets have much more penetration capacity due to their shape, kinetic energy and materials; and this type of threat is becoming more common due to the changes taking place in the various theatres of operations. This makes a thorough study of the problem necessary to improve the safety and security of users.

The difficulty lies in stopping a projectile that possesses about four times more kinetic energy with minimal variation in hull weight. Since this parameter influences not only the comfort but also the mobility of the user. Stopping the projectile is only the first step, as it is necessary to ensure the survival of the user from the direct and indirect loads of the hull and the deformation produced by the impact.

In this work, the light weight ballistic protections are studied in order to mature a prototype helmet capable of stopping rifle bullets, an analysis is made of the charges suffered by a head when it carries a helmet and is hit by a pistol bullet; to finally study how to reduce the ballistic charge produced by the impact of a rifle projectile to acceptable values.

Resumen

La protección balística de la cabeza a través de los cascos presenta un nivel inferior con respecto a la protección disponible para el resto del cuerpo, a pesar de la gran importancia de esta para la supervivencia del usuario. Esto es debido a las importantes limitaciones de peso que puede soportar, así como a la fragilidad del cráneo y cerebro, siendo una barrera infranqueable que ha causado que los cascos usados por la policía y los ejércitos de todo el mundo solo sean capaces a de detener de manera segura balas de pistola. Las balas de rifles tienen mucha más capacidad de penetración debido a su forma, energía cinética y

materiales; y este tipo de amenaza es cada día más común debido a los cambios que se producen en los diversos teatros de operaciones. Esto hace acuciante un estudio pormenorizado del problema para mejorar la protección y seguridad de los usuarios.

La dificultad reside en detener un proyectil que posee unas cuatro veces más de energía cinética con la mínima variación del peso del casco. Ya que este parámetro no solo influye en el confort sino también en la movilidad del usuario. Detener el proyectil, es solo el primer paso, ya que hay que asegurar la supervivencia del usuario de las cargas, directas e indirectas, del casco y de la deformación producida por el impacto.

En este trabajo se estudian las protecciones balísticas ligeras con las que se podrían hacer un prototipo de casco capaz de detener balas de rifle, se hace un análisis de las cargas que sufre una cabeza cuando porta un casco y es impactada con una bala de pistola; para finalmente estudiar la manera de reducir la carga balística producida por el impacto de un proyectil de rifle hasta valores aceptables.

Keywords: Ballistics, projectiles, deformation, shock absorber

CONTENT

LIST OF TABLES

LIST OF FIGURES

LIST OF SYMBOLS

A	Area
a	Acceleration
C_d	Average drag coefficient
C_L	Wave's velocity
δ	Armour areal density
D	Diameter of the projectile
E	Young modulus
E_k	Kinetic energy
erf	error function
F	Force
L	Length of the projectile
m	Mass
m_p	Projectile mass
P	Pressure
$P_b(V_s)$	DOP into unprotected backing
P_s	Residual DOP into the protected backing
S	Constant tension
T	Time
t	Thickness
T_{Dwell}	Dwell time
U	Figure of merit
v	Volume
V	Velocity
V_{50}	Ballistic resistance
Vi	Projectile velocity at the target
Vs	Projectile velocity at the point of measurement
X	Distance
Z	Acoustic impedance
Z_1	Impedance of the first material
Z_2	Impedance of the second (baking) material
ΔL	Deformation of the projectile

γ	Rake angle
δ	Areal density
ε	Strain
ε_f	Fracture strain
εr	Failure strain of the backing
η	Ballistic efficiency
μ	Average
ρ	Density
ρ_b	Density of the backing
ρ_c	Density of the ceramic
σ	Standard deviation
σ_f	Fracture strength

LIST OF ABBREVIATIONS

ACH	Advanced Combat Helmet
AEP	Allied Engineering Publication
AIS	Abbreviated Injury Scale
AK	Automat Kalashnikov
AlN	Aluminium Nitride
AP	Armor Piercing
APR	General Test Guideline (Allgemeine PrüfRichtlinie)
ASTM	American Society for Standard and Materials
B_4C	Boron Carbide
BABT	Behind Armour Blunt Trauma
BHBT	Behind Helmet Blunt Trauma
BC	Blunt Object Skull Fracture Criterion
BFD	Back Face Deformation
BFS	Back Face Signature
BLSH	Ballistic Load Sensing Head form
CB	Coned Bullet
CDF	Cumulative Distribution Function
CENIEH	Research Nacional Centre Of Human Evolution (CEntro Nacional de Investigación de la Evolución Humana)
CIP	Permanent International Commission For The Testing Of Small Arms
CMC	Ceramic-Metal Composite Materials
CMM	Coordinate Measuring Machine
CNT	Carbon Nanotubes
CSiC	Ceramic Bonded Sic
CT	Computed Tomography
DIC	Digital Image Correlation
DOP	Deep Of Penetration
EASC	Euro-Asian Council for Standardization, Metrology and Certification
ECH	Enhanced Combat Helmet
EUROPOL	European Police
FMJ	Full Metal Jacket

FMJ*	Full Metal Jacket - Copper
FMs	Full Brass
FN	Flat Nose
fps	Frames Per Second
FSP	Fragments Simulating Projectile
GEF	Spanish Fracture Group
	(Grupo Español de la Fractura)
GOST	Russian state standard
	(GOsudarstvennyy STandart)
HC	Hard core
HIC	Head Injury Criterion
HIPSiC	Hot – Isostatic Pressed
HOSDB	Home Office Scientific Development Branch
HPSiC	Hot – Pressed Sic
I	Incendiary
ICRC	International Committee of The Red Cross
IRC	Intensity Reflection Coefficient
ISB	International Symposium on Ballistics
ITC	Intensity Transmission Coefficient
JSP	Jacketed Soft Point
K	Handgun
L	Full Lead
L*	Rifle
LPSSiC	Liquid Phase Sintered Sic
LRHV	Long Rifle High Velocity
LWAG	Light Weight Armour Group for Defense and Security
MC	Mild-Steel Core
NATO	North Atlantic Treaty Organisation
NIJ	National Institute Of Justice
PADP	Polyetherdiol-Aliphatic Diisocyanate Polyurethane
PASGT	Personal Armor System Ground Troop
PASS	Personal Armour System Symposium
PB	Pointed Bullet
PBO	Poly (P- Phenylene-2.6-Benzobisoxazole)

PPE	Personal Protection Equipment
PUR	Polyurethane
RN	Round Nose
RW	Rigid steel wall
SC	Lead-Soft Core
SCP	Lead-Soft Core Steel Penetrator
SEM	Scanning Electron Microscope
SIALON	Silicon Aluminium Oxynitride
SB_4C	Solid – State Sintered Boron Carbide
SiC	Silicon Carbide
SiSiC	Infiltrated SiC
SN	Silicon Nitride
SSiC	Solid – State Sintered SiC
STANAG	Standard NATO Agreement
SWC	Semi-Wadcutter
TBI	Traumatic Brain Injury
TDCC	Dimension Sheets Of The CIP
TiB_2	Titanium Boride
UHWMPE	Ultra-High-Molecular-Weight Polyethylene
UK	United Kingdom
USA	United States of America
VPAM	Association Of Test Laboratories For Bullet Resistant Materials And Construction (Vereinigung Der Prüfstellen Für Angriffshemmende Materialien Und Konstruktionen)
WC	Wolfram-Carbide

1 INTRODUCTION

1.1 Structure of the thesis

In the first chapter, Introduction, there is an explanation of the problem and the objectives of the research project. The research is developed around three main steps:

- Study of ballistic impact into an actual helmet.
- Upgrade and optimise armour to defeat rifle ammunition.
- Analyse of the load of the user for the upgrade solution.

2nd chapter reviews the standards and evolution of the ballistic protection for small calibres.

3rd chapter describes the light material used for ballistic protection, regarding their position in the armour.

4th chapter describes the experimental techniques used for the research and a description of the main machines.

5th chapter is the first of the three chapters that introduces the experimentation done along with the research. It presents the results of the investigation, along with the discussion, of the study of the load (in terms of force and acceleration) suffered by the head while a pistol projectile impacts into a helmet. An actual helmet of the Belgian army is going to be fired with pistol ammunition and checked the response of the head surrogates. Main novelties are the assessment of the ballistic impacts into helmets that allows the estimation of force threshold and could make easier to relate with an injury criteria.

6th chapter studies lightweight armour materials to defeat the projectile and to reach the project objectives. Main innovations are the extension of the impact velocity range of mild steel projectiles onto rigid wall beyond the linear behaviour and the study of the impacts of mild steel projectiles into thin ceramics.

7th chapter studies the load (in terms of force and acceleration) suffered by the head while a rifle projectile impacts into the optimised solution. Main novelty is to study a helmet liner to improve the survivability of the helmet user after a rifle impact.

8th and last chapter sums up the conclusions of the research and outlines the future work needed to improve this research and side unresolved questions.

Results and different aspects of the research were published in one journal and several conference proceedings:

Journal:

A. Miranda-Vicario, P. M. Bravo, and F. Coghe, "Experimental study of the deformation of a ballistic helmet impacted with pistol ammunition", Composite Structures, vol. 203, pp. 233–241, Nov. 2018.

Proceedings:

A. Miranda-Vicario, A. Azevedo, F. Coghe, and M. Pirlot; "Experimental testing of different armour configurations for the development of a new ballistic helmet", in Proceedings of the Light Weight Armour Group for Defense and Security (LWAG 2013).

A. Azevedo, A. Miranda-Vicario, F. Coghe and F. Teixeira-Dias; "Modeling of the ballistic behaviour fo Dyneema HB26 and HB80 Using LS-DYNA" in Proceedings of the Light Weight Armour Group for Defense and Security (LWAG 2013).

A. Miranda-Vicario, A. Azevedo, F. Coghe, J. Matos, and M. Pirlot; "Experimental and numerical testing of different armour configurations for ballistic helmets" in Proceedings of the Personal Armour System Symposium (PASS 2014).

A. Miranda-Vicario, A. Azevedo, F. Coghe; "Different armour configurations for the development of personal protective equipment" in Proceedings of the Light Weight Armour Group for Defense and Security (LWAG 2014).

A. Azevedo, A. Miranda-Vicario, F. Coghe, F. Teixeira-Dias and J. Matos; "Validation of a numerical model for helmet testing with a clay head form", in Proceedings of the Personal Armour System Symposium (PASS 2016).

A. Miranda-Vicario, A. Azevedo, and F. Coghe; "Experimental and numerical study of the deformation of mild steel core ammunition", in Proceedings of the Personal Armour System Symposium (PASS 2016).

A. Azevedo, A. Miranda-Vicario, F. Coghe and F. Teixeira-Dias; "Numerical evaluation of the feasibility of a novel ballistic helmet", in Proceedings of the 30th International Symposium on Ballistics (ISB 2017).

A. Miranda-Vicario; "Enhancement of ballistic helmet", IV Jornadas de doctorandos de la Universidad de Burgos. Universidad de Burgos (2017).

A. Miranda-Vicario, A. Azevedo, P.M. Bravo, F. Coghe; "Experimental and numerical comparison of methods for studying the deformation of a ballistic helmet impacted with pistol ammunition" in Proceeding of the Personal Armour System Symposium (PASS 2018).

A. Miranda-Vicario, P. M. Bravo, F. Coghe; "Experimental study of ballistic impacts into helmets", Grupo Español de la Fractura (GEF 2018).

A. Miranda-Vicario, P. M. Bravo, F. Coghe; "Estudio experimental: «BHBT» producido por amenaza balistica", VI Congreso Nacional de I+D en Defensa y Seguridad (2018).

A. Miranda-Vicario, P. M. Bravo, F. Coghe; "Experimental study of the deformation of crushable aluminium foam", Grupo Español de la Fractura (GEF 2019).

A. Azevedo, A. Miranda-Vicario, F. Coghe; "Numerical validation of a shock absorbing material for ballistic impacts" in Proceedings of the Light Weight Armour Group for Defense and Security (LWAG 2019).

1.2 Statement of the problem

Armour protection field is in a constant race to defeat the threat. For personal protection equipment, torso equipment has been able to keep up the pace, and they can defeat almost all kind of small calibre bullets. Limitation of existing protection measurements produces helmets only able to protect effectively from fragments produced by explosives devices. Head protection lacks efficiency regarding high-velocity ammunition due to the inherent constraints of a helmet. As a consequence of this limitation, it is necessary to upgrade the head protection because of the change of scenarios for the State security forces. Nowadays, people are mostly exposed to high-speed projectiles, such as rifle bullets. Newspapers show the impact of events where rifles are involved, from robberies to terrorist attacks. European Police (EUROPOL) pointed to the increase in incidents involving heavy firearms in the EU in 2011 (EUROPOL, 2011; Gobinet, 2011). Since more performant weaponry is more often faced, ballistic protection must be updated and adequate to these new requirements.

1.2.1 Weaponry & Projectiles

As pointed out in the previous point, there are more powerful weapons available on the black market, due to several factors as the widespread diffusion or the simplicity of these weapons. The numbers of weapons manufactured and active are not precise, because of the policy of the governments and producers, and the unlicensed production. Nevertheless, it is estimated that there are about 80 to 100 million of the Avtomat Kalashnikov (AK) series automatic rifles (Izhmash, Russia) officially in service in more than 80 countries. The ubiquity of this weapon is well-known. Firearms such as the Uzi (IMI Systems, Israel), M-16 Series (Colt's Manuf, USA) or the G3 (Hechler & Koch, Germany) all come in the second position of the ranking and are produced in lesser amounts (Small Arms Survey, 2001).

These weapons are designed to fire one of the following projectiles:

7.62 x 39 mm M43

This ammunition has a soft steel core (Figure 1.1) which gives it more penetration power than other soft material for hunting purposes. The jacket is made of steel as well as the core. Lead accommodates the core in the interior of the projectile. Its velocity is slower than the 5.56x45 mm ammunition (Table 1.1). AK series rifles use this ammunition.

Figure 1.1.- Ammunition of calibre 7.62 x 39 mm M43 and its core.

Projectile	**Bullet weight (g)**	**Core weight (g)**	**Muzzle velocity (m/s)**	**Muzzle energy, (J)**
7.62x39 mm M43	8	3.7	740	2150

Table 1.1.- Ammunition properties 7.62 x 39 mm M43.

5.56 x 45 mm NATO Ball (SS109)

The 5.56 x 45 mm projectile with a military designation of SS109 (NATO, 1993) has a steel tip and lead rear, and the jacket is made in acopper alloy (Figure 1.2). It is a light and fast projectile that makes high-performance ammunition (Table 1.2). The M-16 and other NATO countries rifles use this ammunition.

Figure 1.2.- Ammunition of calibre 5.56 x 45 mm NATO Ball - SS109.

Projectile	**Bullet weight (g)**	**Muzzle velocity (m/s)**	**Muzzle energy, (J)**
5.56 x 45 mm NATO Ball (SS109)	4	970	1750

Table 1.2.- Ammunition properties 5.56 x 45 mm NATO Ball - SS109.

9 x 19 mm Full Metal Jacket (FMJ)

Another ammunition very extended is the 9 x 19 mm Parabellum, a pistol round used by the majority of State security forces and bodies in Europe. The standard projectile is the FMJ consisting of a copper or brass jacket and a lead alloy core. Pistol and submachines guns use this ammunition, as Uzi (Table 1.3 and Figure 1.3).

Figure 1.3.- Ammunition of calibre 9 x 19 mm.

Projectile	Bullet weight (g)	Muzzle velocity (m/s)	Muzzle energy, (J)
9 x 19mm FMJ	7.45	360	480

Table 1.3.- Ammunition properties 9 x 19 mm.

Fragments Simulating Projectiles (FSPs)

The last type of projectile necessary for this research is the Fragments Simulating Projectiles (FSPs). They simulate fragments produce by any explosive device. Although current military helmets have been worn extensively during operations, they are only useful against fragmentation threats and checked against 1.1 g FSP (Figure 1.4). FSPs are defined in the standard NATO agreement, STANAG 2920. FSPs were developed for testing personal protection with excellent repeatability. They are scaled for different calibre (Table 1.4)

Figure 1.4.- FSP 1.1 g.

Projectile type	Weight (g)	Hardness Rockwell C
Calibre 5.56 mm (.22)	1.1 +- 0.03	30 +/- 1
Calibre 7.62 mm (.30)	2.84 +/- 0.03	30 +/- 1
Calibre 12.7 mm (.50)	13.39 +/- 0.13	30 +/- 1

Table 1.4.- Fragment Simulating projectiles properties.

1.2.2 Risk assessment

Whenever there is a ballistic impact on the body, extra attention should be paid to avoid head wounds. The International Committee of the Red Cross (ICRC) exposes the importance of protecting the head from ballistic impacts because injuries to the head are among the most lethal; they are among the most dangerous. The lethality of penetrating head wounds is roughly 75 %, and they account for almost 50 % of combat deaths, and about 8 % of survivors (ICRC, 2015).

A study gathered data on gunshots wounds among UK troops deployed overseas between 01 January 2009 and 31 December 2013 (Table 1.5): also shows that although the head represents a minor part of the exposed body surface area, it accounts for a disproportionate number of casualties (Penn-Barwell et al., 2016).

	Fatalities	**Survivors**	**All wounds**
Head	220 (26 %)	52 (6 %)	272 (16 %)
Total wounds	854	883	1737

Table 1.5.- Gunshots wounds for UK troops 2009/2013 (Penn-Barwell et al., 2016).

Head wounds kill either through distressing the brain or through asphyxiation of the unconscious patient who may endure the impact. The survivability in this kind of events is unlikely that even medical journals report these kinds of cases (Siccardi et al., 1991). Rammo et al express surprise of a case where a person survived a transcranial wound caused by rifle ammunition (Rammo et al., 2012).

The damage produced by penetrating bullets is related to the amount of energy delivered to the soft tissues (Stefanopoulos et al., 2014), although the armour can lead to injury the user after stopping a projectile. This effect, named Behind Armour Blunt Trauma (BABT), is due to the deformation of the armour and the energy spread into the body. It can produce severe damage, also being lethal even if the projectile has not perforated the shield. The object of the helmet is to prevent the BABT high load from damaging the skull (Rafaels et al., 2015a). Skull can support around 5000 N (Motherway et al., 2009, 2009; Raymond et al., 2009). Accelerations might also damage the brain, and this is due to the rotational effects causing large shear strains in the brain tissue (Holbourn, 1943).

An impacted helmet loads the head user in different ways (Figure 1.5). Any of the four effects lined at the bottom of the graph may produce burst, bending and skull fracture, local brain injury and diffuse brain injury. Three of the sources of injury are going to be addressed during this research except rotational acceleration because only orthogonal impacts were studied.

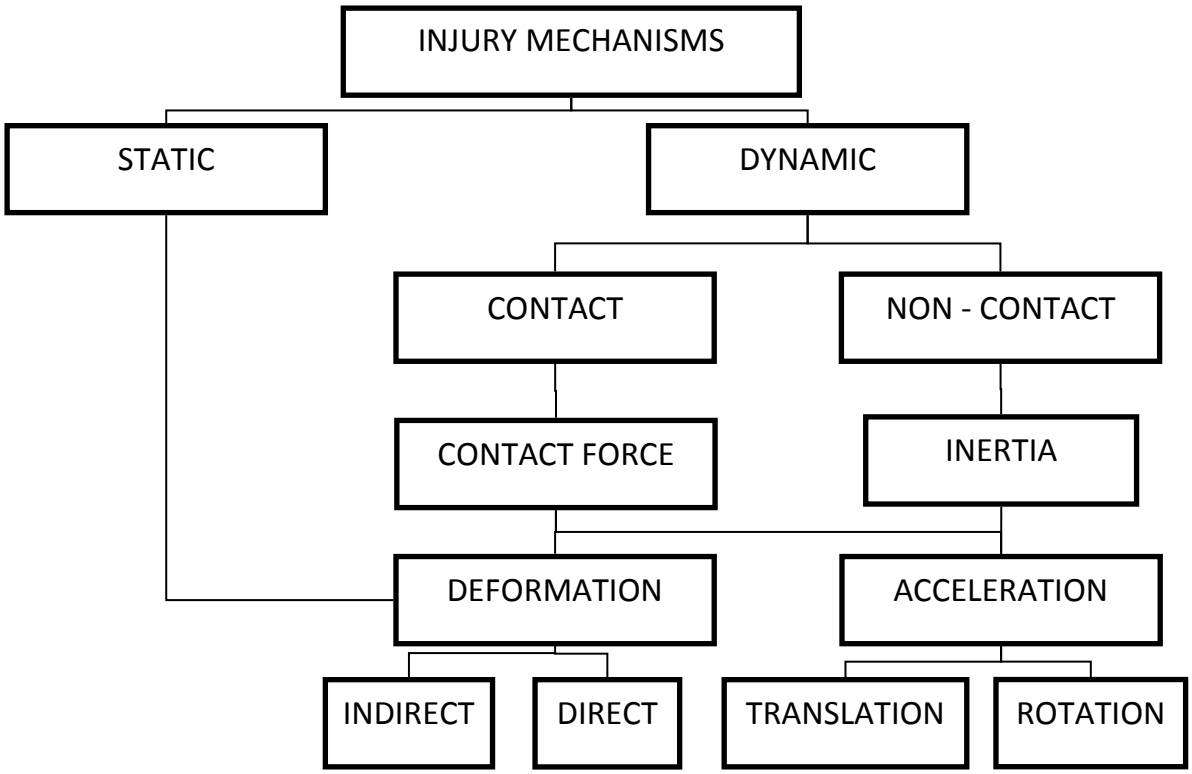

Figure 1.5.- Injury mechanisms with respect to blunt force in the head (Schmitt et al., 2014).

The ballistic resistance needed for defeating rifle ammunition is bulky and heavy. Nowadays, it is only available for torso protection. Regular helmets offer lower protection level, mostly for stopping explosion fragments or handguns projectiles. Therefore they are insufficient for facing the new threats. For all of these reasons, a helmet able to stop rifle rounds will be beneficial for police forces. It will allow them to be deployed safely and complete their tasks with lower risks.

1.3 Objectives

This research aims to prove the feasibility of a concept ballistic helmet capable of stopping a high-velocity projectile, coming from rifle ammunition. The prototype should also reduce the risk of injury and meeting a high standard of comfort.

There are three main criteria for developing the ballistic concept helmet: ballistic resistance, the total weight of the system, and limited damage to the user after an impact event.

The first step is to design a helmet able to stop the projectile at a nominal velocity of different weapons. The riskier ballistic threats are the Kalashnikov round (Table 1.6).

	Threat	**Ballistic resistance**
Primary goal	7.62x39 M43 (mild steel core)	V_{50} > 740 m/s
Secondary goal	7.62x39 Soviet M43 (mild steel core)	V_{50} > 640 m/s

Table 1.6.- Ballistic protection resistance objectives.

Secondly, it has to be light and comfortable. The actual helmet weighs around 1.7 kg (Willa, 1999). The objective is to design a helmet with similar weight specification than the current one (Table 1.7).

Primary goal	< 1.5 kg
Secondary goal	< 3.5 kg

Table 1.7.- Full mass of the helmet objectives.

Thirdly, the load suffered by the head user for non-perforating impacts will be determined. Several criteria have to be fulfilled to avoid injuries to the user. Different research shows that the average skull fracture happens at 5 kN. Therefore, it is needed to prevent contact between the helmet and the head. In case it is not possible the contact force between them should be smaller than 5 kN to limit skull fracture, and the Back Face Signature (BFS) shorter than 16 mm (Table 1.8). BFS is the indentation produced by the armour in the witness material; this parameter is commonly used for Personal Protection Equipment (PPE), such as vest and helmets.

Primary goal:	Avoid contact between helmet shell and skull	Fcontact = 0 N (BFS = 0 mm)
Secondary goal	Limit contact force between helmet shell and skull	Fcontact < 5kN

Table 1.8.- Risk of skull fracture objective.

Another source of injury is the risk of traumatic brain injury (TBI) mainly caused by the rapid acceleration of the head. Head Injury Criterion (HIC) is an adimensional value to assess the damage (Tse et al., 2016), although it is not intended for ballistic use (Table 1.9). Despite the fact that projectiles with a 45° impact angle cause higher strains on the brain tissue than other angles (Aare and Kleiven, 2007; Ghajari et al., 2013); only orthogonal impacts will be studied in this project.

Primary goal:	Limit accelerations to a minor injury	HIC15 < 500
Secondary goal:	Limit accelerations to moderate injury	HIC15 < 900
Additional goals:	Limit linear acceleration	< 400g

Table 1.9.- Risk of traumatic brain injury objectives.

In order to accomplish with the above considerations, the following goals were established for the present research:

1. Understand how the impact event loads affect the wearer of the helmet.
2. Study the interaction between the projectile and the armour, and characterise the defeat mechanisms.
3. Design through testing the material configuration of the helmet shield for rifle protection. Optimise taking into account the material properties and the limits set before.
4. Study through testing of the user loads for minimising the risk of injury for the best-selected configuration.

This research will be approached through the next stages to accomplish the previous goals:

- Study the load (in terms of force and acceleration) suffered by the head while a pistol projectile impacts into a helmet. An actual helmet of the Belgian army is going to be fired with pistol ammunition and checked the response of the head surrogates.
- Study how the armour defeats the projectile. Optimise the armour to achieve the previous objectives.
- Study the load (in terms of force and acceleration) suffered by the head while a rifle projectile impact into the optimise solution. Compare and reduce the levels to the previously obtained.

2 STATE OF THE ART

2.1 Level of ballistic protection

Level of ballistic protection is defined in several international standards which only covers a limited number of projectiles, those most often encountered. This is due to the enormous amount of projectiles available in the market and the reduction of expenditures when testing ballistic protection. Different countries have set up various references. For example, the USA, through the National Institute of Justice (NIJ), has established several standards as (National Institute of Justice, 1985b, 1985a, 2008). There is an NIJ standard for ballistic helmets currently under revision (National Institute of Justice, 1981). The Home Office Scientific Development Branch (HOSDB) of the UK Police produced some examples as Body armour Standard (Croft and Longhurst, 2007). And the German institution Vereinigung der Prüfstellen für Angriffshemmende Materialien und Konstruktionen (Association of test laboratories for bullet-resistant materials and construction, VPAM) wrote standard for general and head protection (VPAM, 2009, 2010). Details on different standards for ballistic protection are presented below.

2.1.1 NATO

NATO released in September 2016 the Allied Engineering Publication (AEP) standard AEP-2920: Procedure for the evaluation and classification of personal armour bullet and fragmentation threats (NATO, 2016) . The standard classified the threat with respect to the material of the projectile in 4 categories: lead core, mild steel core, hardened steel and tungsten cobalt cores. The hardness is also specify for each tipe of categories. A number relates with the caliber of the ammunition. The mild steel core 7.62 x 39 mm correspond to a B4 class (Table 2.1).

Category	Class	Calibre (mm)	Minimum Core Hardness (HRC)
A Lead Core projectiles	A1	9 x 19	-
	A2	4.6 x 30	-
	A3	5.56 x 45	-
	A5	7.62 x 51	-
	A Special	Emerging threat	
B Mild steel core projectiles	B2	4.6 x 30	40
	B3	5.56 x 45	40
	B4	7.62 x 39	40
	B5	7.62 x 51	40
	B Special	Emerging threat	
C Hardened steel core projectile	C4	7.62 x 39	60
	C5	7.62 x 51	60
	C6	7.62 x 54	60
	C7	7.62 x 63	60
	C Special	Emerging threat	
D Tungsten cobalt core projectile	D1	9 x 19	70
	D3	5.56 x 45	70
	D5	7.62 x 51	70
	D Special		

Table 2.1.- Classification of the protection levels for AEP 2920 .

2.1.2 USA

The NIJ standard 0101.06 established seven levels of armour protection, as seen in Table 2.2. Remarkable and popular ammunition and weaponry define these levels from the USA. The mild steel core 7.62 x 39 mm has no specific level in this clasification.

Armour Type	Test Ammunition	Nominal Bullet Mass (g)	Required Bullet Velocity (m/s)	Required Hits/ Armor Specimen	Permitted Penetrations
I	22 LRHV Lead	2.6	320 – 12	5	0
	38 Special RN Lead	10.2	259 – 15	5	0
II-A	357 Magnum JSP	10.2	381 – 15	5	0
	9 mm FMJ	8.0	332 – 12	5	0
II	357 Magnum JSP	10.2	425 – 15	5	0
	9 mm FMJ	8.0	358 – 12	5	0
III-A	44 Magnum Lead SWC Gas Checked	15.55	426 – 15	5	0
	9 mm FMJ	8.0	426 – 15	5	0
III	7.62 mm .308 Winchester FMJ	9.7	838 – 15	5	0
IV	30-06 AP	10.8	868 – 15	1	0
Special	These items must be specified by the user. All of the items must be specified				

Abbreviations: AP - Armor Piercing FMJ - Full Metal Jacket JSP - Jacketed Soft Point LRHV - Long Rifle High-Velocity RN - Round Nose SWC - Semi-Wadcutter

Table 2.2.- Classification of the protection levels for NIJ standard 0101.06 (National Institute of Justice, 2008).

The standards for head and torso protection explain the procedure to test and the back face deformation allowed to the armour. Once the level of protection is defined, all projectiles with similar characteristics would be presumably stopped by the armour; e.g. level III-A for all pistol and revolver ammunition. Threats used as reference are well-known and defined, but new projectile may appear able to defeat the ballistic protection intended for it. This case happened with FN ammunition 5.7 x 28 mm, SS 109 or 4.6 x 30 mm H&K ammunition. It can be fired from a pistol, but it could easily penetrate the level III-A ballistic protection. The solution given was to allow this weapon only for military use or only to allow selling less powerful ammunition.

2.1.3 UK

HOSDB (Home Office Scientific Development Branch), sited in the UK, works with various research centres, universities, academies and is in direct contact with the various industries that use body armour. HOSDB has developed on test standards for stab and bulletproof vests for the police in England since 1993. Classification of the protection levels has been updated and defines six levels of protection (Payne and O'Rourke, 2017). The mild steel 7.62 x 39 correspond to an HO3 (Table 2.3).

Protection level	**Classification**	**Test round designation**	**Velocity (m/s)**
HO1	9 mm FMJ	9 mm FMJ	365 +/- 10
	9 mm JHP	9 mm JHP	365 +/- 10
HO2	9 mm FMJ	9 mm FMJ	430 +/- 10
	9 mm JHP	9 mm JHP	430 +/- 10
HO3	Rifle 7.62	7.62 x 51 mm Ball	830 +/- 15
	Rifle 7.62	7.62 x 39 mm MSC	705 +/- 15
HO4	Rifle 7.62	.308 Win	820 +/- 15
SG1	Shotgun 12 gauge	Win	435 +/- 25
Special			
FMJ Full Metal Jacket JHP Jacketed Hollow Point MSC Mild Steel Core			

Table 2.3.- Classification of the protection levels for Body armour HOSDB Standard (Payne and O'Rourke, 2017).

2.1.4 Germany

The VPAM standard General Test Guideline (Allgemeine PrüfRichtlinie, APR) published on 2006 defines 14 levels of armour protection (Table 2.4). In this case, it even refers to the

manufacturer for assuring the same type of projectile used. This standard refers to European producers of ammunition that is the most common ammunition in Germany. The mild steel core 7.62 x 39 mm corresponds to a level 8.

Test level	**Type of weapon**	**Calibre**	**Ammunition and projectile**		**Test conditions**	
			Type	Mass (g)	Shot distance (m)	Bullet velocity (m/s)
1	K/L*	.22 Long Rifle	L/RN	2.6 ± 0.1	10 + 0.5	360 ± 10
2	K	9 mm Luger	FMJ / RN / SC , tinned	8.0 ± 0.1	5 + 0.5	360 ± 10
3	K	9 mm Luger	FMJ / RN / SC , tinned	8.0 ± 0.1	5 + 0.5	415 ± 10
4	K	.357 Magnum	FMJ / CB / SC	10.2 ± 0.1	5 + 0.5	430 ± 10
		.44 Rem. Mag.	FMJ (*) / FN / SC	15.6 ±0.1	5 + 0.5	440 ±10
5	K	.357 Magnum	FMs / CB	7.1 ± 0.1	5 + 0.5	580 ± 10
6	L*	7.62 x 39	FMJ / PB / MC	8.0 ± 0.1 (core 3.6)	10 + 0.5	720 ± 10
7	L*	.223 Rem.	FMJ / PB / SCP	4.0 ± 0.1	10 + .05	950 ± 10
		.308 Win.	FMJ / PB / SC	9.55 ± 0.1	10 + 0.5	830 ± 10
8	L*	7.62 x 39	FMJ / PB / HC I	7.7 ± 0.1 (core 4.1 hardness 65 HRC)	10 + 0.5	740 ± 10
9	L*	.308 Win.	FMJ / PB/ HC I	10.4 ± 0.1 (core 4.0 ± 0.1 hardness 62 ± 2 HRC)	10 + 0.5	860 ± 10
10	L*	7.62 x 54 R	FMJ / PB / HC I	10.4 ± 0.1 (core 5.3 hardness 63 HRC)	10 + 0.5	860 ± 10
11	L*	.308 Win.	FMJ / PB / WC	8.4 ± 0.1 (core 5.9)	10 + 0.5	930 ± 10
12	L*	.308 Win.	FMJ / PB / WC	12.7 ± 0.1 (core 5.58 hardness 1330 HV 10)	10 + 0.5	810 ± 10
13	L*	.50 Browning	FMJ / PB / HC	43.0 ± 0.5 (core 35.0 hardness 55 ± 2 HRC)		930 ± 20
14	L*	14.5 x 114	FMJ / PB / HC I	63.4 ± 0.5		911 ± 20
The rates of twist can be gathered from the dimension sheets (TDCC) of the CIP						
CB	coned bullet			L	full lead	
CIP	Permanent international commission for the testing of small arms			L*	rifle	
				MC	mild-steel core	
FMJ	full metal jacket (steel)			PB	pointed bullet	
FMJ*	full metal jacket (copper)			RN	round nose	
FMs	full brass			SC	lead-soft core	
FN	flat-nose			SCP	lead-soft core steel penetrator	
HC	hard core			TDCC	Dimension sheets of the C.I.P.	
I	Incendiary			WC	wolfram-carbide	
K	handgun					
The test steps 1 to 14 mentioned in table 1 are listed in increasing order according to their ballistic resistance. Test step 1 offers the lowest, step 14 the highest resistance against penetration. If a test specimen meets a particular level of resistance all underlying levels are also met. Step 6 and 8 are to be additionally tested with projectile FMJ/PB/SC calibre 7.62 x 39. Step 9 is to be additionally tested with the projectile in test step 7 calibre 308 Win. Step 10 is to be additionally tested with projectile type D (FMJ/PB/SC), 11.8 ± 0.1 g, v0: 810 ± 10 m/s calibre 7.62 x 54R.							

Table 2.4.- Classification of the protection levels for VPAM APR 2006 Edition: 2009 (VPAM, 2009).

2.1.5 Spain

Spanish Army uses their standards (Ministerio de Defensa de España, 2017), and they follow the guidelines of the NIJ standards for the bulletproof part.

2.1.6 Russia

Russia uses their state standard (GOsudarstvennyy STandart, GOST). This standard refers mainly to different ammunition, as they do not follow NATO guidelines, but they are part of the Euro-Asian Council for Standardization, Metrology and Certification, (EASC, 2017). Even though the threat considered comes from Russia, there is no specific class for as mild steel 7.62 x 39 mm (Table 2.5).

Class	**Name**	**Characteristic of the projectile**			**Distance firing (m)**
		Core type	**Weight (g)**	**Velocity (m/s)**	
Special protection classes					
C	Bayonet	—			—
C1	18.5 mm hunting	Lead	34.0±1.0	400±10	5±0.1
C2	Fragment	Steel ball	1.05		—
Basic protection classes					
Бр 1 (Br 1)	9x18 mm	Steel	5.9	335±10	5±0.1
Бр 2 (Br 2)	9x21 mm	Lead	7.93	390±10	5±0.1
Бр 3 (Br 3)	9x19 mm	Strengthen steel	7.0	410±10	5±0.1
Бр 4 (Br 4)	5.45x39 mm	Strengthen steel	3.5	895±15	10±0.1
	7.62x39 mm PS	Strengthen steel	7.9	720±15	10±0.1
Бр 5 (Br 5)	7.62x54 mm PP	Strengthen steel	9.4	830±15	10±0.1
	7.62x54 mm B-32	Strengthen steel	10.4	810±15	10±0.1
Бр 6 (Br 6)	12.7x108 mm B-32	Strengthen steel	48.2	830±20	50±0.5

Table 2.5.- Classification of the protection levels for GOST 34286-2017 (EASC, 2017).

After the review of the standard, it is possible to see that the threat considered in this thesis (mild steel 7.62 x 39 mm) is a usual reference. However, this is only possible after the recent update of the standards. Protection from this threat fails among the higher levels of protection.

2.2 Evolution

Shields and protections have to fulfil some constraints given by the threat, mechanical properties, weight and price. After the appearance of powder weapons, the protection of the soldier evolved from the full steel plate armour to some leather protection. The lack of protection of the plate armour was noted; therefore, a reduction in the weight of the protection was made to prime the mobility and agility of the user. Bulky helmets appeared again in World War I, for stopping fragments from explosions. That has been the primary purpose in military helmets since 1914. After World War II, helmets shields were still done in steel. However, new options started to be explored.

During the Vietnam War (1955-1975), vests with ballistic nylon and polycarbonate inserts could stop fragments and shrapnel. However, they were bulky and reduced the thermal comfort of the user; consequently, soldiers usually wore them open or did not wear them at all.

In 1964, Stephanie Kwolek synthesised high-quality aramid fibre at the Dupont laboratories, later named as Kevlar. The process oriented the molecules in the same direction as fibre, increasing the fibre's tensile strength (Table 2.6). This material made possible to manufacture flexible layers and proved useful for bulletproof protection. The outcome was a reduction of the weight in PPE and an increase in thermal comfort. Aramid was widely adopted to produce all kind of armours and shields. Aramid-reinforced composite helmets were a fundamental part of the U.S. Army Personal Armor System Ground Troop (PASGT) system (N.A., 1989) or the helmet used in the Belgian army manufactured by Schuberth.

In the 1980s, Allied-Signal, now Honeywell Performance Fibres (Colonial Heights, Virginia, U.S.A.), and DSM High-Performance Fibres (Heerlen, The Netherlands) presented ultra-high-molecular-weight polyethylene (UHMWPE) fibres. These large oriented molecules have enhanced mechanical properties (Table 2.6), improved structure as suggested by (Roylance et al., 1973), that provide the vests with protection equal to that of aramid for 15 per cent less weight. What is more, Polyethylene retains its properties when exposed to water. However, it is more difficult to weave, and its cost is higher than aramid fibres (Composite World, 2003).

In 1998, Second Chance Body Armor Inc. (Central Lake, Mich., U.S.A.) began using a fibre,

poly (p- phenylene-2.6-benzobisoxazole), or PBO. Toyobo Co. Ltd. (Osaka, Japan) traded it as Zylon. PBO fibre has excellent mechanical properties (Table 2.6) appropriate for ballistic protection. On the other hand, it costs several times as much as the other fibres, and there is a worrying degradation of this material (Chin et al., 2007).

Magellan Systems International in partnership with Dupont Advanced Fibre Systems developed another fibre, traded under the name M5. M5 fibre is based on the polymer poly(diimidazo pyridinylene (dihydroxy) phenylene) with excellent mechanical properties (Table 2.6). U.S. Army Natick Soldier Centre tested it. Areal density was estimated to be reduced up to 60 % for the same ballistic protection compared to Kevlar (Cunniff et al., 2002). However, it may degrade with solar radiation and moisture (Scott, 2006). Therefore, the ballistic protection fibres are mostly aramid and UHMWPE fibres (Chen, 2016).

Modules	**Density (kg/m^3)**	**Young modulus (GPa)**	**Tensile stress (GPa)**
Kevlar	1440	154	3.0
Spectra 900	970	66	2.4
Spectra 2000	970	124	3.4
Dyneema SK76	970	115	3.8
Zylon PBO	1550	270	5.8
M5	1700	270	4.0

Table 2.6.- Mechanical properties of fibres used for ballistic protection.

There are two significant factors for providing excellent impact resistance: energy absorption and speed of sound in the material. For a complete understanding of the process, other parameters have to be taken into account, such as adhesion to the matrix, temperature resistance or mechanisms of fracture and damage. For sorting the fibres, a figure of merit can be used for relating two parameters above mentioned, speed of sound and energy absorption:

$$U = \left(\frac{1}{2} \frac{\sigma_f}{\rho} \varepsilon_f \right) \sqrt{\frac{E}{\rho}} \qquad \text{Eq 1}$$

Where

U is a figure of merit

ρ is density

σ_f is fracture strength

ε_f is fracture elongation

E is Young modulus

If the fibres break without plastic deformation, the fracture elongation is expressed as:

$$\varepsilon_f = \frac{\sigma_f}{E} \qquad \text{Eq 2}$$

Therefore, Eq 1 rewrites as:

$$U = \frac{1}{2}\frac{\sigma_f^{\,2}}{E\rho}\sqrt{\frac{E}{\rho}} \qquad \text{Eq 3}$$

This parameter shows the importance of high strength combined with low density (Rimdusit et al., 2013). What is more, the U parameter units are [L^3 / T^3]. So, the cubic root of the parameter offers a velocity that could be related to the ballistic resistance. The parameter points out the outstanding properties of Dyneema (Figure 2.1), partially due to its lower density (Cunniff, 1992).

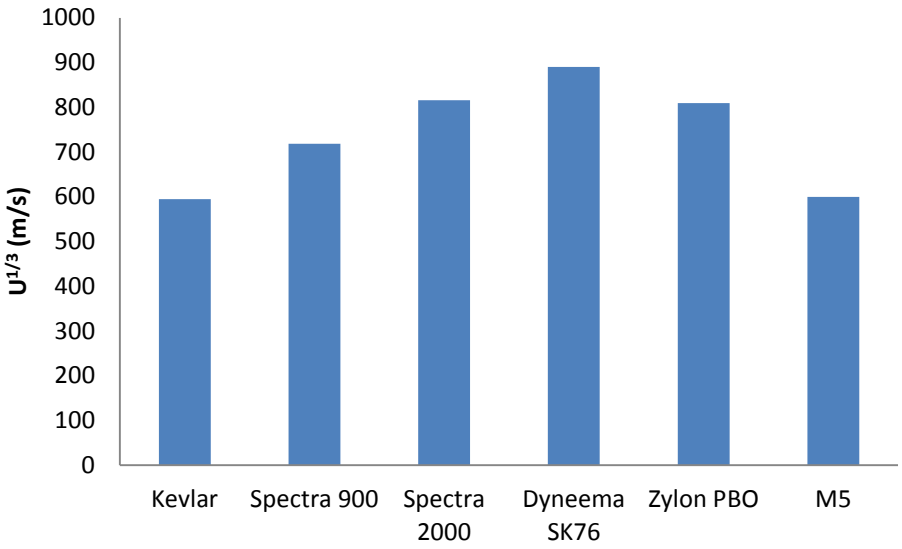

Figure 2.1.- Figure of merit ($U^{1/3}$) for the fibres used for ballistic protection.

The development of carbon nanotubes (CNT) does not permit sufficient quantities of textile to be produced. Nowadays, it can be only used for reinforcing composites (Chazot and Hart,

2019). Although theoretically, its potential for this application is enormous, its $U^{1/3}$ could be more than three times bigger than Dyneema (Wetzel et al., 2015).

However, researchers still disagree about the effects of the CNT on wounds. Some reported that some CNT had penetrated various biological barriers causing damage to humans (Qu et al., 2009), whereas others stated that some families of CNT would be beneficial for a wound (Li et al., 2015).

Helmets are manufactured with hard composites. The behaviour of the tissue in soft or hard armour can be different. One of the problems is to produce a deep draw. To circumvent this problem, Gentex cuts the tissue, polyethylene fibres or weaves them into pinwheel patterns, overlapping each layer to ensure complete coverage prior to compression moulding (Grick, 1986). The pinwheel strategy has some disadvantages because sometimes it produces variations in fibre volume and areal density in parts of the helmet.

Hard face inserts for stopping rifles ammunition were upgraded using ceramic tiles. Nowadays, lighter options like a ceramic faced laminated composite with better ballistic performance than steel are available (Übeyli et al., 2007). The ceramic face breaks up the bullet into small parts, and the composite wrap prevents them from being expelled everywhere.

It is possible to find available commercial body ballistic protection level IV. It is a level IIIA vest (Table 2.7) enhanced with a ceramic insert (Table 2.8). The vests are done with composites such as Kevlar or Dyneema, while the insert is ceramic, usually made of alumina or silicon carbide. The insert must always be used within a vest for being useful.

Ballistic capabilities :	NIJ Level IIIA according to STD 0101.04
Armour material :	DSM Dyneema®
Areal Density :	5.3 kg/m^2
Thickness :	7 mm
Warranty :	10 years

Table 2.7.- Properties of an IIIA vest.

Size :	25.4 x 30.5 cm
Weight :	3.2 kg
Thickness	1.9 cm
Ballistic capabilities :	NIJ Level IV according to STD 0101.04 in combination with a vest.

Table 2.8.- Properties of the ceramic insert.

Whereas, only level III-A is available for helmets. They are only built with a single composite material. A helmet able to stop pistol ammunition weighs 1.4 kg. Moreover, it is necessary to check Back Face Deformation (BFD), because it can be significant enough to damage the user. No standard specifies acceptable values in force. ASTM (American Society for Standard and Materials) is currently developing a standard about specifications for ballistic-resistant head protection, paying attention to life-safety criteria. Ceramic inserts are available, but this option is limited and remains too heavy. Moreover, it does not avoid the problem with the BFD (Freitas et al., 2014a).

Current helmets only have a criterion for the maximal deflexion, thus the maximal depth of indentation or the back face signature. Advanced Combat Helmet (ACH) and Enhanced Combat Helmet (ECH) of the US Army require maximum Back Face Signature (BFS) when impacted with 9 x 19 mm ammunition at 425 m/s of 16 mm for lateral impacts, and front and back shots require only 25.4 mm of maximum BFS. ECH can defeat partially rifle threats. Unfortunately, further information remains confidential.

Some real army helmets are shown as an example: PASGT helmet is a infantry helmet which provides ballistic protection against fragments from explosives devices. The shell is a composite structure consist of several levels of Kevlar-29. Its mass is between 1.4 kg and 1.9 kg. The chinstrap is a two-point design, having an open chin-up and two adjustable buckles and a single snap fastener. Its has a strap-netting suspension (David et al., 2011).

Belgian helmet was manufactured by Ulbrichts with an aramid composite (Figure 2.2). The inner structure consists of several plastic cylinders and a leather strip. It guarantees the standoff between the head and the helmet and increases the thermal comfort. It also acts as a shock-absorbing layer for low energy impacts on the helmet shell.

(a) Shell of the helmet

(b) Liner of the helmet

Figure 2.2.- Belgian Army helmet used for the tests.

The 1.58-kg Advanced Combat Helmet (ACH) is a lighter version of the old PASGT. The model is cushioned on the inside. It provides increased 9 x 19 mm bullet protection.

The Enhanced Combat Helmet (ECH) is an improved ballistics protection capability version in service since 2013. The helmets weigh between 1 kg to 1.3 kg. The helmet is also required to protect against certain rifle projectiles.

The Spanish COBAT helmet offers fragment protection up to 650 m/s and 9 x 19 mm with 1.35 kg. It was fielded in 2017.

The Russian 6B47 helmet weighs 1.2 kg, has NIJ II-A/BR2 protection level (9 x 19 mm Para bullets / 9 x 18 mm Makarov bullets). It can stop steel fragments.

Police forces occasionally wear helmets which are based on military design, adding some more material; typically titanium, like the helmet manufactured by Ulbricht. This new helmet enhances the protection against pistol and rifle with a ceramic applique in the front. It fulfils the ballistic requirements of the VPAM level 6 with a total weight of around 2.71 kg for the frontal part.

The WELP Group offers a VPAM Level 6 said in a statement that the VPAM 6 combat throughout the helmet's entire surface area of 1335 cm^2. Figure 2.3 sums the protection level and mass of the presented helmets, as well as the objectives for this research.

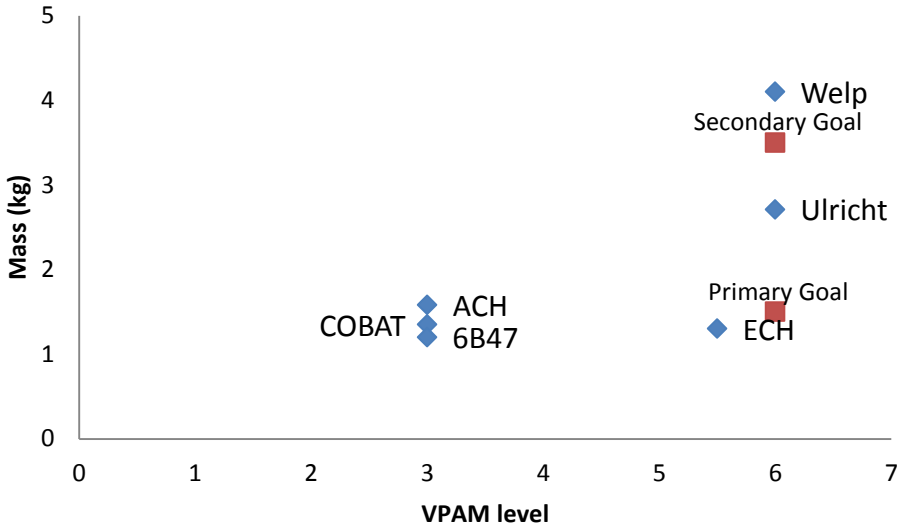

Figure 2.3.- Weight and ballistic level protection of different helmets (Mass for Welp helmet is estimated, Ulricht helmet level 6 protection is only frontal, VPAM level for ECH is estimated) in blue. Goals of this research in red.

The project looks for improvement of the existing helmets, overranking them in protection and seeking a mass reduction.

3 LIGHTWEIGHT ARMOUR MATERIALS

This chapter is firstly going to emphasize the necessity of lightweight material for personal armour, and then the different families of light materials used for ballistic protection are described regarding their position in the armour pack.

If the geometry of a helmet is simplified to a hemisphere, with a 150 mm radius, a estimation of the weight and the areal density of the geometry can be done. The proposed armour can be first checked as a solution regarding the weight and thickness of the shield. For example, for a 3.5 kg helmet, an areal density of about 23 kg/m^2 is acceptable. Concerning the selection of the materials, for a 10 mm thickness, the whole density of the materials shall not exceed 2300 kg/m^3 (Figure 3.1). This overview triages materials that could fit for the project.

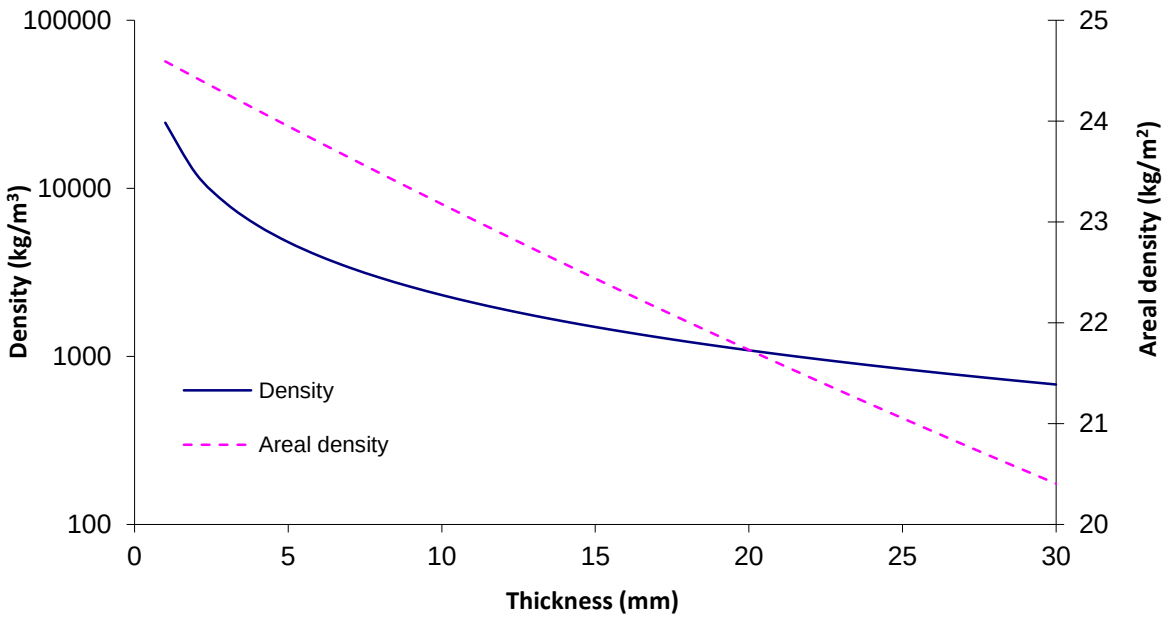

Figure 3.1.- Mathematical model relating areal density, density and thickness for material selection.

Checking the materials available with attention-grabbing properties and low weight, three families of materials appear composite materials, ceramics, and metals (Figure 3.2). Another group of materials remarkable for the project are foam, but they have weak mechanical properties.

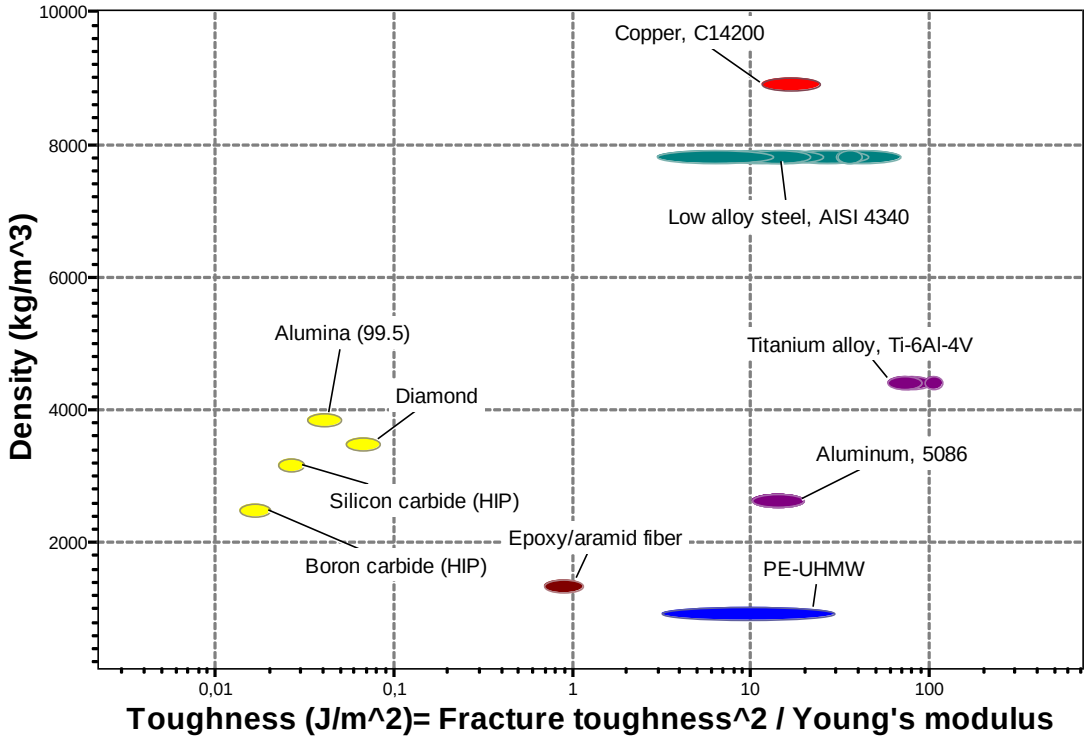

Figure 3.2.- Material selection regarding the density and toughness.

Composite or steel helmets were able to only defeat soft core projectiles at low velocities. Mils steel or hard core projectiles at high velocities require an improvement in the properties of the materials. As no material can meet all the properties needed for stopping a rifle projectile, it is necessary to make multilayer protection. Following the structure of a bullet-resistant vest, there are two parts, although the whole shield works together for stopping the projectile. The first part (strike and wave spread layer) has to stop the projectile and mostly defines its ballistic properties. This part involves the ceramic and composite layer. It is essential to check and study the variability, such as the interplay between the ceramics and the composite layer that may decrease the ballistic resistance and the erosion of the projectile (Tasdemirci et al., 2012). The second part has to limit the force transmitted to the user. Otherwise, the deformation of the shield can injure the user severely. Dedicated composite or metal sheet limit the BFD. Adding a metal layer to composite armour has to be as hard as possible if positioned in the front part. Otherwise, it should be ductile. Regarding the BFD, the best position of the metal plate is in the back (Horsfall et al., 2013). A soft final layer, as liner or pads, is used to reduce the force transmitted to the head (Sahoo et al., 2015; Tan et al., 2012).

3.1 Strike layer

3.1.1 Introduction

Strike layer has two main tasks: deform (or fracture, if it is an armour piercing round) the core of the projectile and spread the impact over a large area of the second layer. The hard core becomes like the shape of a mushroom, which is easier to be stopped. The material used for this layer is ceramic due to their high hardness and high compressive strength. Ceramics are very brittle, so they have to be used with a back face material, as composite or metal for holding the tile. For a maximal ballistic limit, it is found that the value of the parameter σ/ρ determines the place of the plate in the multilayered target with the maximum ballistic limit velocity (Ben-Dor et al., 1999).

Several ceramic materials have been considered and were examined intensively for ballistic protection, such as silicon nitride (SN), titanium boride (TiB_2), aluminium nitride (AlN), SIALON (Silicon aluminium oxynitride), fibre-reinforced ceramic (e.g. C-SiC) or ceramic-metal composite materials (CMC). The only way to recommend the best ceramic material that may be the most appropriate for a ballistic threat should also take into account the weight, manufacturing ability and cost (Medvedovski, 2010a). Therefore, despite their high ballistic performance, these materials are not used for ballistic protection for technical and economic reasons (CeramTec). Usually, the most used technical ceramics are silicon carbide, boron carbide and alumina (2008). Boron carbide has more ballistic efficiency than other ceramic materials expected to be used for ballistic purposes, followed by silicon carbide tiles (Rozenberg and Yeshurun, 1988a). Others authors with other ballistic tests conditions show that the silicon carbide outperforms others ceramics (Kaufmann et al., 2003).

The ballistic efficiency evaluates the ceramic performance based on its areal density upon a ballistic impact (Rozenberg and Yeshurun, 1988a). This value is the impact velocity and projectile dependent. Ballistic efficiency is calculated comparing the deep of penetration (DOP) in a semi-infinite baking material with and without the ceramic tested.

$$\eta = \frac{1}{2}\frac{\rho_b\left(P_b(V_s) - P_s\right)}{\rho_c t_c} \qquad \text{Eq 4}$$

Where

η is the ballistic efficiency

ρ_b is the density of the backing

$P_b(V_S)$ is the Deep of Penetration (DOP) into unprotected backing as a function of the impact velocity of the projectile

P_s is the residual DOP into the backing

ρ_c is the density of the ceramic

t_c is the ceramic thickness.

The microstructure plays a vital role in this material. Pores reduce the strength of ceramic. Grain size should be small as well as refinement of the defects and its distribution enhance the performance of the ceramic tile (Belenky and Rittel, 2012; Holland and McMeeking, 2015; Mashhadi et al., 2010). Dynamic fracture toughness is also higher than static (Pittari III et al., 2015).

It is not possible to make complex shapes in every material with an acceptable ballistic grade. Usually, planes and helicopters are protected with boron carbide tiles, where weight is critical. A problem with the ceramics is that they are not able to support several impacts, as long as after one hit cracks expand everywhere. This fact is solved using small tiles for covering the protected area. Small tiles reduce the damaged surface and can be replaced more straightforward and cheaper than more extensive options. The behaviour of one tile alone or surrounded by other tiles or other material is modified. Thus, the confinement with the correct acoustic impedance is essential (Table 3.1), thus the confinement should have an impedance close to the ceramic tile impedance (Savio et al., 2011a). The acoustic impedance of a material is defined as:

$$Z = \rho C_L \qquad \text{Eq 5}$$

Where

Z is acoustic impedance

ρ is density

C_L is the velocity of the wave

Material	Acoustic impedance (MRayls)
Silicon carbide (sintered)	37.35
Silicon carbide (hot pressed)	38.84
Boron caribe	35.00
Alumina	42.08
Steel	45.24
Aluminium	17.01
PE	2.52
Water	1.48
Air	0.0004

Table 3.1.- Acoustic impedance of different materials (Bottiglieri, 2012).

Acoustic impedance determines the acoustic transmission and reflection at the boundary of two different materials. During an impact, compressive waves are created: when they reach the border of the tile, the incident wave splits in an inverted reflected wave and transmits wave towards the other material.

The inverted reflected wave is a traction wave. Ceramic tiles can handle enormous compressive force without any problems, but they are unable to deal with the same order of magnitude of force generated by the traction wave. The more energy dissipated as transmitted energy, the better for the impacted ceramic tiles. They will have to manage a smaller traction load. The Intensity Transmission and Reflection Coefficients (ITC, IRC) indicate the amount of energy of the incident wave that goes to each material (Kremkau, 2014).

$$ITC = \frac{4Z_1Z_2}{(Z_1 + Z_2)^2} \qquad \text{Eq 6}$$

$$IRC = \frac{(Z_2 - Z_1)^2}{(Z_1 + Z_2)^2} = 1 - ITC \qquad \text{Eq 7}$$

Where

Z_1 is the impedance of the first material

Z_2 is the impedance of the second (baking) material

The optimal is to have continuous material for not having reflected waves (Figure 3.3). Regarding the values of different materials (Table 3.1), steel confinement will produce small

reflected waves, while aluminium produces much bigger ones. Smooth contact between both surfaces is vital for avoiding gaps.

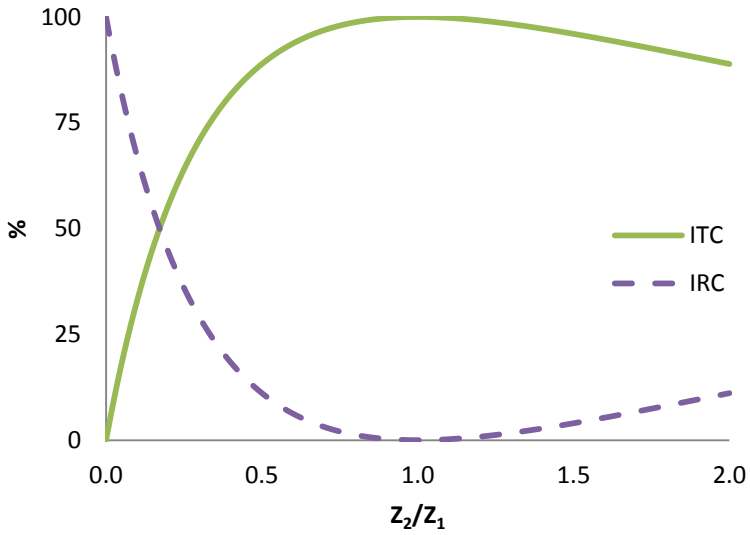

Figure 3.3.- Representation of ITC and IRC vs the ratio Z_2/Z_1.

For this research, several ceramics were tested. The most extensively used was silicon carbide.

3.1.2 Manufacture

There are different ways of producing silicon carbide (SiC) tiles (Table 3.2). Solid – State Sintered Sic (SSiC) tiles have the right balance of mechanical properties, weight and manufacturability.

SiC material type	Density (g/cm^3)	Porosity (%)	Young modulus (GPa)	Flexural strength (MPa)
Ceramic bonded SiC (CSiC)	2.8	<20	250	160
Infiltrated SiC (SiSiC)	3.12	<1	400	350
Solid – state sintered SiC (SSiC)	3.15	<2	410	430
Liquid phase sintered SiC (LPSSiC)	3.21	<1	420	730
Hot – pressed SiC (HPSiC)	3.20	0	450	640
Hot – isostatic pressed (HIPSiC)	3.21	0	450	640

Table 3.2.- SiC types and properties.

In solid-state sintering, coarsening tends to dominate over densification, especially in highly covalent ceramics such as silicon nitride and silicon carbide (Izhevskyi et al., 2000). Due to the high temperatures applied, and to relatively prolonged soaking times at these

temperatures, abnormal grain growth occurs, often resulting in anisotropic α – SiC phase formation. It is complex to produce a fully densify sample of these covalent ceramics without any additive as bond material. In solid-state sintering, the only transport mechanism is atomic diffusion in the solid-state. Because the bonding in silicon carbide is covalent, self-diffusivity is very low and pure silicon carbide could not be sintered to full density. Bonded ceramic tiles use other material for the bond, such as silicon nitride. CSiC is a cheaper manufacture method, but mechanical properties are not as good as with SSiC (Medvedovski, 2010b).

An attractive property of the ceramic tile is its capacity to hold the projectile during a short lapse of time, in the order of some microseconds. This lapse of time during the tile overcomes the projectile is named dwell time; and it is governed by physical properties of the material, like the speed of sound in the ceramic. It can be indirectly estimated as (LaSalvia, 2015):

$$T_{Dwell} = \frac{\Delta L}{V_i} \qquad \text{Eq 8}$$

Where

T_{Dwell} is the Dwell time

ΔL is the deformation of the projectile

V_i is the impact velocity of the projectile

During this period, the ceramic behaves like an elastic wall. The projectile flattens plastically and erodes. The tip of the projectile generates compressive waves and a fracture conoid (Figure 3.4) that grows until the backplane of the armour (Den Reijer, 1991). There is also a fragmentation of the ceramic due to the shock waves. When reaching the other face, these shock waves return as tensile waves and initiate many cracks. The magnitude of the passing/reflected wave depends on the impedance mismatch of the ceramic and the back face material. Ceramics cannot handle large tensile forces, so some radial cracks start in the rear face of the tile (Sherman and Brandon, 1997).

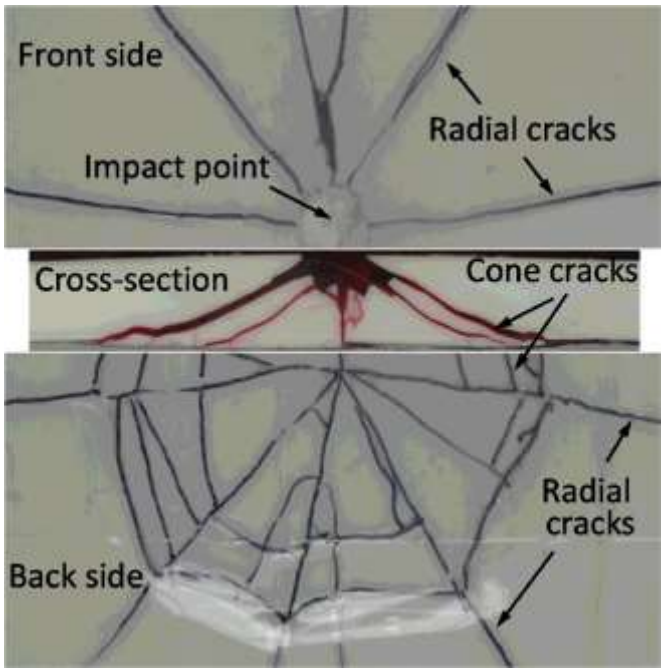

Figure 3.4.- Fracture conoid cracks (Rahbek et al., 2017).

3.1.3 Ceramic tested

Boron carbide has high hardness and high elastic modulus despite its low density. Its high flexural strength and fracture toughness guarantee extraordinarily high specific stopping power to defeat high-velocity projectiles. VERCO successfully improved the manufacturing process of sintered boron carbide tiles (Table 3.3). The density reaches up to 99.8 % of the theoretical one (Speyer and Lee, 2004; Thévenot, 1990).

Property	**Typical Values**
Grain size, µm	3
Density, kg/m^3	2450
Flexural strength, 4py bend, Mpa	350
Vickers hardness, Kg/mm^2	2400
Elastic modulus, GPa	370
Fracture toughness, MPam^(1/2)	3.2
Poission ratio	0.17

Table 3.3.- Properties of sintered B4C from VERCO.

Another company, SM Group, also provided some samples of boron carbide. They produce armour for helicopters; consequently, they are able to manufacture complex shapes (Table 3.4).

Property	Typical Values
Density	2.5 - 2.6 g/cc
Hardness (Knoop 1 Kg)	2600
Flexural Strength (MOR), 200 C	240 MPa
Fracture Toughness, Klc	3-4 MPa $m^{1/2}$
Elastic Modulus, 200 C	360 GPa
Thermal Conductivity, 200 C	48.0 W/ mK

Table 3.4.- Properties of sintered B4C from SM group (SM Group).

Second ceramic material tested was silicon carbide. Two different types of ceramic were used (Table 3.5): high density grade of silicon carbide tile –SSiC, density 3100 kg/m^3 – two different thicknesses: 4.2 mm and 3.2 mm (HEXOLOY SA); low density grade of silicon carbide tile –bonded, density 2900 kg/m^3, thickness 5 mm– (FORCERAM). Both of them were manufactured by Saint-Gobain.

	Hexoloy SA	Forceram
Composition	Sintered SiC	Bonded SiC Chemical composition SiC 68 % / Bond 25 %
Grain size (µm)	4-10	Not Available
Density (kg/m^3)	3100	2900
Hardness	2800 kg/mm^2 Knoop, 100g	75 RHA
Flexural strength, 4py bend (Mpa)	380	160
Compressive strenght (MPa)	3900	Not Available
Elastic modulus (GPa)	430	250
Fracture toughness ($MPam^{1/2}$)	3	3.5
Poission ratio	0.14	Not Available

Table 3.5.- Physical properties of SiC ceramic tiles (Saint-Gobain).

3.2 Wave spread layer

3.2.1 Introduction

Wave spread layer, usually as composite such from aramid or ethylene fibres, offers excellent behaviour for ballistic impact. Fibres resist projectile penetration due to their inherent tensile strength, absorbing energy while they elongate. The composite material used for this research is Dyneema, manufactured by DSM. It is an Ultra-High Molecular Weight Polyethylene (UHMWPE) fibre-based composite laminate with polyurethane (PUR).

3.2.2 Manufacture

The excellent properties of the UHMWPE fibre (Table 3.6) allow standing against impact much better than other materials.

Young Modulus	Tensile stress	Shear stress (GPa)	Linear density	Strain to failure (%)	Diameter (µm)	Density (kg/m3)	Sound speed (km/s)
132 GPa	3.8 GPa	1.8	0.0002gram/m	3.5	16.1	980	11.6
1350 cN/dtex	38.4 cN/dtex		2 dtex				

Table 3.6.- Properties of SK76 filament in UHMWPE composite (Chocron et al., 2013; Hudspeth et al., 2012).

Not only fibre properties but also the structure formed is critical. Fibres are packed without being woven (Figure 3.5), which produces a stronger and lighter material. It also allows for bigger compressibility than woven structures (Laible Roy, 1972).

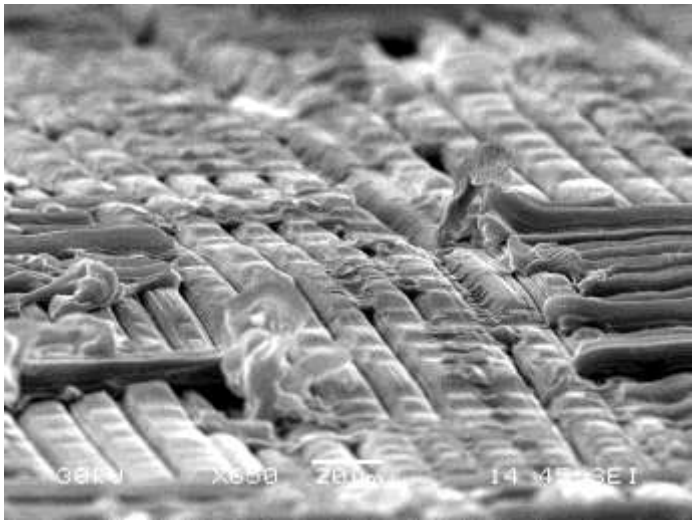

Figure 3.5.- UHMWPE fibres in the laminate.

Fibres lay in a polyurethane-based elastomers matrix, precisely a polyetherdiol-aliphatic diisocyanate polyurethane (PADP) matrix. The matrix represents about 20 % of the composite. The combination of high fibre strength and low matrix shear strength produces a complex mechanism that gives rise to its unrivalled performance. The matrix shear strength has to be small in order to improve the ballistic resistance (Chocron et al., 2014; Karthikeyan

et al., 2013). Single layers of SK76 filament are parallelly aligned, which creates a ply (Sapozhnikov et al., 2015). Every ply has an average thickness of 2.5 filaments (Figure 3.6).

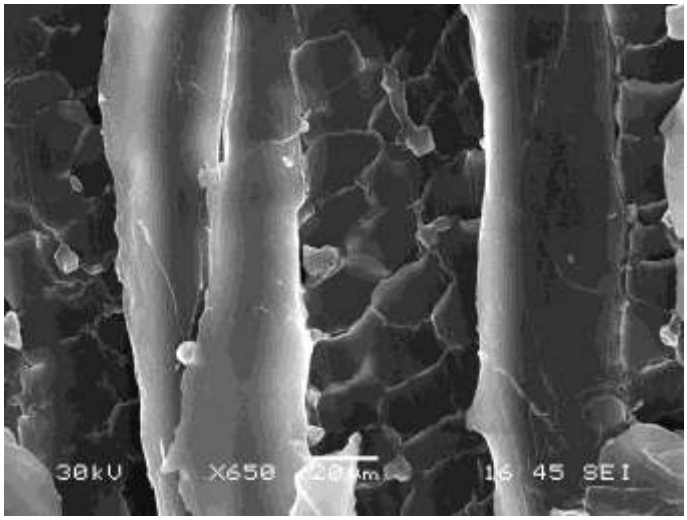

Figure 3.6.- Section of several plies in the laminate in UHMWPE composite.

Four plies perpendicularly positioned make a layer; they are embedded in a PU matrix. This structure distributes impact energy along the fibres much faster and more evenly than conventional woven fabrics.

Study of different ways of stacking the layers has already been done in literature (Karthikeyan et al., 2016). Simply stacking the layers or displaying them in different helicoidal structures shows that trade in between ballistic resistance and back face deformation is produced (Hsieh et al., 2016). The best ballistic resistance is an entirely orthogonal structure. Another stacking sequence appeared, dubbed «hybrid» with a good trade of ballistic resistance and BFD. This design changes the directions of the ply; first, 75 % of the layers follow the orthogonal cross structure. The rest of the layers are revolved 22.5º, not 90º. UHMWPE composite laminates in the hybrid configuration reduce the BFD at no or small cost of resistance penetration (Vargas-Gonzalez and Gurganus, 2015; Zhang et al., 2015). Orthogonal and hybrid structures are going to be utilised in this research.

3.2.3 Properties

Determining the mechanical properties of a panel of Dyneema is challenging, due to the high tensile strength and low friction coefficient (F. Zok, 2010). It is needed a great surface for a

small testing section (Figure 3.6). Mechanical properties are astonishing taking in account the high mechanical properties regarding the low density (Table 3.7).

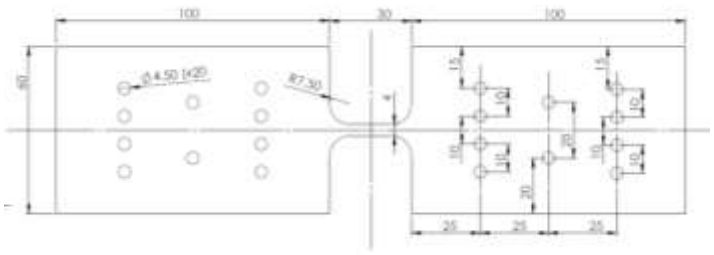

Figure 3.7.- Testing sample for UHMWPE composite (F. Zok, 2010).

Materials	Density (kg/m^3)	Strain to fracture (%)	Tensile strength (MPa)	Tensile modulus (GPa)
Dyneema® HB80	980	3.5	2500	120

Table 3.7.- Nominal mechanical properties of Dyneema® HB80 (Kulkarni et al., 2013).

Mechanical properties are sensitive to the rate of load. Further empirical studies allowed to create an equation to estimate ballistic properties (Gorp et al, 1993), empirical ballistic resistance is defined by:

$$V_{50} = 232\ \delta^{0.5}\ m_p^{-1/6} \qquad \text{Eq 9}$$

Where:

V_{50}= Ballistic resistance (m/s)

δ= armour areal density (Kg/m^2)

m_p=mass projectile (g)

This formula was obtained with FSP projectile and might be used for other threats. However, increasing the thickness of the composite does not always imply an increase in the ballistic limit (Shaktivesh et al., 2013). Only a 19 kg/m^2 protection stops an AK round, as shown by DSM (Dyneema®). This area density is acceptable to produce the shell of the helmet, but the significant transient deformation makes a helmet only made with this composite useless. This composite is going to be used in this project because of its unique mechanical properties, including low density.

The primary energy absorbing mechanisms are the energy absorbed in the tensile failure of the primary yarns. Higher strain rates increase energy absorption per unit volume. Other essential mechanisms are the elastic deformation of the secondary fibres and the formation of the moving cone, which produce the BFD. Minor mechanisms are the delamination and the sliding of the layers. Also, a side effect is the melted fibres in the impact zone created by the friction heat (Figure 3.8). Fibre melts at 150 °C and matrix at 180 °C (Attwood et al., 2014; Karthikeyan and Russell, 2014; Morye et al., 2000).

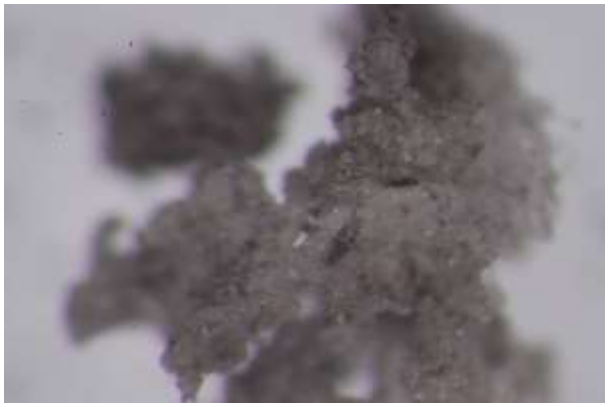

Figure 3.8.- Melted fibres retrieved from the impact point in UHMWPE composite.

3.3 Liner

Ballistic helmets typically employ one out of two types of liners, foam padded and strap-netting liners (Figure 3.9).

(a) Foam padded liner.

(b) Strap-netting liner.

Figure 3.9.- Liners of a ballistic helmet.

Their primary function is to hold the helmet in the correct position in an ergonomically acceptable way. The two liners systems have different performance regarding heat comfort and reducing the pressure field around the head while a blast or impact event occurs. Pads allow distributing the impact forces to broader areas, reducing the loads to the head of the user (Li et al., 2010; Salimi Jazi et al., 2012).

The key for energy absorbing properties of the foam is its cellular and crushable structure. During compression, the cells compress and fracture which prevents the impulse to be transferred to the body directly. Low-density foam with a small cell size is more useful to reduce this impulse (Liaghat et al., 2010; Nasirzadeh and Sabet, 2014). Foam density plays a minor role in dissipating energy.

It is possible to calculate the amount of foam needed with the next equations:

$$F = PS \qquad \text{Eq 10}$$

Where

F is the maximum allowable transferred force

P is the pressure (compression stress)

S is the contact surface

The force and the surface of the impact define the crushing pressure of the foam. This value is determined by the plateau in the graph compression stress-strain (Avalle et al., 2001), and changes for different materials and densities. The ideal is to equal the impact energy with the crush energy absorbed by the foam. The kinetic energy of the projectile and the energy to be absorbed is calculated as follows:

$$E_k = \frac{1}{2} m V^2 \qquad \text{Eq 11}$$

Where

E_k is the kinetic energy

m is the mass

V is the velocity

For the case of this study, the mass is crucial, not only of the projectile but also of the moving cone of the shell of the helmet.

The crushing energy absorbed by the foam can be calculated with:

$$E_k = \sigma \varepsilon v \qquad \text{Eq 12}$$

Where
v is the crushed volume
ε is the compression strain
σ is the plateau stress

Eq 11 and Eq 12 should be equalled to be able to assess the quantity of kinetic energy that the foam can dissipate.

4 EXPERIMENTAL TECHNIQUES

Different experimental techniques were used to achieve the objectives of this research. This chapter explains the different set-up and techniques used for this research.

4.1 Ballistic resistance

In order to estimate the ballistic resistance of any armour configuration, it is necessary to shoot the type of projectile with the correct velocity. Due to the enormous types of projectiles present nowadays, a universal weapon with interchangeable barrels is used for this purpose (Figure 4.1). Each barrel is prepared for only one type of projectile.

Figure 4.1.- Universal barrel mounted in the weapon.

The projectile velocity is measured with a double optical basis. The target is placed with regards to geometry and boundary conditions (Figure 4.2).

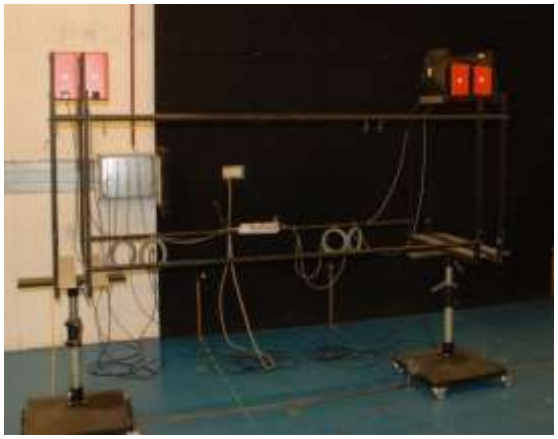

(a).- Optical bases.

(b).- Support STANAG 2920.

Figure 4.2.- Laboratory set up for measuring projectile velocity.

V_{50} is the velocity at which a given projectile will defeat a given armour shield 50 % of the time. In the case of estimating the V_{50}, tests are conducted as described in STANAG 2920 (NATO, 2016). For shooting projectiles with different speed, it is necessary to put less powder in the cartridge than the nominal quantity. The target is positioned 5 m ahead of the muzzle. The optical bases are positioned in the middle. The measurement of the speed is corrected to estimate the speed of the projectile at the impact point using Eq 13:

$$V_i = V_s e^{\left(\frac{-X\rho_a C_d A}{2m_p}\right)} \qquad \text{Eq 13}$$

Where:

V_i=projectile velocity at the target
V_s=projectile velocity at the point of measurement
X= distance from the measurement point to the target
ρ_a= air density
C_d=average drag coefficient
A=projectile presented area
m_p=projectile mass

Regarding the target, whether it has been perforated or not, it is possible to estimate the V_{50}. For this purpose, there are several mathematical tools developed for reaching the value. Among different statistical procedures; such us Probit, STANAG, logit, c-log-log; for estimating the V_{50}, STANAG and Probit estimations are used in this research (Mauchant et al., 2011).

4.1.1 V_{50} STANAG

This estimation requires a small number of shots, but it does not provide any value of the scatter of the data. This system is commonly used as both experimental measurement and production check. The first step is to use a clear definition of a complete perforation of the armour. Once a projectile has been fired, the criterion of perforation is met when a rod can get through the armour completely, or the last layer of the armour is broken (spalling). Any other event is considered no penetration.

At least six shots are needed for the calculation: using the three no perforation with the highest velocity and the three perforations with the lowest velocity, V_{50} is the arithmetical mean of the group of velocities.

4.1.2 V_{50} PROBIT

This procedure assimilates the ballistic resistance of a shield to a Cumulative Distribution Function (CDF) of a probability density function.

$$CDF(x) = \frac{1}{2}\left(1 + erf\left(\frac{x-\mu}{\sigma\sqrt{2}}\right)\right) \qquad \text{Eq 14}$$

Where
erf is the error function
σ is the standard deviation of the ballistic resistance distribution
μ is the average of the ballistic resistance distribution, the V_{50}

μ will be the V_{50}. The software scans all the possibilities and chooses the best pair of values (μ and σ) that fits with the tests performed. With this estimation, scatter of the data is also an output. Moreover, the more tests performed, the more accurate the results are.

4.2 High-speed cameras

High-speed cameras allow studying different phenomena. In the laboratory, there are two FASTRAMCAM SA5 cameras. They can film up to 1000000 fps. For example, the next figures are two consecutive frames made by the camera of a projectile penetrating a ceramic target (Figure 4.3).

(a).-Frame 1.

(b).-Frame 2, after 3.09 μs.

Figure 4.3.- Projectile hitting the ceramic tile.

It is possible to have stereoscopic vision using two cameras. The target has a black and white speckle pattern made with non-reflective paint (Figure 4.4). This measurement system is called 3 Dimensional Digital Image Correlation (DIC) and measures the displacement of a surface in the three axes.

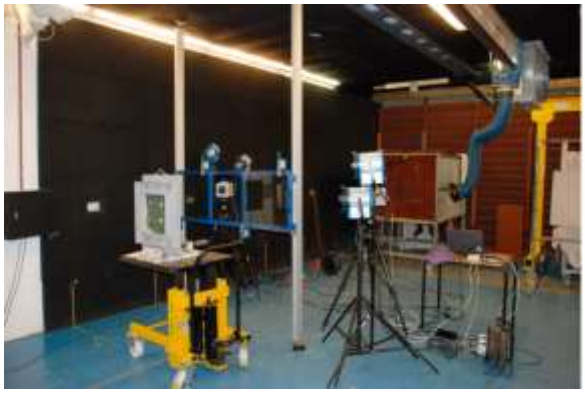

(a).-Laboratory set-up. Overview.

(b).- Speckle pattern.

Figure 4.4.- Set up for stereoscopic vision.

With this technique, it is possible to calculate the speed, acceleration, and curvature of the bulge produced by the impact (Figure 4.5 and Figure 4.6). It is a very accurate technique for studying the dynamic deformation produced during the impact.

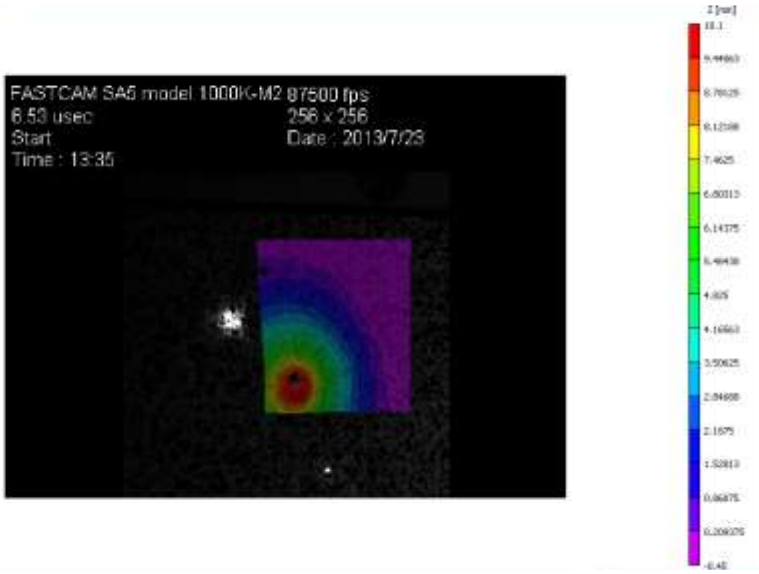

Figure 4.5.- Post-processing of the data, field of displacement.

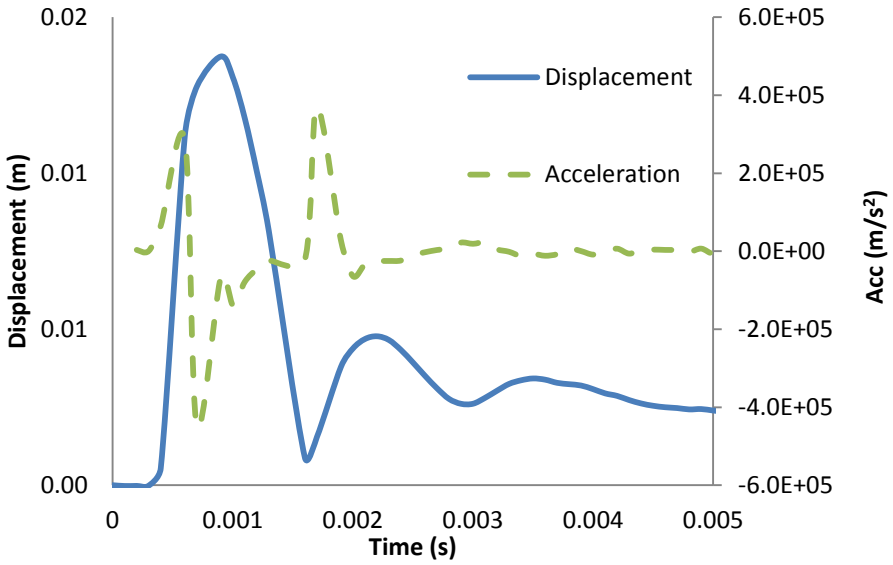

Figure 4.6.- Plot with the displacement and the acceleration of the back face helmet upon an impact.

A problem appeared when using this technique for ballistic impacts. The usual paint for making the speckle pattern does not remain stuck during the entire test 3D DIC (Figure 4.7).

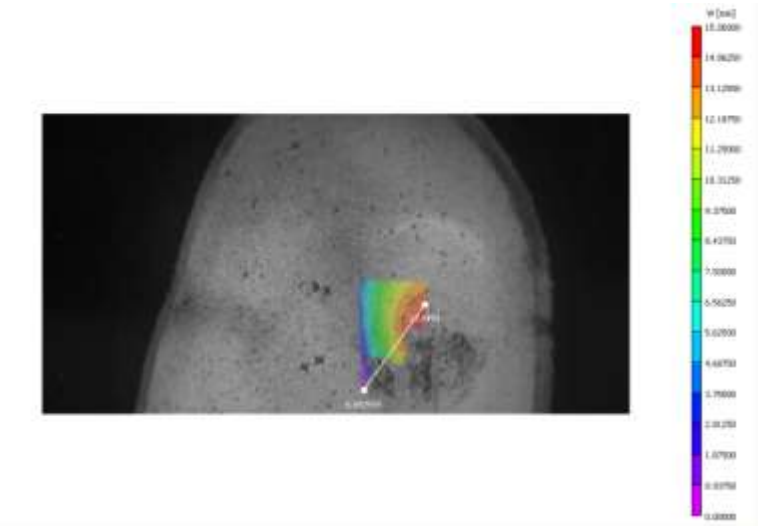

Figure 4.7.- DIC applied to an impacted helmet. Image of the interior part of the shell, when the maximum displacement occurs.

At first glance, it seems that the paint detaches because of the acceleration of the support material. Nevertheless, after checking that the paint comes off from the border of the deformed zone and not only from the centre; it is possible to notice that the paint comes apart from the surface when it bends fast enough. This paint is not able to replicate the movement of the impacted zone. It is not only because of the normal acceleration of the surface but sometimes the zone without paint appears when the zone is exceedingly bent.

After researching about other covers with excellent mechanical and bonding properties, polyurea seems to be a good option. Ballistic properties change insignificantly unless adding a thick layer of polyurea which is not used for that purpose (Xue et al., 2010). However, there is a risk of debonding due to the hyperelastic extension of the polymer (Ackland et al., 2013).

For trying to solve this problem, some tests have been done with this material for painting the speckle pattern. Six samples have been tested for evaluating the aptitude of the paint in a VIC 3D analysis. There are three types of materials (INOX, Aluminium and HB 80), and the speckle pattern has been made with two types of paint (Elastoguard S300R and Elastoguard S300R + WP). During the test, a Kevlar pack was in the strike face. 9 x 19 mm is the ammunition used for this test (Table 4.1).

Sample	Paint	Velocity (m/s)
A	S300R	353
Al	S300R + WP	310
INOX	S300R	322
INOX	S300R + WP	378
HB 80	S300R	417
HB 80	S300R + WP	414

Table 4.1.- Tested samples for studying the new coating.

All samples were successfully tested, and the paint remains attached to the base layer. Although it would be better matte paint, the shine level is enough for making the test. Even if there is perforation, only a little part of the speckle pattern is damaged. This is important in case of testing perforating events; this material would give more information than the old one.

4.3 K – Serie 600 Coordinate Measuring Machine (CMM)

It is difficult to accurately measure the permanent deformation produced in the back face of the target with traditional tools. This CMM allows digitising objects and making a virtual model. The virtual model, as a point's cloud, makes it faster and easier to get these data than with the real sample (Figure 4.8)

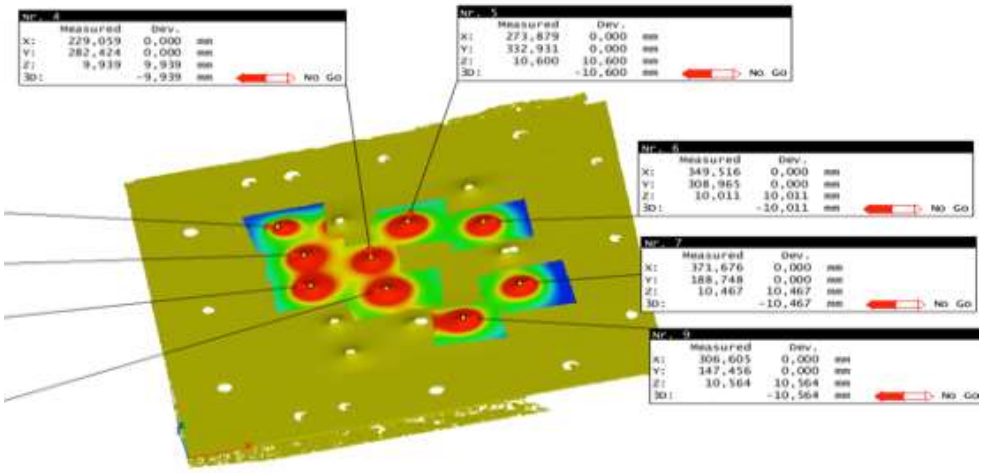

Figure 4.8.- Digitalize sample of the back face bulges of the target.

A scanner and the K – Serie 600 CMM portable system composed of three cameras (Figure 4.9) are able to position all the points of the object with an accuracy of 90 μm.

Figure 4.9.- 3D scanner system: cameras.

This scanner has been used for measuring the DOP in the clay, and the BFD of the samples.

4.4 Pressure Measurement Film

The pressure measurement film, developed by Fujifilm, can measure pressure and contact loads. Microcapsules break and produce a red stain on the film when pressure is applied and the colour density changes according to the various pressure levels. Prescale films are less than 200 μm thick. They are suitable for studying the force of the BFD of a shield (Figure 4.10).

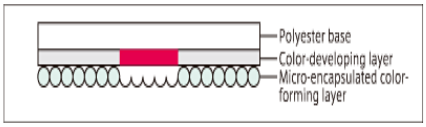

Figure 4.10.- Structure of the Prescale film.

There are seven types of Prescale available to detect varying pressure range (0.05～300 MPa); for this research, only high-pressure films seem to be interesting (Table 4.2). The colour has to be translated to the pressure load thanks to software, FPD-8010E develop by Fujifilm. The accuracy of the film is 10 % while testing on recommended conditions; 20 – 35 °C and 35 % - 80 % RH.

Product	**Range (MPa)**
Super High Pressure (HHS)	130-300
High Pressure (HS)	50-130
Medium Pressure (MS)	10-50

Table 4.2.- Range of measurement of the Prescale film (FUJIFILM).

Nevertheless, there are some disadvantages while using it. The time needed to produce the mark might be quite long, and for this project, it is also interesting to measure the pressure in a hemispheric surface. So, the contact between this one and the film might not be good enough.

4.5 Army clay head form

This head form (Figure 4.11) is a modification of the head form defined in N.I.J. 0106.01 standard for ballistic penetration tests. It is possible to conduct an experiment in sagittal and coronal positions. These specific head forms have a cavity to be filled up with clay. Clay has to be conditioned and verified prior to tests in order to have less variability in mechanical properties. The verification of the clay is done with free-fall drop test of a 1039 ± 5 g ball from 2000 ± 5 mm. The steel ball has 63.5 ± 0.05 mm diameter.

There is no correlation between this test methodology and personal injury. The system is foreseen for measuring the BFS of armour during an impact.

Figure 4.11.- Army clay head form with Weible clay.

In the standard, the spaces have to be filled with Roma Plastilina N°1 clay. This clay is the standard from the USA. The clay needs to be heated up to reach adequate rheological properties, while the tests are conducted at room temperature. This introduces a gradient of temperature and changes the behaviour of the clay. Weible clay is specified in the VPAM standard. This clay also needs a higher temperature than room temperature but lower Roma

N°1; thus, its properties vary less while the tests are taking place. Furthermore, for ease of purchase Weible clay was used in this research.

Army clay head form has different associated problems: one of them is the scatter of the data; there are more significant factors – such as humidity or use of the clay – that can influence this variable. Secondly, the petals might affect the BFD of the helmet, either by holding the helmet or modifying the flow of the clay (National Research Center, 2014; Gotts, 2015). A test was conducted for checking this problem. A prescale film was placed between the helmet and the clay head (Figure 4.12).

Figure 4.12.- Clay head with a prescale film.

After firing a 9 x 19 mm ammunition into the helmet, the films showed two parallel lines produced by the petals. Moreover, the film was broken due to the more significant deformation of the shell of the helmet and the clay than the film. The red stain in the film was not clear enough attributable to the soft back face (Figure 4.13).

Figure 4.13.- Prescale film after the test (arrows point the petal marks).

The Peepsite head form (Figure 4.14) reduces these potential problems with this existing clay head form. However, it is not accepted in any standard.

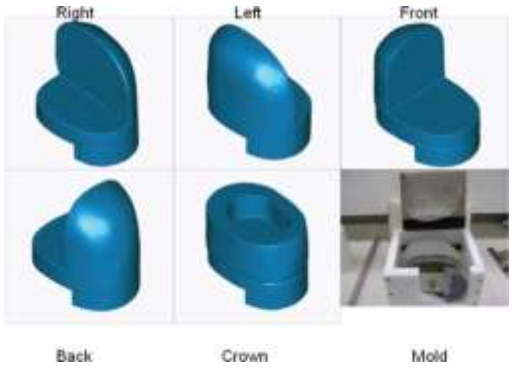

Figure 4.14.- Peepsite head form.

4.6 Ballistic Load Sensing Head form (BLSH)

BLSH system consists of load measuring head forms to assess the ballistic impact protection performance of helmets (Figure 4.15). The BLSH enables direct measurement of the dynamic loads imparted to the skull by the deformation of a ballistic helmet caused by non-penetrating projectiles. The forces may be correlated with the risk of injury, such as skull fracture (Pintar et al., 2013).

Nonetheless, there is no suggested correlation between the BLSH force data and injury data, (N. A., 2012) it would be easier to expect some injuries from a force value than from a DOP in the clay. Stress in the cranial bone increases when the contact between the shell and the skull is initiated.

Figure 4.15.- Ballistic load sensing head form.

The BLSH is used in this study to evaluate the force produced by a ballistic helmet during an impact and the acceleration produced in the centre of the head form. It is equipped with an array of seven uniaxial load piezo-electric sensors per impact zone. Each one is able to measure up to 22 kN. A skin simulating pad covers the sensors to simulate better the skull response. The head form is mounted on a flexible neck from the Hybrid III anthropomorphic test device. The Hybrid III 50th Percentile Male Crash Test Dummy is the most widely used in the world. It accurately simulates the human dynamic response.

4.6.1 Abbreviated Injury Scale (AIS)

The AIS created by the Association for the Advancement of Automotive Medicine is an anatomically based, global damage scoring system that classifies each damage according to its relative importance on a scale from 1 to 6. The AIS provides standardised terminology to describe injuries and ranks the severity of the injury.

The AIS is monitored by a scaling committee of the Association for the Advancement of Automotive Medicine. Current AIS users include health organisations for clinical trauma management; systems development engineers, and researchers for epidemiological studies. This rank allows choosing the level of injury desired easily and what type of injury would be expected. Injuries are ranked on a scale of 1 to 6, with 1 being insignificant and 6 an unsurvivable damage (Table 4.3). This rank signifies the chances of survivability related to

damage. The AIS is not an injury scale, in that the difference between AIS 1 and AIS 2 is not the same as the one between AIS 4 and AIS 5 (Gennarelli and Wodzin, 2006).

AIS Code	Injury	Description
1	Minor	Skin/scalp: abrasion, superficial laceration.
2	Moderate	Skin: major avulsion. Vault fracture: simple, undisplaced.
3	Serious	Basilar fracture. Total scalp loss. Single contusion cerebellum.
4	Severe	Vault fracture: complex, open with torn, exposed or loss of brain tissue. Small epidural or subdural hematoma.
5	Critical	Major penetrating injury (> 2 cm) Brain stem compression Large epidural or subdural hematoma
6	Unsurvivable	Massive destruction of both cranium and brain

Table 4.3.- AIS classified head injury.

4.6.2 Head Injury Criterion (HIC)

Some experimental measures have been developed by the automotive and sports industries to assess injury risks for low speed, high mass impacts. Although different criteria have been proposed, there is no consensus on the approach to use to cover the full spectrum of possible blunt impact head injuries. The Head Injury Criterion is a measure of the likelihood of head injury arising from an impact, taking into account the time length of the event and the mean value of the acceleration. The HIC can be used to assess safety-related to vehicles and sports equipment (Marjoux et al., 2008). It is accepted for low-speed non-penetrating impacts (Frank et al., 2011), but not high-speed impacts like a ballistic impact.
It is defined as:

$$HIC = MAX\left(\frac{1}{T_2 - T_1}\int_{T_1}^{T_2} a(T)dT\right)^{2.5}(T_2 - T_1) \qquad \text{Eq 15}$$

where
T is time. $T_2 - T_1$ is limited to a precise value, usually 15 ms or 36 ms (Eppinger et al., 2000).
a is acceleration measured in G's.

Injuries related to the HIC value can even lead to death (Table 4.4).

AIS	HIC range
0	0-134
1	135-519
2	520-899
3	900-1254
4	1255-1574
5	1575-1859
6	>1860

Table 4.4.- AIS equivalence to HIC (Greenwald et al., 2008).

The main drawback is related to the time length studied. For an automotive accident, 15 ms is appropriate, while for a ballistic impact, it is exceptionally long. It can last a couple of ms.

4.6.3 Blunt Object Skull Fracture Criterion (BC)

Blunt criterion predicts head injury from blunt impact (Sturdivan et al., 2004). This type of impact is similar to the one produced by the armour. BC is applied for head impacts only with blunt (<40 mm radius) objects. There are lots of data from automotive accidents, and it can also be used for less-lethal weapons or the BABT. The criterion is based on the force required to produce depressed skull fractures (Yoganandan et al., 2014).

It is defined as:

$$BC = \ln\left(\frac{E_k}{m^{1/3} D t_s}\right) \qquad \text{Eq 16}$$

Where
E_k is the impact kinetic energy in Joules,
m is the mass of the impacted individual, in kg
D is the diameter of the projectile in centimetres (if impact area is circular),
t_s is the thickness of the skull in millimetres.

The BC has been demonstrated to correlate very well with experimental data published from cadaver and animal studies, but still needs confirmation for head impacts (Raymond, 2008). Table 4.5 shows the proposed BC levels compared to the AIS criterion.

	Proposed Tolerance Levels (kN)	Equivalent AIS
No Skull fracture	<2.2	-
Minor Depressed Skull Fracture	2.2 – 5.5	2 /3
Major Depressed Skull Fracture	>5.5	4

Table 4.5.- AIS equivalence to BC.

4.7 Development of new support for samples with a helmet

In order to test the samples in the head forms, support was designed to attach the samples to a regular helmet. The front part of the helmet was removed for placing flat samples 100 x 100 mm. The ballistic limit is not very sensitive to the curvature, not as the BFD (Tan, 2014). Using flat samples simplifies the support and the manufacture of the ceramic tiles. Samples are firmly held by their four sides in the support. The frame is attached through six bolts to a Schuberth helmet. First of all, the helmet was tested for checking if it was able to support the load of the rifle projectile (Figure 4.16). A 7.62 x 39 mm projectile was fired at 745 m/s. Due to the lack of support, the tile and composite were removed during the impact. It produced a net indentation in the clay head form.

(a) (b) (c)

Figure 4.16.- Initial concept support. (a) helmet support after the test, (b) head form after the test and (c) BFD of the support.

The helmet was though enough for supporting the load of the impact. The final design allows varying the standoff between the head form and the helmet (Figure 4.17) from some mm – it depends on the head form or the sample tested – up to 50 mm. Basic configuration weighs 750 g.

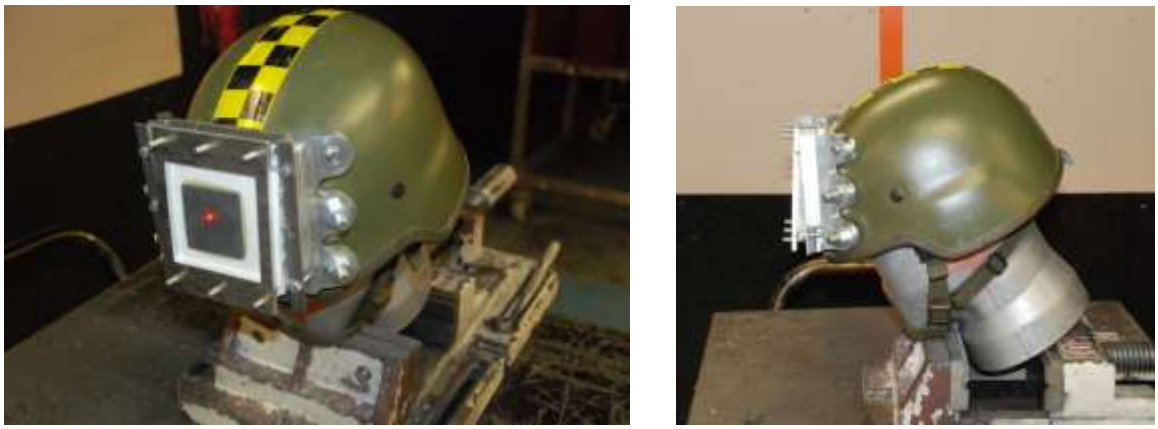

(a) (b)

Figure 4.17.- Final support and helmet.

4.8 Traction testing machine

The testing machine Zwick Roell Kappa 050 DS can test various mechanical properties of the materials (Figure 4.18). A testing machine with a precise speed of +/-0.1 % of the set speed in the range of 0.0000167 to 100 mm/min (no-load or constant load) measurement (average over 5 sec or 10 mm) with a load capacity of 50 kN (Table 4.6). Tensile tests and bending tests were done for this project.

Figure 4.18.- Testing machine Zwick Roell Kappa 050 DS.

Load capacity	50 kN
Test area width (between drive screws)	610 mm
Test area height	1350mm
Test speed	0.001 mm/h to 100mm/min
Crosshead speed accuracy	+/- 0.1 %
Resolution of stroke encoder	0.068 nm
Frame dimension	860 x 655 x 2310 mm
Weight	840 kg

Table 4.6.- Specification properties for testing machine Zwick Roell Kappa 050 DS.

4.9 Computed Tomography (CT)

The Research Nacional Centre of Human Evolution (*Centro nacional de investigacion de la evolución humana* - CENIEH) belongs to the national research network of Spain. It has a Micro-Computed Tomography laboratory with a GE Phoenix v/tome/x (Figure 4.19) and a Scanco Medical µCT 80. With this equipment, measurements of the area, volume, porosity, thickness, density of the samples are done, even for different parts of a composite or mixture of material. The image processing is done with VG studio software.

Figure 4.19.- Phoenix v/tome/x s (GE Measurement & Control).

The axial microtomography provides high resolution/high precision 2D images of the internal structure of the sample without destroying it. From these 2D images, a 3D model can be recreated and produced a digital reconstruction of the object. These representations show the internal structure and allow for virtual evaluations and morphometric analyses (CENIEH).

4.10 Scanning Electron Microscope (SEM)

Scanning Electron Microscope (SEM) magnifies the samples with a beam of electrons. It allows images up to 300000x. SEM needs conductive samples to perform better; nevertheless, it is possible to cover non-conductive samples with gold. A beam of electrons and electromagnets creates the images instead of the light and optical lenses of a traditional microscope. SEM JEOL JSM-6460LV with an X-Ray detection system INCA (Figure 4.20) can also determinate the elemental composition of the samples.

Figure 4.20.- SEM JEOL JSM-6460LV with an X-Ray detection system INCA.

5 STUDY OF THE LOAD SUFFERED BY THE HEAD

5.1 Introduction

It is needed to assure that the load of the skull is lower than the injury risk threshold. An actual Belgian helmet is going to be tested with two different systems. First one is the clay head form, which relies on the indentation of the plasticine. The second one is the BLSH, with multiple sensors to evaluate the force generated during the event. The results will be used to evaluate the aptitude of the concept of protection for rifle ammunition; part of this was already published, as mentioned in the point 1.1 (Miranda-Vicario et al., 2018).

5.2 Test procedure

9 x 19 mm ammunition was fired into the considered helmet wore by the BLSH. The target is placed 5 m far away from the muzzle. The projectile velocity is measured with a double optical basis DRELLO LS19 positioned in the middle of the trajectory of the projectile. Correction of the velocity allows taking into account the deceleration of the projectile form the measurement point to the impact point (Payne and O'Rourke, 2017).

Twenty-two helmets were tested, shooting four times at each helmet on specific locations (front, back, left and right). Tests were conducted with the two head surrogates: clay head form wore twelve helmets and BLSH the rest, ten helmets; with a total of 81 fair tests (Table 5.1).

	Front	**Back**	**Right**	**Left**
US Army clay head	12	12	12	11
BLSH	8	8	9	9

Table 5.1.- Tests conducted for each surrogate.

The NIJ standard (National Institute of Justice, 1981) defines the order of the impacts. After every impact, each helmet was removed from the head surrogate. In case of the clay head, the BFS was measured, and the next position of the helmet was tested. For the BLSH, the same position was tested for all helmets, and then the head surrogate was modified to test the next spot.

5.3 Results and discussion

For the US Army clay head form, the indentation produces upon every impact was measured with a calliper (Figure 5.1). Table 5.2 and Figure 5.2 present the results of the impact velocity of the projectile, the position impacted into the helmet and the measured BFS.

Helmet	Impact velocity (m/s)	Position	BFS (mm)
10	304	L(eft)	3.10
12	309	R(ight)	6.00
12	312	L	3.40
11	313	B(ack)	11.50
1	320	B	8.47
1	321	F(rontal)	1.18
12	322	B	10.40
1	323	R	0.84
10	323	B	4.40
12	324	F	6.80
11	325	F	6.00
10	332	R	3.00
11	333	L	4.50
9	334	F	8.44
9	334	L	2.40
10	334	F	7.60
9	335	R	2.60
9	339	B	7.42
11	345	R	5.00
4	346	R	2.01
2	347	F	4.68
3	348	L	3.90
2	349	B	10.28
2	349	R	1.85
4	349	B	14.27
5	350	B	2.12
7	350	F	10.70
3	351	F	10.43
3	351	B	7.63
3	352	R	4.90
7	352	B	9.30
4	353	L	4.80
7	353	L	4.00
2	355	L	2.81
4	355	F	13.83
8	358	R	2.10
7	364	R	3.00
6	366	L	3.20
5	367	R	6.70
6	367	R	3.80
5	368	F	4.40
8	371	B	17.60
5	372	L	9.10
8	372	L	2.80
8	373	F	12.80
6	376	F	6.09
6	376	B	16.50

Table 5.2.- Experimental data from the clay head form.

Figure 5.1.- US Army clay head after a 9 x 19 mm ballistic impact protected by the helmet in the frontal area.

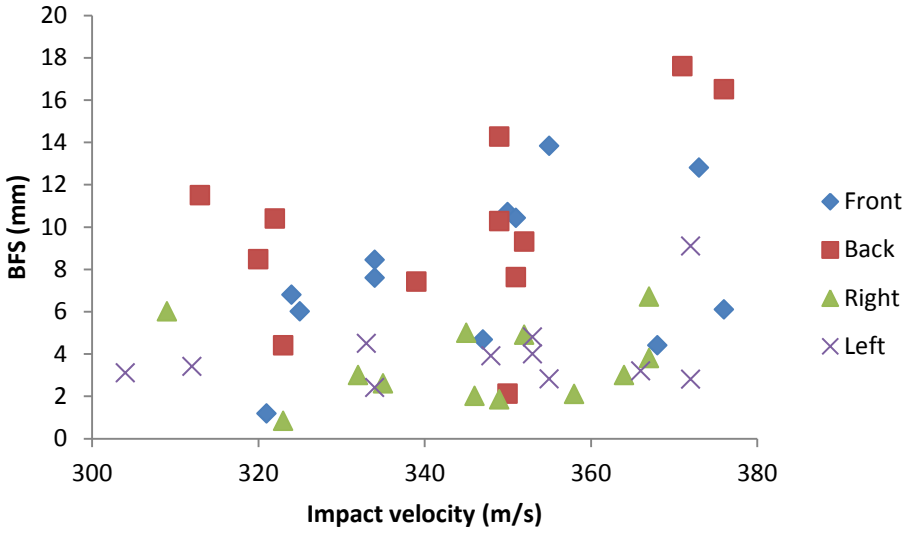

Figure 5.2.- BFS versus impact velocity.

Data present a significant scatter thus complicating the statistical analysis. The first examination shows that there are two different populations for the BFS; one population is the data from lateral impacts, as shown in Annex A for further details. In this case, the BFS is quite insensitive to the velocity of the projectile (Figure 5.3). The second group is front and back impacts. The BFS increased with velocity in the second population (Figure 5.4). This different behaviour was also observed for another type of aramid helmet (Palta et al., 2018), and it might be caused by the local geometry of the helmet (Pasquali and Gaudenzi, 2017).

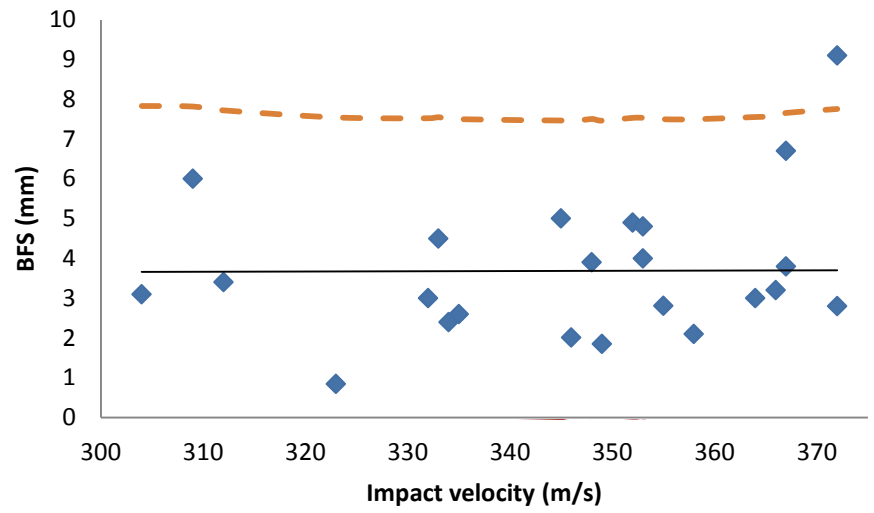

Figure 5.3.- BFS as a function of impact velocity for both lateral impact conditions, data with their linear regression and 95 % upper confidence interval (dashed line). Lower confidence value is lower than 0.

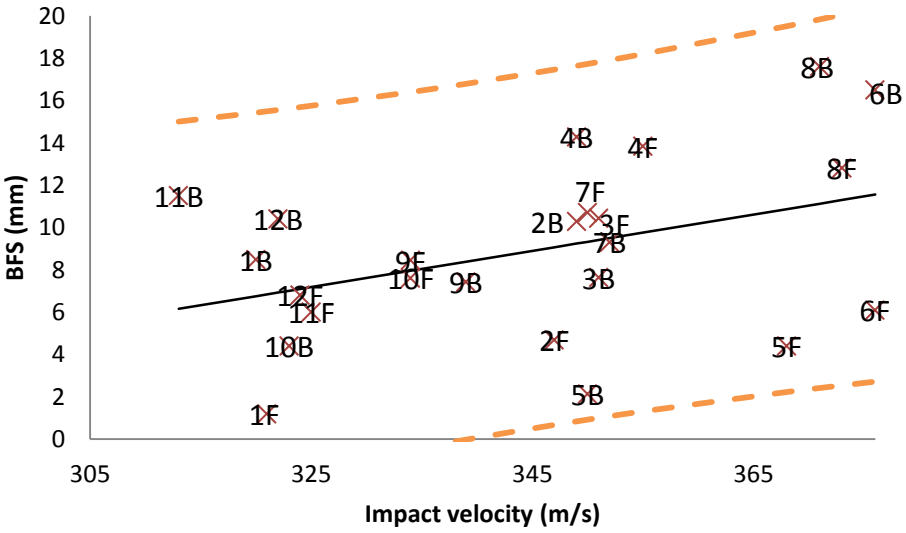

Figure 5.4.- BFS as a function of impact velocity for both front and back data with their linear regression and 95 % confidence interval (dashed lines).

Once the populations were characterized with their normal distributions, it was possible to calculate the probability of the BFS for each specific impact; connecting and arranging each test to its percentile. Working with the probability allows grouping regarding different parameters, such as the helmet or the position, and studying its influence. Removing the effect of the units of the event measured facilitates the comparison of the data regarding any parameter. If the elements of a given group presented similar percentiles values, the parameter

that defines that group would have no influence; but if the elements of the groups were isolated, the parameter would influence the outcome of the experiment (BFS, in this case). This comparison was made in Figure 5.5 for each helmet (numbered in X-axis); it was possible to observe some differences despite a small number of data.

Helmet 4 exhibited similar behaviour for the back and front position, BFS produced by this helmet is larger than the average. Helmet 5 behaves in the contrary way, producing less BFS than the average. Helmet 4 and 5 exhibited very similar behaviour between the front and back position, unlikely the other samples.

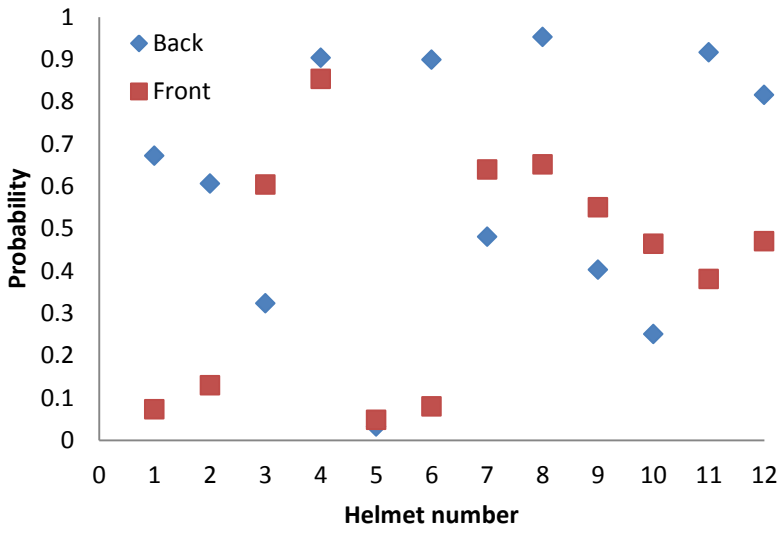

Figure 5.5.- BFS percentile for every helmet.

Data from the BLSH is presented below (Figure 5.6 and Table 5.3). BLSH provides other interesting parameter like the duration of the interaction between the helmet and the head (less than 1 ms) that allow to calculate the head form impulse. Force presents a wide distribution again, but they can be arranged in only one population.

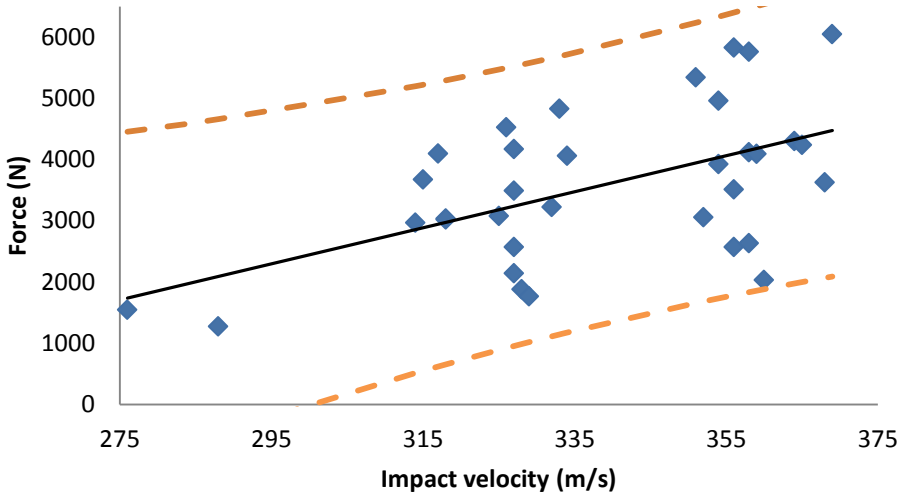

Figure 5.6.- Peak force vs impact velocity, data with their linear regression and confidence interval 95 %.

Helmet	Position	Velocity (m/s)	Force (N)	Percentile	Impulse (kg m/s)	HIC
J	(R)ight	276	1545	0.072	0.70	49
J	(L)eft	288	1273	0.952	0.65	39
H	(F)ront	314	2970	0.457	1.06	38
F	F	315	3674	0.91	1.49	
E	(B)ack	317	4098	0.866	1.36	238
F	B	318	3021	0.517	0.96	122
G	F	318	3038	0.595	1.19	29
H	B	325	3076	0.46	1.45	129
E	F	326	4525	0.189	1.39	
F	R	327	2570	0.289	1.29	54
G	L	327	4169	0.896	1.61	835
G	B	327	3490	0.775	1.69	270
H	R	327	2143	0.524	1.13	147
H	L	328	1882	0.543	0.78	97
F	L	329	1763	0.486	0.88	74
E	L	332	3222	0.812	1.35	284
G	R	333	4829	0.018	1.80	403
B	R	334	4056	0.939	1.71	84
D	B	351	5344	0.455	2.06	997
A	F	352	3058	0.215		
C	B	354	3923	0.437	1.61	261
J	F	354	4958	0.07	1.60	358
A	B	356	2569	0.814	1.22	160
B	B	356	5827	0.091	2.10	387
D	F	356	3513	0.216		
A	R	358	2634	0.072	1.13	
B	L	358	5759	0.721	1.89	892
I	F	358	4117	0.465	1.54	78
C	R	359	4091	0.489	1.85	142
A	L	360	2031	0.934	1.02	141
D	R	364	4301	0.26	1.65	192
C	L	365	4240	0.912	1.79	317
D	L	368	3625	0.146	1.45	170
E	R	369	6047	0.426	2.15	1237

Table 5.3.- Experimental data from the BLSH.

The force-normalised results were grouped per helmet. There are differences for every helmet as occurred with the helmets tested with the clay head form (Figure 5.7).

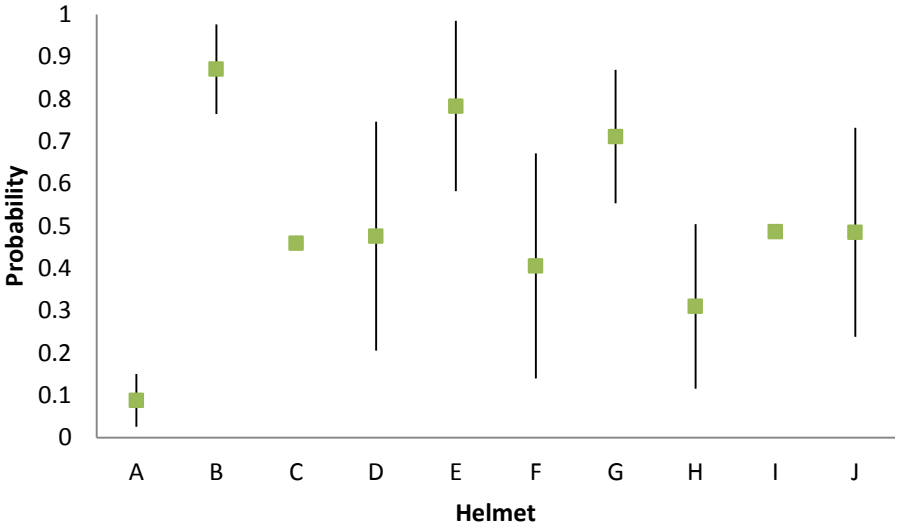

Figure 5.7.- Force percentile and grouped by helmet tested (average + standard deviation). For helmet "C", the variability is not noticeable in the plot; whereas for the helmet "I", there was only one fair test.

The two most extreme situations were compared; in this case, helmets "A" and "B", similar to the helmets 4 and 5 from the clay head form. The impact velocity was the same for these both cases. Moreover, there was no clear difference from the retrieved projectiles shapes nor the affected area of the helmets (Figure 5.8).

Ammunition test "A"

Ammunition test "B"

Figure 5.8.- Projectiles after the impact (Ammunitions from tests "A" and "B", frontal and rear view).

As no visible differences were observed, it seemed the observed scatter could be attributed to the variability of each helmet, due to the manufacturing process, the service period, and the inherent spread of the ballistic tests.

Also, the acceleration of the head was studied. HIC was calculated with the BLSH accelerometers data, as explained in point 4.6.2 (Figure 5.9).

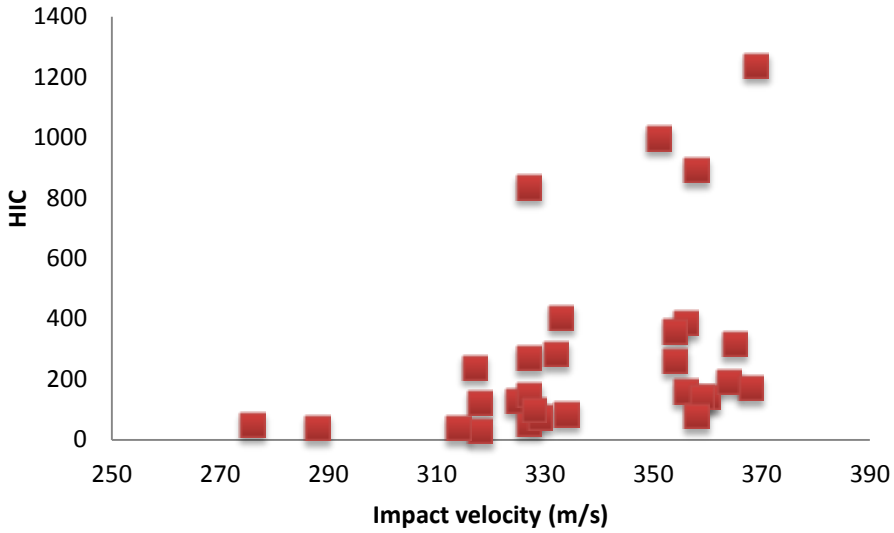

Figure 5.9.- HIC vs impact velocity.

The points with the highest values become form helmets B, D, E and G. These helmets were the ones that transmitted more force (B, E and G). There is a link between the force and acceleration of the head produced by the impact. However, the HIC is not a uniform cloud of points, and there is a gap with no data points. The existence of this gap is not evident, and it might be produced by the way the value of the HIC is calculated.

Checking this criterion, the vast majority of the impacts produces a low HIC and would produce minor injuries.

The residual energy that loads both surrogates was compared on the same scale, to validate if the data is exchangeable, and it will provide another criterion to relate with injury criteria. For the US Army head form, the VPAM standard shows how to estimate the residual energy from

the indentation (VPAM, 2010). Residual energy is quite low, and in any case, it is smaller than 12 J (Figure 5.10).

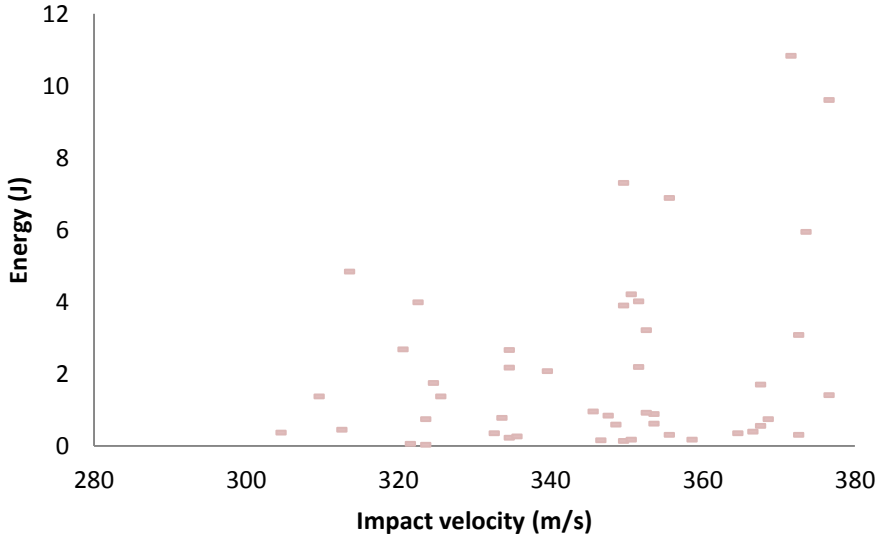

Figure 5.10.- Residual energy for the clay head form estimated with the VPAM standard.

For the BLSH, it is needed to estimate the residual energy with the data provided from the force sensors and the affected region of the helmet. From visual inspection, the affected part is maximum about 50 mm radius circle, but only a fraction assists to load the head form. The actual contact surface of the helmet with the head is smaller, and it is going to be taken in account the radius of 30 mm. The minimum area would be a 4.5 mm radius circle, the calibre of the ammunition. Dividing the momentum by the affected region, the velocity is estimated. Thus, the kinetic value was assimilated to the residual energy that reaches the head (Figure 5.11), further details shown in Annex B.

The values of the residual energy estimated from the clay head form were lower than the minimum of the energy values obtained from the BLSH. The maximum values agreed with the ones estimated by Hisley et al (Hisley et al., 2011). As there was no head form, the standoff from the head to the helmet was assumed to be 12.7 mm and 19.05 mm. The actual standoff between the BLSH and the helmet studied is 14.9 mm.

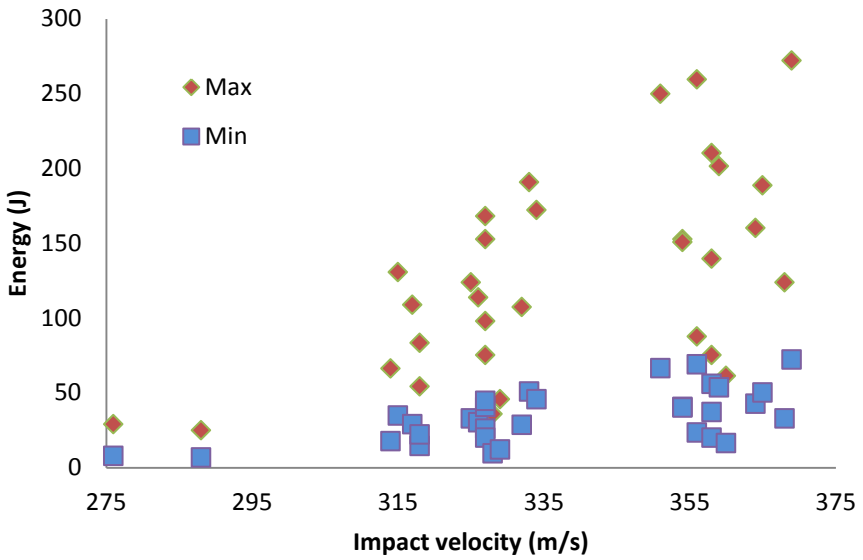

Figure 5.11.- Residual energy for the BLSH.

5.4 Conclusions

Four parameters were studied from this series of tests: BFS, force, HIC and energy.

BFS shows independence from the velocity of the projectile, which makes more difficult to link it with any injury criterion.

Force shows a relationship with the velocity of the projectile and provides useful data to set an acceptable level for helmets, this limit could be the injury threshold. However, it is difficult to assess the correct level for an injury threshold, and it is necessary to take into account the big scatter. The relationship is linear and have similar scatter along all the velocity range studied, which facilitate the statistical analysis allowing to determinate the probability of the level of load for an event.

HIC takes successfully in account the duration and value of the peak acceleration, but the relationship with the impact velocity is not linear and shows a gap. This behaviour challenges the link between the HIC and impact velocity.

Residual energy might be an excellent value to check the results, but at this stage is only estimation.

As a novelty, the relationship of these four parameters among them and with the impact velocity and the way to compare them are explained in this text. The research shows the better aptitude of the force among the others.

Regarding to the force data, the vast majority of the shots are below the 5000 N limit. Only four impacts exceed this value. Similar happens for the HIC, where these four cases also surpass a HIC of 500. For the majority of the shots, these criteria show a low risk of injury.

However, for the energy criteria, there is a disparity. Injury criteria from sports consider that for an impact of 20 J a concussion could occur (Mills, 2007), with an energy ranged 45 J may produce non-loss of consciousness concussion and for 75 J may generate a loss of consciousness for longer than 1 minute (McIntosh and McCrory, 2000). Moreover, the risk of injury from BABT, more specifically Behind Helmet Blunt Trauma (BHBT) has already been reported in literature for the same ammunition (at the top range of velocity studied) and similar composite helmets (Freitas et al., 2014b; Hisley et al., 2011; Palomar et al., 2018; Rafaels et al., 2015b). With all these criteria in mind, residual energy estimated with clay head form and the VPAM standard is far from indicating a risk, and the BLSH shows a certain risk. This cannot be due to the different standoff of each surrogate (6.1 mm larger for the clay head form). It would produce a deeper BFS, from 17.6 mm to 23.7 mm. Subsequently, the estimated energy increases from 10.84 to 18.74 N, with the VPAM estimation method; these values are still under the concussion threshold.

A proposal to estimate the residual energy from the force values shows the disparity from the VPAM standard and experimental results. Further investigation is needed to correlate appropriately the estimation.

The distance between the head and the helmet plays a critical function transmitting the load to the head. This parameter will be very interesting to study to reduce the load of the rifle ammunition.

6 OPTIMISATION OF THE BALLISTIC PROTECTION

6.1 Impacts into steel plate

The study of the deformation of the core of the projectile is imperative to increase the effectiveness of the armour and also to have reliable data to implement in numerical simulations. This mild steel rifle projectile has been less studied, as there is more extensive literature about harder projectiles impacted in ceramics (Behner et al., 2016; Hogan et al., 2017; Savio et al., 2011b; Woolsey et al., 1989; Zinszner et al., 2015). In our case, the core is soft and deforms during the impact with hard steel plate. The smaller range was studied by (Hamouda and Hashmi, 1997; Wilkins and Guinan, 1973), analysing several metal projectiles but for slower velocity range. The dynamic impact of the core into the target is driven by the mechanical properties affected by the impact velocity. Nevertheless, current testing systems do not replicate a ballistic impact; compression machines or Hopkinson bars are capable of determining different strain rates, but the impacting core is subject to deceleration while the impact and the energy is limited to the kinetic energy. The core collapses in several mechanisms of deformation, depending on the impact velocity.

7.62 x 39 mm M43 projectiles were fired into hardened steel plate acting as a rigid boundary; the projectile was not able to do significant damage to the plate, until a certain velocity. The impacted cores were retrieved and analysed.

6.1.1 Material

The rigid wall was used to focus on the deformation behaviour of the projectile core. The rigid target consisted of a 12 mm thick steel armour plate, 480-540 HBW hardness, 1250 MPa yield strength and around 1600 MPa tensile strength. The ferrous alloy contained mainly Mn, Si and C, as shown in Table 6.1. It was manufactured by SSAB, named as ARMOX 500.

C (Max %)	**Si (Max %)**	**Mn (Max %)**	**P (Max %)**	**S (Max %)**	**Cr (Max %)**	**Ni (Max %)**	**Mo (Max %)**	**B (Max %)**
0.32	0.4	1.2	0.0010	0.003	1.0	1.8	0.7	0.005

Table 6.1.- Elemental analysis of the armour steel rigid target.

6.1.2 Test procedure

Thirty-three 7.62 x 39 mm M43 were fired onto the steel plate, with the impact velocity ranging from 200 to 1125 m/s. The plate was clamped on one side, and all shots were placed close to the clamped side. The thickness and size of the plate prevented it from moving when impacted. Projectiles rebounded after the impact onto the steel plate, and they were found in the nearby of the target.

6.1.3 Results and discussion

The projectile was entirely stripped of its jacket when impacted onto the rigid wall. The core impacted the plate, suffering a plastic deformation and an important reduction of length. This reduction depended on its impact velocity (Figure 6.1). The core deformed in a flat shape following the flat geometry of the surface of the steel plate; this description illustrates the behaviour of the high-hardness steel target. No significant damage or bulging of the armour plate was observed after the tests while impact velocity was 900 m/s. From that velocity; partial penetration occurred, creating small craters in the armour and the core deformed following that shape.

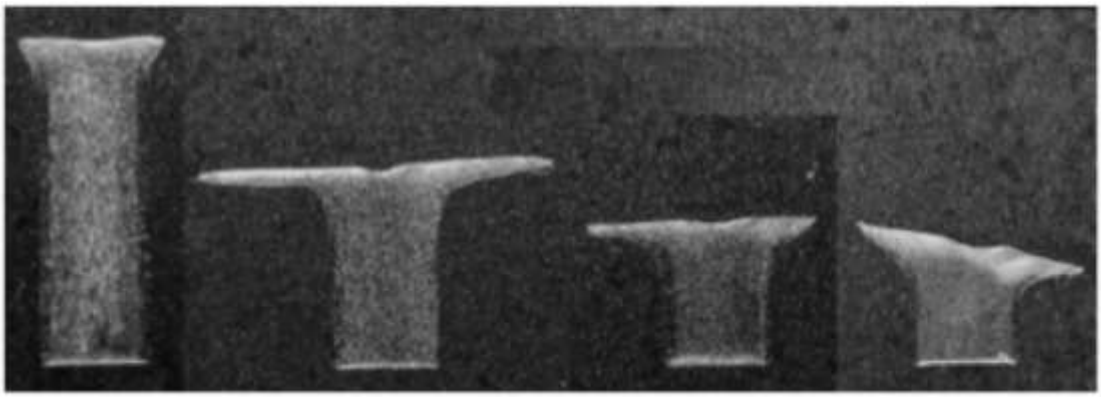

(a) (b) (c) (d)

Figure 6.1.- Shape of the core after impacting rigid wall at: (a) 203 m/s; (b) 466 m/s; (c) 622 m/s; and (d) 740 m/s.

There were different deformation patterns for the projectile as a function of the impact velocity. For low velocities, there is a mushroom formation. The front part of the cylinder bulges out due to compression while the rear part stays almost undeformed. At 203 m/s, the

diameter of the tip increased from 4.00 to 7.43 mm (Figure 6.2). These patterns are different from impacting a softer steel target, such as AH36 steel, where the retrieved cores are blunted (Shin et al., 2018). The metallographic picture extracted from the cut section of the projectile showed the front grains compressed and the neighbouring grains flowing towards the sides (Figure 6.3). The metallographic analysis was done after polishing the section of the core. The four stages for polishing (P280, P500, P1000 and P2000) took in total around half an hour. Finally, the sample was plunged in Nital 3 % for around 5 seconds to clearly revealed its structure.

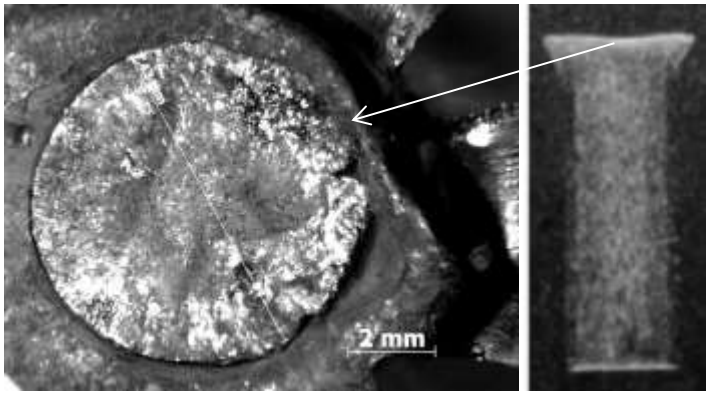

Figure 6.2.- Tip of the core of the projectile impacted at 203 m/s.

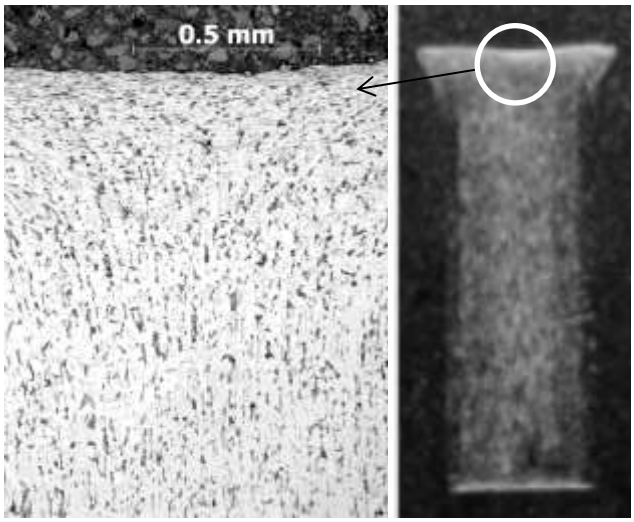

Figure 6.3.- Metallographic view of the tip of the core of the projectile impacted at 203 m/s.

For faster projectiles, a petalling pattern appeared (Figure 6.4). Several major cracks propagated radially toward the symmetry axis due to tensile hoop stresses forming several petals (Teng et al., 2005). The impact and the geometry of the core produced a cavity

surrounding the axis of the projectile. The metallographic analysis revealed that the deformed grains were thicker in the edge than in the centre (Figure 6.5).

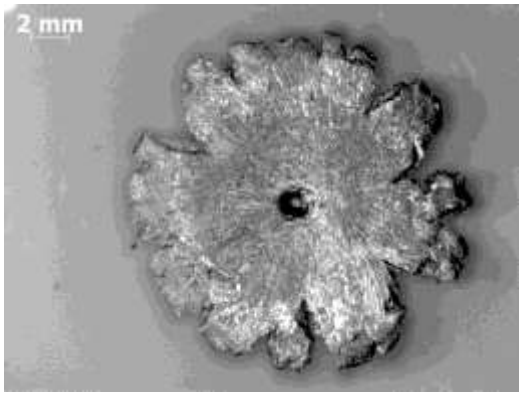

Figure 6.4.- Tip of the core of the projectile impacted at 466 m/s.

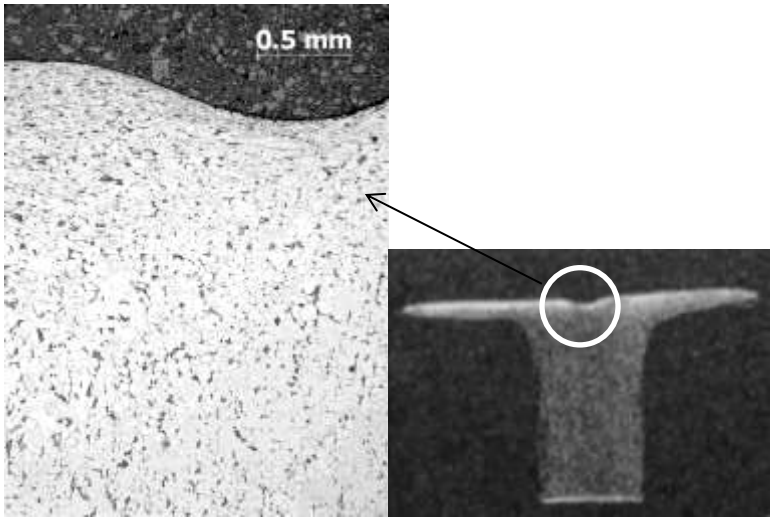

Figure 6.5.- Metallographic view of the tip of the core of the projectile impacted at 466 m/s.

A third fracture pattern appeared when the impact velocity was in the range of 507 to 636 m/s. It was very similar to the mushrooming, but part of the projectile was dissociated from the core and eroded. These cracks appear at the base of the petals, cutting them apart. There are thermal stress concentrations due to the friction of the petals of the projectile widening along the target; this movement produces high adiabatic shear till fractures in the base of the petals cut them apart (Figure 6.6).

(a) (b)

Figure 6.6.- Core after impacting rigid wall at (a) 550 m/s (Illustrates the cracks at the base of the petals) and (b) 573 m/s (Petals removed from the core).

Figure 6.7 and Table 6.2 show that the residual mass of the core dropped considerably around that velocity.

	Impact velocity (m/s)	Residual length (mm)	Residual weight (g)
RW1	203	17.21	3.607
RW2	242	16.10	3.604
RW3	466	11.04	3.617
RW4	486	11.00	3.601
RW5	507	10.01	2.036
RW6	550	9.00	3.228
RW7	573	7.95	2.343
RW8	580	8.40	2.215
RW9	622	7.20	3.605
RW10	636	8.10	2.317
RW11	640	7.53	2.314
RW12	677	7.20	2.166
RW13	691	6.76	2.166
RW14	705	6.85	1.943
RW15	728	6.95	2.050
RW16	740	6.47	2.040
RW17	745	7.01	2.182
RW18	797	6.07	1.864
RW19	797	6.07	1.864
RW20	802	5.93	2.010
RW21	802	5.93	2.010
RW22	832	6.13	1.828
RW23	842	6.13	1.828
RW24	866	5.69	2.004
RW25	920	5.84	2.556
RW26	920	6.17	2.394
RW27	926	5.95	2.546
RW28	1017	5.40	2.775
RW29	1028	6.18	3.057
RW30	1107	6.45	3.278
RW31	1118	6.82	3.265
RW32	1124	7.38	3.292
RW33	1132	7.10	3.268

Table 6.2.- Experimental data from the retrieved mild steel core impacted onto the rigid wall.

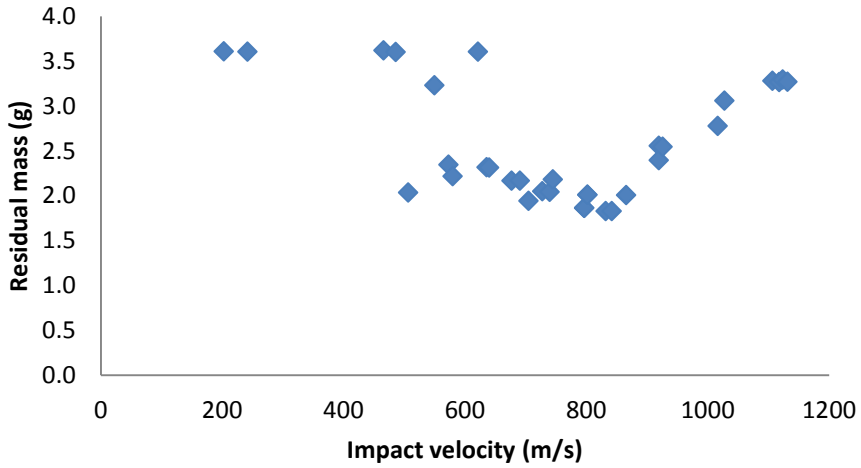

Figure 6.7.- Residual mass of the core as a function of impact velocity of the projectile into a rigid wall.

Most of the projectiles had either all or none of the petals, only one of the cores had partially removed the petals (Figure 6.6.a). Thus, most of the petals are removed almost simultaneously and the mass of the projectile drops abruptly. This means that there is a critical length of material when this material breaks the chip. This process is comparable to machining by chip removal, where the steel plate acts as the tool with a contact angle of 0 degrees (Figure 6.8).

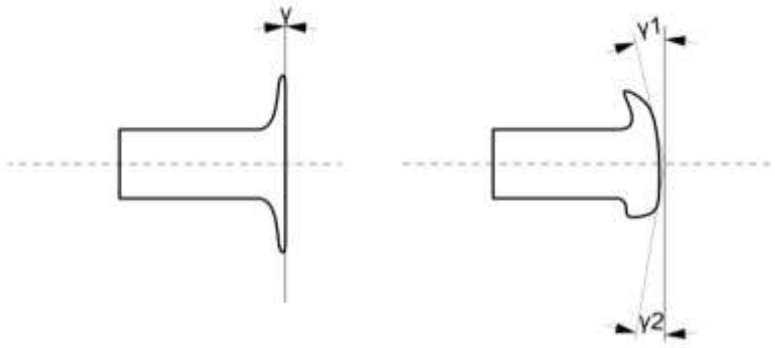

(a) (b)

Figure 6.8.- Rake angle for (a) low velocity and (b) high velocity impacting onto the rigid wall.

From velocities from 636 to 900 m/s, the high strain region of the projectile is eroded, and it mainly remains the part of low strain and undeformed portion of the core (Jones et al., 1984). This process produces a more irregular mushrooming with some cracks, and self –hardening

of the material. It is possible to observe that this process of reduction of mass for the core starts with higher impact velocities. The microstructure of metal changes during the deformation process, the grains change their shape, and the internal structure may change (Humpreys and Haterly, 1995); due to of the impact, the temperature of the projectile increases. The grains, as shown in Figure 6.9, were involved in the high rate deformation, but there was no evidence of recrystallisation, as shown for the tip of the core of the projectile impacted at 740 m/s.

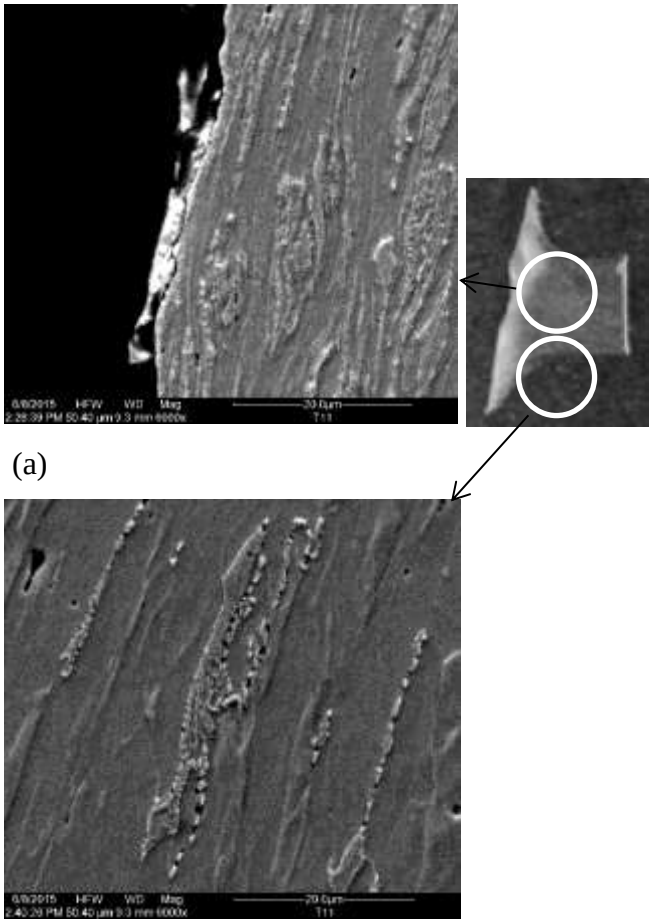

(a)

(b)

Figure 6.9.- Sample T11 740 m/s, metallographic picture (a) centre and (b) side.

Impacts faster than 900 m/s produced a crater in the armour steel and the core deformed following the shape of the crater. The apparition of a crater at high impact velocities is due to the dynamic tensile strength of the material, as explained in (Manjit Singh et al., 2008). The faster the impact velocity, the bigger the crater became. The recovered cores reflect this effect of perforation. The mass of the recovered core was reduced, but less than in lower velocities (Figure 6.7). The energy needed to create the crater is not enough to explain the change of

behaviour of the residual mass, as it is possible to find projectile with a mass between the 3.2 and 2.3 g, the values of gap between 507 to 636 m/s.

The deformation of the core for impacts at this range of velocities was limited by the crater in the armour plate. When the penetration started; the mushroom curved and reached its final shape. There was no change of diameter in the back part of the projectile core. In this case, the perforated armour acted as a tool with a variable negative rake angle (Figure 6.8 and Figure 6.10). Therefore the core was subjected to a more significant shear deformation; thus, the limit of the material was reached which shorter and more irregular chips (Ohbuchi and Obikawa, 2005). The core needed more energy to advance due to the confinement of the rake angle while perforating the steel armour (Jones, 1972). This would explain the reduction of erosion of the core with the increment of the impacted velocity (Figure 6.10).

(a) (b) (c) (d) (e)

(e) (f) (g) (h) (i)

Figure 6.10.- Core after impacting rigid wall at (a) 486 m/s, (b) 550 m/s, (c) 572 m/s, (d) 797 m/s, (e) 838 m/s, (f) 842 m/s, (g) 920 m/s (h) 1016 m/s and (i) 1027 m/s.

Erosion of the projectile seems to be related to the shape of the target. The apparition of a deeper crater, thus a smaller negative rake angle, provoke less reduction of mass. The level of deformation and erosion was assessed by measuring the residual length as a function of impact velocity for the different targets, as shown in Figure 6.11 and Table 6.2. For the rigid boundary, it was similar to other experiments shown in the literature (Wilkins and Guinan, 1973). Projectiles used by Wilkins (Wilkins and Guinan, 1973) had length diameter ratio (L/D) of 3 and 6.15, and for this research, the ratio L/D was between 3.5 and 5.3. This research also extended the velocity range of the previous work. Comparing both results,

jacket and other materials surrounding the jacket have minor effects on the deformation pattern of the core.

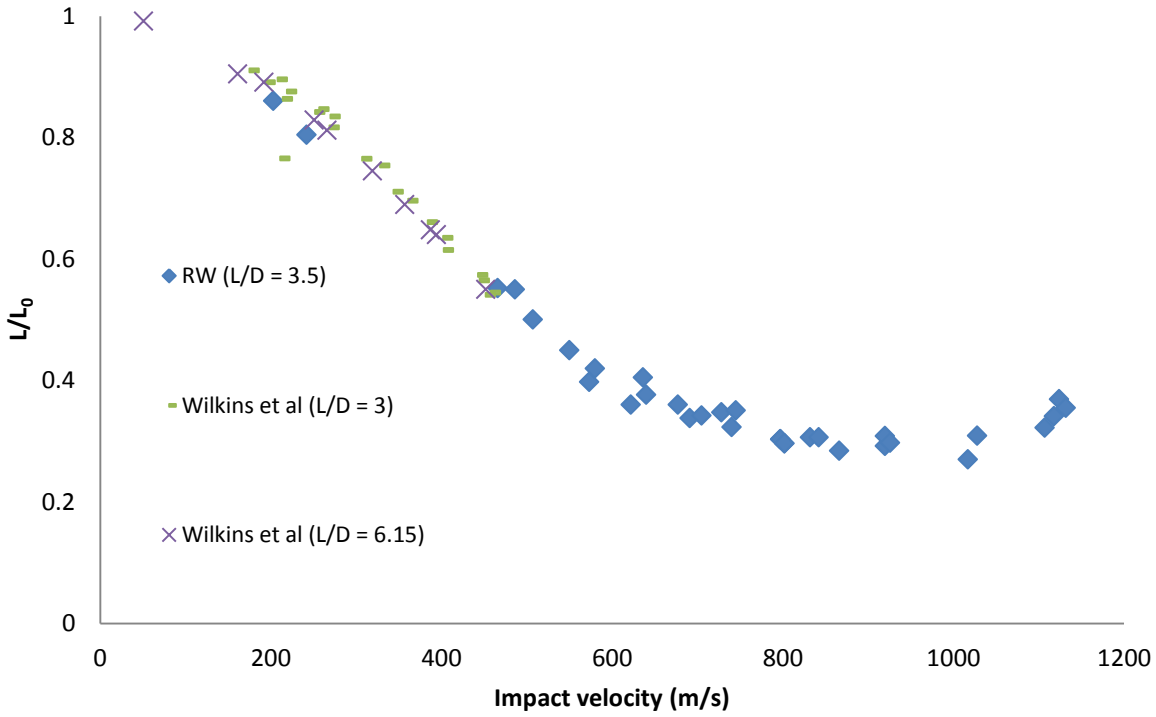

Figure 6.11.- Residual length of the core as a function of impact velocity of the projectile into the rigid wall (L/D = 3.5), and the results from literature L/D =3 and L/D=6.15 (Wilkins and Guinan, 1973).

For the rigid wall, the rate of erosion/deformation of the projectile was quite linear regarding the velocity, from 250 up to 570 m/s. The rate diminished because of the self-hardening after the chip removal (Figure 6.11). Impacts faster than 1000 m/s have a larger residual core than slower impacts, due to the partial perforation of the core into the armoured plate.

6.2 Impacts into SiC ceramic tiles

Following a similar procedure as with the steel plate, SiC ceramics tiles were tested backed with UHMWPE composite layer. The ceramic was 4.2 mm thickness SSiC. Armours were firmly clamped on the four sides using the aluminium frame. The cores of the projectiles were retrieved from the armour pack, paying particular attention to not damage or deform it during the process. Results for the silicon carbide are presented here.

The projectiles fired into the ceramic targets showed some different characteristics than the ones fired onto the rigid boundary (Figure 6.12). The projectile's jacket is not fully stripped from the core (Figure 6.13). The jacket is open in the tip and slides around the core (Strassburger et al., 2013).

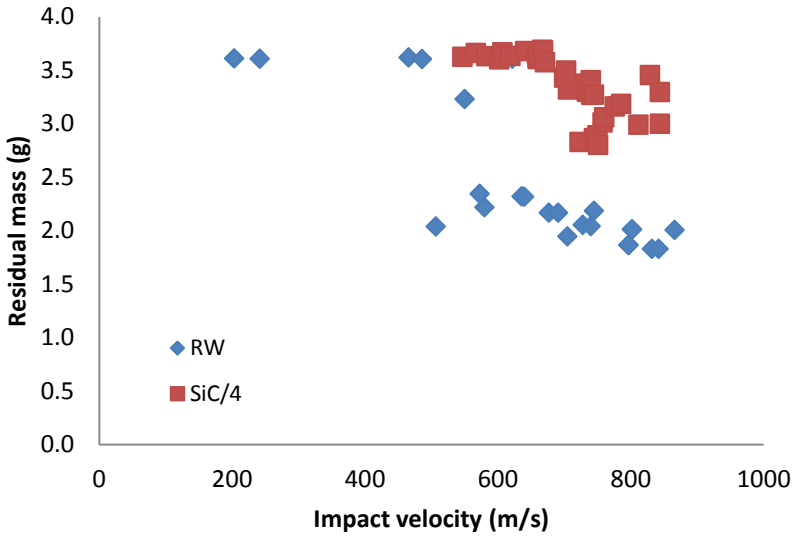

Figure 6.12.- Residual mass of the core as a function of impact velocity of the projectile into two targets: ceramic tile (SiC/4) and rigid wall (RW).

Figure 6.13.- Jacket surrounding the core after an impact.

The projectile tumbles while penetrating the target. This new orientation of the projectile makes it easier to be stopped (Figure 6.14).

Figure 6.14.- 4 mm thickness SiC postmortem tile with the tumbled core.

The ceramic tiles limit the deformation of the core. It deforms plastically in the impact zone, and the shape of the 'mushrooming' is flat. When the projectile defeats the ceramic and the penetration starts; the mushroom curves and reaches its final shape (Anderson Jr. and Walker, 2005). There is no change of diameter in the back part of the projectile core (Figure 6.15). This deformation increases the transferred energy from the projectile to the target (Bandaru and Ahmad, 2016).

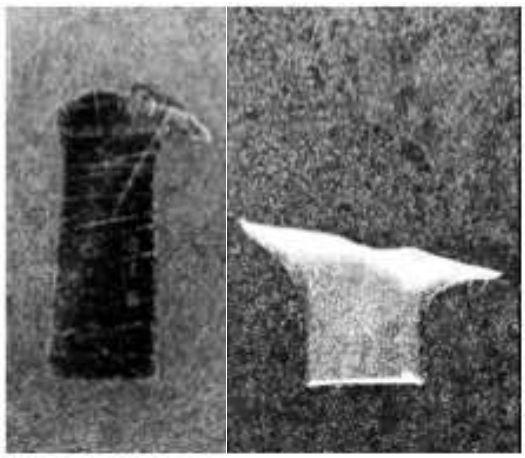

(a) (b)

Figure 6.15.- The shape of the projectile core after impact at 735 ± 5 m/s into (a) ceramic tile and (b) rigid wall.

The backing deformed and was able to stop the projectile. A CT scanner performed to the backing revealed the mechanism to stop and spread the energy. This composite layer is partially perforated, the fibres close to the strike face (upper face) and cut apart. Also, the composite is deformed, and a cone is produced. There is delamination of the layers and one of

the slides into the centre, due to the large deformation produced. The bright points are remains from the ceramic or the projectile (Figure 6.16).

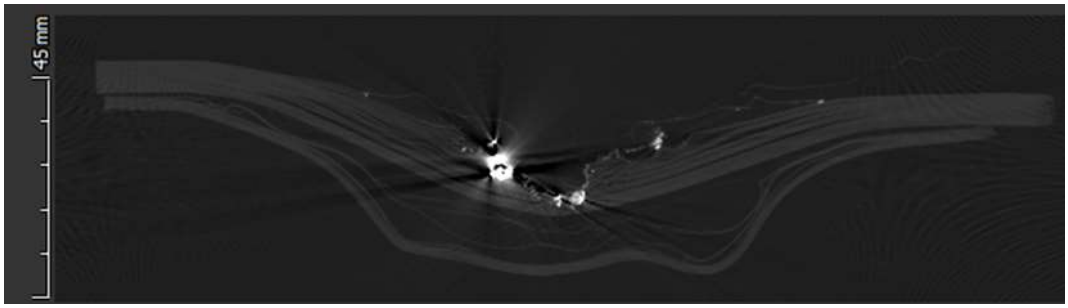

Figure 6.16.- UHMWPE backing material deformed (impact velocity 740 m/s).

By quantifying the global deformation of all projectiles cores, it is possible to evaluate the effectiveness of the armour in resisting the penetration of the core. The level of deformation and erosion was assessed by measuring the residual length as a function of impact velocity for the different targets, as shown in Figure 6.17. For the rigid boundary, it is similar to other experiments shown in the literature (Wilkins and Guinan, 1973).

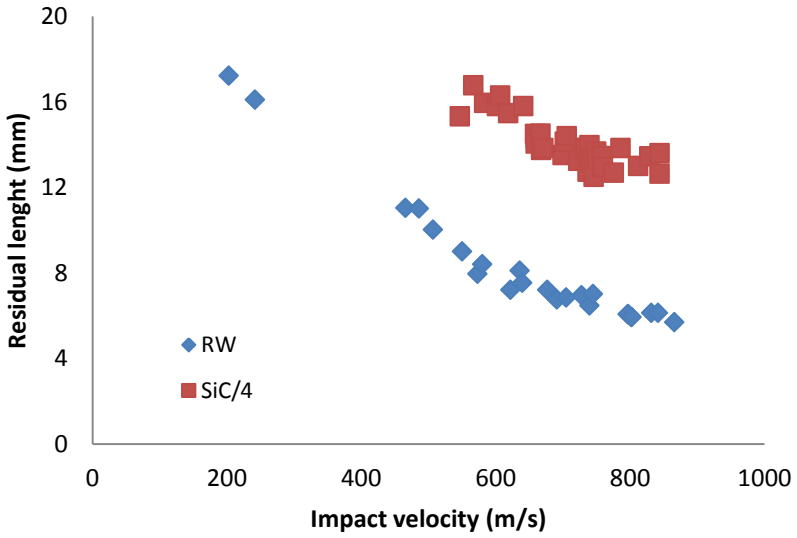

Figure 6.17.- Residual length of the core as a function of impact velocity of the projectile into two targets: ceramic tile (SiC/4) and rigid wall (RW).

A minimum of kinetic energy is needed to start the plastic deformation of the projectile, as shown in Figure 6.17, in opposition to Tang et al who propose a model where the required kinetic energy for starting the deformation of the core is null (Tang and Wen, 2017). This

value is about 150 m/s for the steel plate and about 350 m/s for the ceramic. There is nevertheless a similar rate of diminishing for the length of the core for both targets.

The tested tiles are still far of behaving as a rigid wall. The rigid steel wall is much more efficient at stopping and at deforming the projectile. The level of deformation was assessed by measuring the residual length as a function of impact velocity for the different targets, as shown in Figure 6.17. For achieving the same residual length, the rigid steel plate only needs half of the impact velocity compared to the armour assemblies with the ceramic strike face.
The rate of erosion/deformation of the projectile is quite linear regarding the velocity, up to a certain velocity. This velocity is different for the steel plate and the ceramic armour. For the steel plate, the rate of erosion/deformation diminishes at around 650 m/s; for the ceramic, at around 700 m/s (Figure 6.17). This effect points out a way to determine the optimum thickness of the ceramic to deform a projectile at a given velocity.

In Figure 6.12, a drop of the residual mass of the core appears at around 550 m/s for the steel target and 740 m/s for the ceramic armour. This shows another criterion to determine the optimum thickness of the ceramic to interact with a projectile at a given velocity. A lighter core would be easier to defeat by the composite.

There are already multiple mathematical models to optimise a ceramic faced armour (Florence and Ahrens, 1967; Tang and Wen, 2017). Florence model is meant to estimate the ballistic resistance of two-layer armour, with a hard strike face. Florence model was improved for hard core projectiles (Horsfall et al., 2000). One main parameter for this model is the angle of the fracture conoid of the ceramic. The original model estimated this value as 66°, based on experimental results regarding the fracture of glass blocks and extrapolated that value to ceramics. For the ceramic tiles of this study, the angle measurement of the fracture conoid was 44.5 grades (Figure 6.18). From the impacts, it is clear that this angle is not constant along the thickness of the tile neither along with the revolution of the section; the angle used for this formula should be an average to estimate the direct affected section of the ceramic tile. Controlled fracture of the ceramic was also obtained with a steel punch. This produced a fracture pattern following the conoid, but no ejection or further damage to the tile. This angle above is the average of several measurements in several pieces retrieved from the broken ceramic tile.

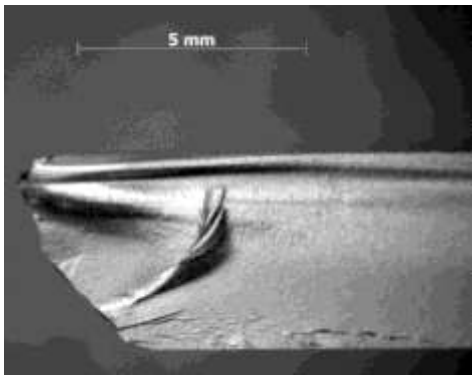

Figure 6.18.- SiC tile, angle of the fracture conoid.

The ballistic limit was estimated with the Florence model, for constant areal density and varying the thickness of the ceramic and the backing. The ballistic limit is maximized for a velocity of 753 m/s, according to the model (Figure 6.19).

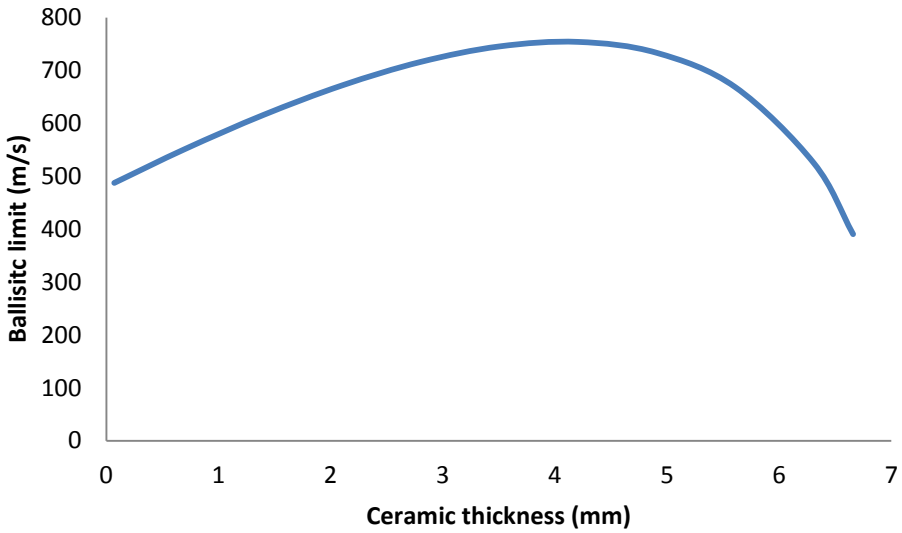

Figure 6.19.- Florence model results for a dual pack, SiC ceramic and UHMWPE.

Comparing the three criteria presented: mass reduction, length reduction and Florence model, the Florence model predicts the maximum ballistic resistance at 753 m/s, which is very close to the impact velocity when the core shatters and its weight is significantly reduced. This accuracy is due to the revision of the value of the conoid angle of the ceramic to the actual value of the ceramic.

The ceramic tiles break in several pieces due to the impact. The fracture of the ceramic shows a mirror, mist, and hackle region (Rice, 1984). The mirror region is formed during the initial

acceleration stage of propagation of the stress waves. The mist region is an annular region just outside the mirror, and the hackle region contains a set of radial striations away from the direction of the crack. In this example, the mirror region is tiny (Figure 6.20).

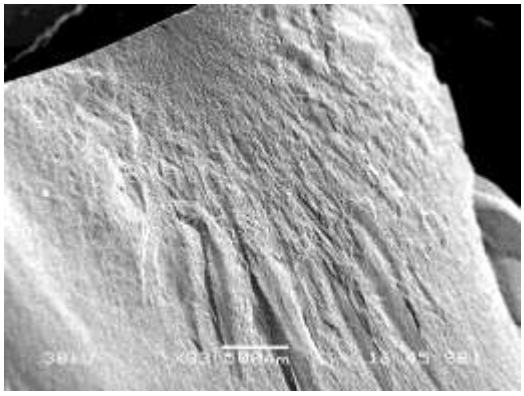

Figure 6.20.- SEM image of SiC debris.

The ceramic fragments are ejected upon an impact. After retrieving the dust, it is possible to observe two types of debris. One type is rounded and with very soft edges, totally different from the second type of debris (Figure 6.21). After analysis, the rounded fragments were shown to be made of lead, meaning that they come from the projectile. The second type of fragments comes from the ceramic tile. Particle analysis was done with "Morphologi G3", a digital system for automated high sensitivity measurement of size and shape of particles.

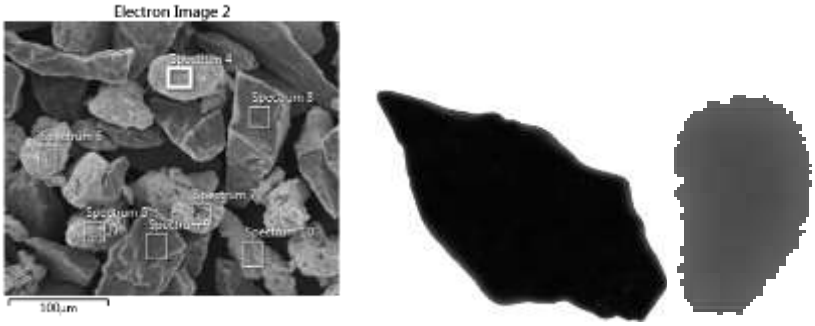

(a) (b) (c)

Figure 6.21.- Debris after the impact: (a) SEM image (b) SiC particle and (c) lead particle.

The fragments were sieved in six stages from 0.063 mm up to 2 mm diameter (Table 6.3). It is possible to estimate the energy used to fracture the ceramic tile, as the surface fracture allows estimating the energy needed for producing the fragmentation. The energy involved in the

fracture process was estimated from the value of the critical strain energy release rate (G) multiplied by the estimated surface of fracture. In all cases, this energy was less than 5 J.

Diameter (mm)		Mass (g)	Mass (%)	Particles (m^3)	Surface particle (m^2)	Surface total (m^2)
>2		7.99	36.31	1.82E+02	2.83E-05	5.15E-03
1	2	5.82	26.46	1.06E+03	7.07E-06	7.51E-03
0.5	1	3.73	16.94	5.44E+03	1.77E-06	9.62E-03
0.25	0.5	2.39	10.86	2.79E+04	4.42E-07	1.23E-02
0.125	0.25	1.33	6.06	1.25E+05	1.10E-07	1.38E-02
0.063	0.125	0.50	2.30	3.75E+05	2.78E-08	1.04E-02
	<0.063	0.235	1.07	1.39E+06	6.94E-09	9.67E-03
	TOTAL	22	100			6.85E-02

Table 6.3.- Debris size distribution after impact.

6.3 Impacts into other ceramic tiles

Four different types of ceramic were used: two grades of silicon carbide and two grades of boron carbide. Different thicknesses were available depending on the type of ceramic and grade. Relatively thin tiles were selected in order to see if thinner tiles could also give sufficient interaction with the impacting projectile. Table 6.4 shows an overview of the different ceramic tiles used during the experimental campaign. However, although one would expect the ballistic resistance to be solely defined by the ceramic type and quality; it is necessary to take in account other parameters, such as its interaction with the rest of the armour or the weight.

	Thickness (mm)	Areal density (kg/m^2)	Grade
SiC/3	3.2	9.9	SSiC
SiC/4	4.2	13.0	SSiC
SiC/5	5.0	14.5	CSiC
B_4C/3	3.9	9.4	SB_4C
B_4C/4	4.2	10.1	SB_4C

Table 6.4.- Ceramic tiles used during the experimental campaign.

Due to their inherent brittleness, ceramics have to be used in conjunction with a back face material, e.g. a composite or metal backing to support the tile. For this research, an ultra-high molecular weight polyethylene (UHMWPE) composite layer was glued to the different ceramic tiles. Its thickness was chosen in such a way, that the considered projectile was

always stopped for velocities up to 830 m/s, well above the regular nominal muzzle velocity of the projectile. Finally, a thin layer of aluminium was glued to the composite for improving the contact forces between the clamp system and the target samples. This precaution was necessary due to the low friction between the UHMWPE composite material and the metal clamp. Hence, the samples tended to slip out of the clamp system during impact. The UHMWPE material and the aluminium were sufficiently soft not to cause any further significant plastic deformation to the projectile after complete perforation of the ceramic tile. Some cores were recovered after perforating the whole armour assembly, and no significant differences were found when compared to the projectiles stopped inside the armour assembly. Impact velocities of the projectiles range between 550 and 830 m/s. Support hold firmly four sides of the armour samples. They were fired in the centre of the sample.

When compared to the different targets, the most significant deformation (at equal impact velocity) is observed for the rigid steel target (Figure 6.22). Despite the differences in areal density, hardness and material, the ceramic tiles all perform similarly, leading to similar levels of deformation of the projectile core. The core deforms plastically in the impact zone, and the shape of the 'mushrooming' is quite similar for all ceramic tiles. There is no change of diameter in the back part of it. This shape formation shows the lack of hardening during the impact event; otherwise, the core would become a thicker cylinder without the mushroom shape.

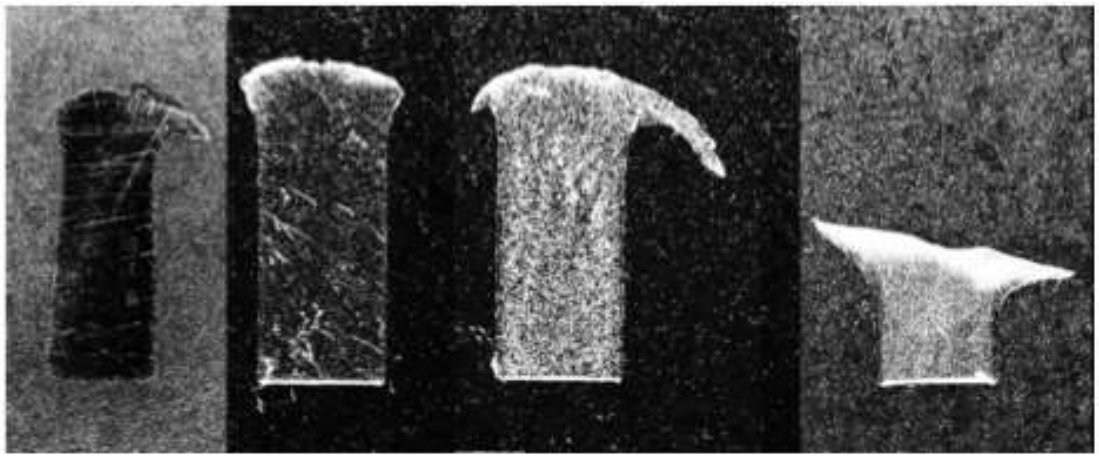

(a) (b) (c) (d)

Figure 6.22.- The shape of the projectile core after impact at 735 ± 5 m/s into different targets: (a) SiC/4; (b) B_4C/4; (c) B_4C/3; and (d) ARMOX 500.

The remaining cores from the projectiles are going to be studied and compared with others coming from projectiles retrieved from the baseline. The baseline chosen is a rigid wall made of a thick plate of ARMOX 500 steel. It is tempered steel that does not deform against this threat. When impacting a ceramic tile, the first difference is the projectiles tumble while penetrating the target. The projectile turns around 90 degrees regarding the line of fire; this new position of the projectile makes it easier to be stopped (Figure 6.14). Core of the projectile impacted into ceramic deforms less than the rigid wall and with a less flat surface due to the penetration in the ceramic, preventing the expansion of the nose part. The rigid steel wall is much more efficient at deforming the projectile. For achieving the same residual length, the rigid steel plate only needs half of the impact velocity compared to the armour assemblies with the ceramic strike face.

Contrary to the typical results for armour-piercing threats where boron carbide tiles have a higher ballistic efficiency than silicon carbide tiles (Rozenberg and Yeshurun, 1988b) and higher density grades have higher ballistic resistance (Hazell et al., 2014); the results for the ceramic tiles tested do not show any major differences between the different ceramic materials, grades or thicknesses, for projectile and velocity range studied (Figure 6.23).

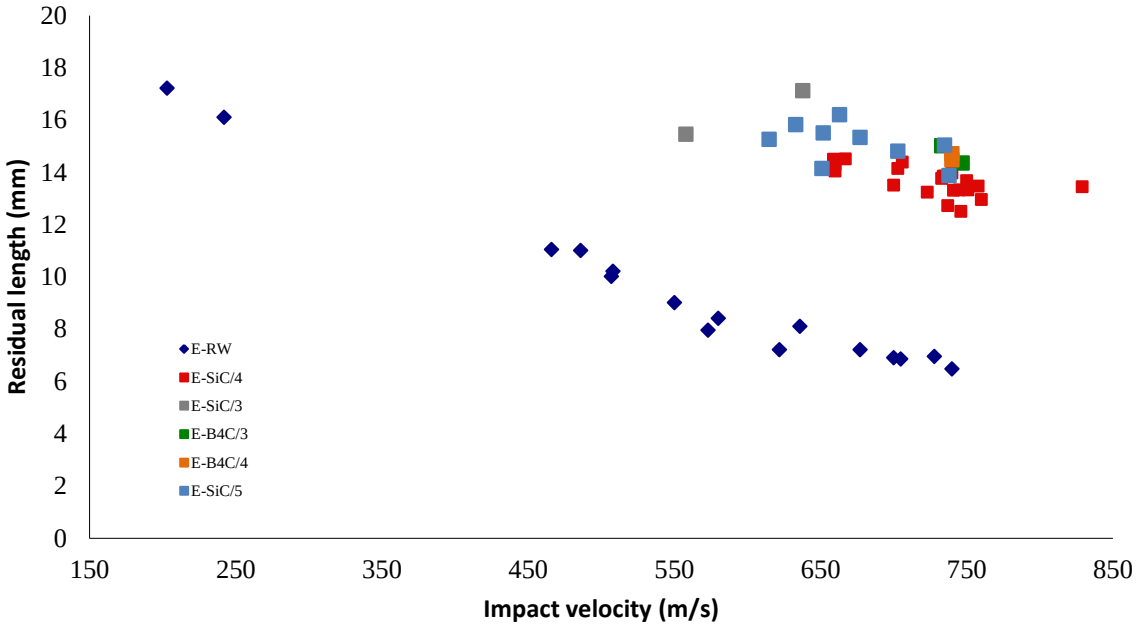

Figure 6.23.- Residual length as a function of impact velocity.

In order to detect meaningful differences in the shape of the projectile after impact, the residual mass of the projectile was also measured for each impact. The ratio residual mass over the residual length of the cores after impact as a function of residual length (or residual mass) should then be an indicator for essential differences in final geometry of the projectile (extensive mushrooming or not). As it can be seen in Figure 6.24, the value for the ratio mass over length evolves similarly among the different ceramic targets and the rigid wall. The plastic deformation of the core hence seems to be entirely independent of the target material. Despite all the different materials facing the projectiles, and the different mushrooming shapes of the core, the ratio does not seem to be affected. It shows little to no variation for all the different ceramic materials. The deformation is hence almost independent again of the various parameters tested here as thickness, areal density or hardness of the target material.

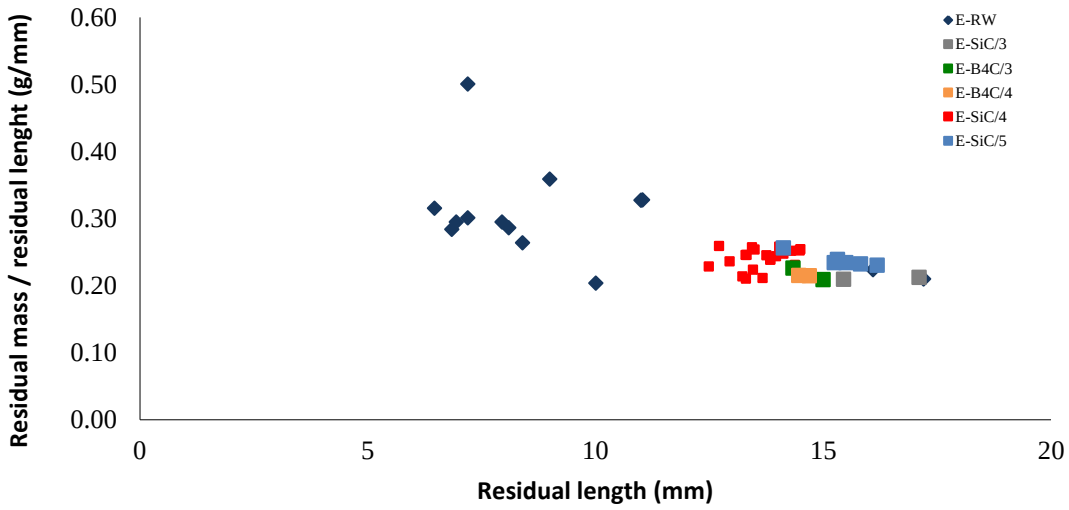

Figure 6.24.- Ratio residual mass over residual length as a function of residual length.

The plastic deformation of the mild steel core of the 7.62 x 39 mm M43 projectile was studied after impacting against different targets. The considered targets were a rigid steel wall and several relatively thin ceramic tiles. Although different ceramic materials, grades and thicknesses were tested, no significant differences were seen concerning the deformation of the projectile core for the ceramic materials. When compared to the rigid steel wall, it is immediately apparent that the tested tiles are still far of behaving as a rigid wall, possibly indicating an interest to use thicker tiles.

The fracture pattern of the ceramic tiles seems to depend on the thickness of the tile. SiC ceramic tile breaks in less parts, as seen in Figure 6.14 and Figure 6.25. For the B_4C, there is not a visual difference because the thickness of both tiles is only 0.3 mm different (Figure 6.26).

(a) 3 mm thickness.

(b) 5 mm thickness, a quarter of ceramic.

Figure 6.25.- SiC tiles after the test.

(a) 3.9 mm thickness.

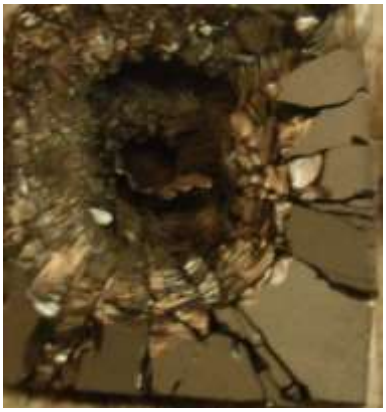

(b) 4.2 mm thickness.

Figure 6.26.- B_4C tiles after the test.

The fracture of these ceramics is mainly intergranular, as expected from a ballistic impact with some parts with intragranular fracture (Figure 6.27 and Figure 6.28),(Dateraksa et al., 2012; Medvedovski, 2010a).

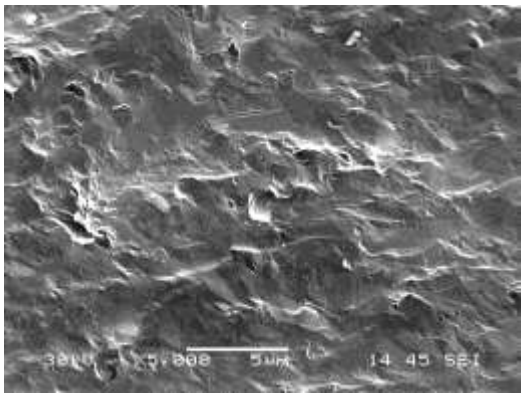

(a) B_4C.

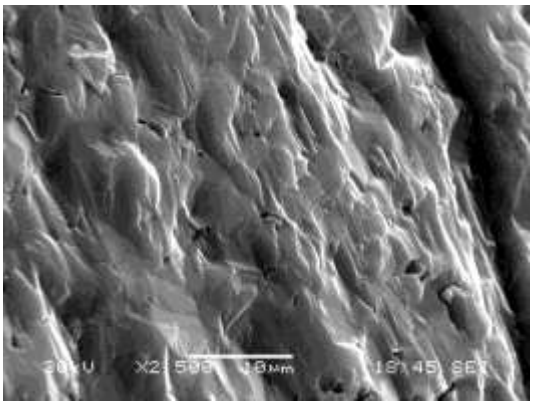

(b) SiC.

Figure 6.27.- Detail of an intergranular fracture.

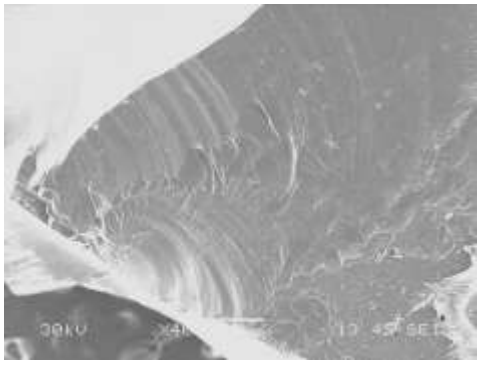

Figure 6.28.- Overview of a fracture of B_4C tile.

6.4 Add-on solutions

The protection offered by ceramic armours can be enhanced by pre-striping the jacket (Hazell et al., 2013). This effect is very useful, but it might be impossible to achieve in a portable solution placed in front of mobile armour. For removing the 7.62 x 39 mm jacket, several materials have been placed as a target with the only interest of disrupting the projectile: damaging or striping it as much as possible. In this situation, the armour behind it would have to stop a pointless and damaged jacket projectile. A secondary effect would be to deviate or destabilise the projectile, increasing the yaw angle, but it would need too much distance to be useful for a PPE. This add-on solution cannot be cumbersome because it will be placed in front of the strike face of the armour. Five metals were chosen: Ti64 1mm, brass 1mm, copper 1mm, AZ31 1mm and Ti64 1mm + Kevlar 1 ply.

Ballistic test was performed at nominal velocity. In some cases, the projectile could be recuperated (Figure 6.29). Lead core were used because it should be easier to strip the jacket.

(a) Target: Ti64.

(b) Target: AZ91.

Figure 6.29.- Projectile retrieved after test.

All the target samples have broken in a petalling pattern (Figure 6.30).

Figure 6.30.- Petalling fracture mode.

For the samples tested, the most affected projectile was the one impacted into Ti64, although it was only minor deformation. The projectile presented bizarre nose geometry (Figure 6.31.a), as the result of the jacket replicating the core geometry during the impact (Figure 6.31.b).

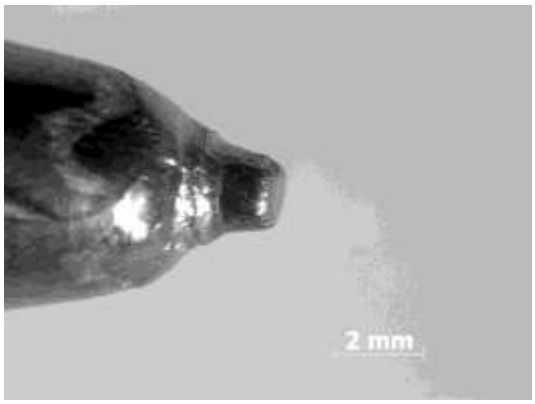

(a) Projectile after impacting Ti64. (b) Section of a projectile.

Figure 6.31.- Detail of the tip of the projectile.

The jacket of the projectile is neither broken nor striped; thus, this add-on solution will not serve to its purpose but increase the weight of the helmet. So these solutions have to be dismissed as they do not achieve any level of improvement.

6.5 Strike face

Impacting a ceramic layer produces a lot of debris and material ejected that could be a problem to people around the impact point. Covering the ceramic tile for limiting the debris expelled by the shields is vital for several reasons, like avoiding risks for the user, protecting the ceramic from low energy impacts and having and adequate material for covering it, e.g. for camouflage purpose.

Two materials were tested, a titanium layer and Dyneema layer. Both of them were 1 mm thick, and both of the configurations had the same areal density, varying the thickness of the back face accordingly (Table 6.5).

Configuratio	Materials	# samples	Deflection
A	SiC	4	Medium
B	(1mm Ti64) +SiC	4	Important/Penetration
C	(1mm HB80) +SiC	7	Medium

Table 6.5.- Covered solutions to reduce the ejection of debris.

Configuration A showed for specific velocities a characteristic pattern named Hertzian fracture in the back face (Figure 6.32). When a spherical indenter is loaded onto a flat specimen surface, cracking occurs around the circumference of the indentation mark

(Seshadri and Srinivasan, 1984). The fracture occurs in a flat specimen made by a brittle material (Frank and Lawn, 1967). The aluminium behaves as a fragile material because of the high speed of the event. The indenter is the projectile surrounded by the composite layer that pushes the material in a very local zone. Ring-and-cone crack develops along the edge of the contact circle.

Figure 6.32.- Hertzian fracture in the back face of a sample.

For configuration A, the material ejected is about 66 % of the total ceramic tile mass (Figure 6.33). In covered samples, this value drops to 6 % and has slower ejection velocities. It looks interesting to cover the ceramic, but it should introduce the fewer mass possible to the solution because it does not increment the ballistic protection of the armour.

Figure 6.33.- High-speed video of the projectile impacting configuration A, two consecutive frames after 3.09µs.

With the same areal density, configuration B performs worse than the others.

In the configuration C, there seems to be no differences in the ballistic resistance outlined. However, and similarly to configuration A, the amount of ejected material is reduced, as shown with the high-speed video (Figure 6.33 and Figure 6.34).

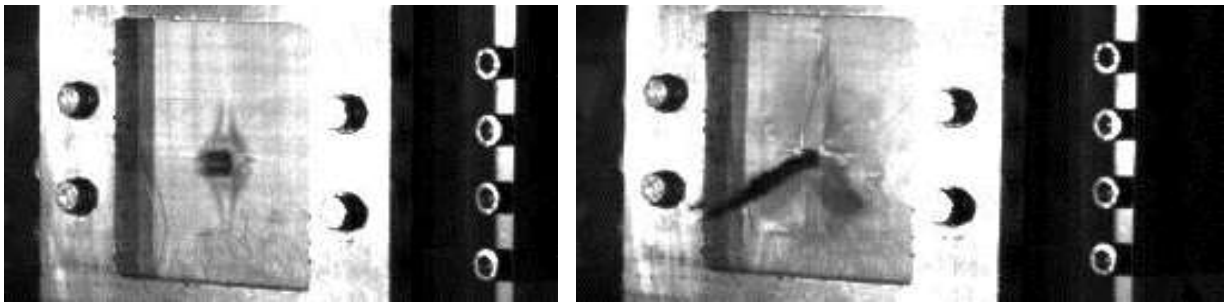

Figure 6.34.- High-speed video of the configuration C, two consecutive frames.

6.6 Optimisation of the armour pack

UHMWPE composite is able to stop the 7.62 x 39 mm M43 with an areal density of 19 kg/m^2, with a BFD of about 100 mm (Dyneema®). Florence model proposes an optimisation of dual (ceramic – composite) armours, for an areal desnity of 22.21 kg/m^2, able to defeat the threat at 740 m/s. With these details as starting points, different configuration were experimentally tested to achieve the best configuration taking in acount the areal density of the sample and BFD after the test. Up to 30 different configuration were tested, varying the thickness, materials and layup of the samples.

Several types of material in different position of the pack were tested: SSiC, SB_4C, CSiC reaction bonded silicon carbide ceramic, UHMWPE composite (orthogonal and hybrid structure), steel, aluminium, magnesium, titanium… Hybrid structures from UHMWPE composites delaminate more than the orthogonal structures upon stopping high speed projectiles.

The optimal configuration is under 26 kg/m^2, with a V_{50} of 762 m/s with a BFD average of 27.62 mm for impacts around 750 m/s (Figure 6.35 and Figure 6.36). The armour pack is done by SiC layer, orthogonal UHMWPE composite and a metal sheet. The armour is able to reach the first goal for the ballistic protection resistance objective. B_4C ceramic could be used to reduce the weight of the solution.

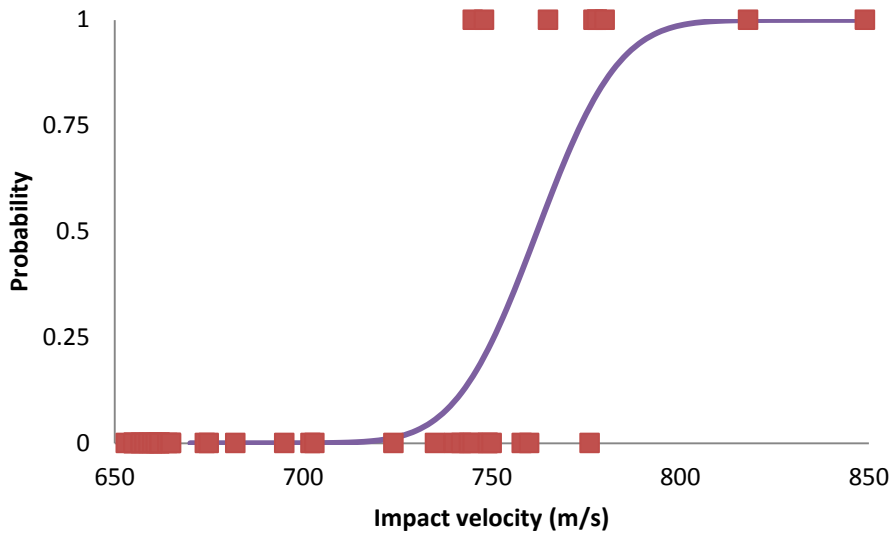

Figure 6.35.- CDF of the probability of perforation for the optimised configuration.

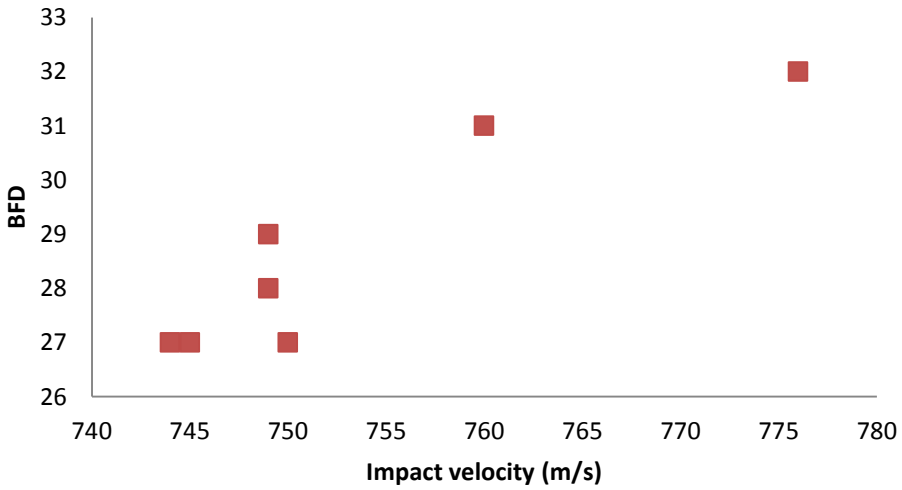

Figure 6.36.- BFD related to the impact velocity of the optimised configuration.

This optimised solution was achieved for testing samples. For a full helmet, the armour pack has to be reevaluated to take in account the curvature of the materials into the studied parameters or the inertia of the complete shell. Literature shows that these facts might reduce the BFD, reducing the total weight of the helmet (Pasquali and Gaudenzi, 2017; Tan, 2014).

6.7 Conclusions

7.62 x 39 M43 projectiles were impacted onto a thick tempered steel plate. The deformation of its steel core was studied and compared. Different fracture patterns were reported regarding

the impact velocity and the target. The metallographic analysis showed that, despite the dynamic deformation, there were only compressed grains and no recrystallisation.

Novelty of the research extends the velocity range to study the deformation of the mild steel core projectile beyond the linear behaviour. Also, it was proposed to explain the loss of material of the projectile through the theory of metal machining; it is able to explain the differences of the residual core at different impact velocities, regarding the differences of the rake angle at different velocities. It was shown that the confinement of the projectile in the crater helps to maintain its mass, and it explains the steady loss of mass at a certain velocity.

When impacted into the ceramic tile, the core needed more impact velocity to reach the same level of deformation and mass reduction compared with the rigid steel wall target. Also, thin ceramic tiles were not able to reach the same high levels of erosion/deformation as the steel plate. In any case, composite baking is needed to support the ceramic tile. Although the energy fracture of the ceramic tile is very low in comparison with the impact energy of the ballistic event, it is essential to deform the projectile and make it easier to stop.

Innovation of the research refers to the study of thin ceramics to defeat mild steel projectiles. Ceramics have been used extensively in a thicker configuration for defeating hard core projectiles. The thin configuration leads to a lightweight solution suitable for a ballistic helmet.

Projectile behaves quite differently when impacting a ceramic or a rigid wall. Main interesting conclusions are the importance of tumbling the projectile to stop it and the rake angle. Understanding and adjusting these factors may leed to lighter solutions, however this solution would most probably be useful to one single threat configuration, which means that it would be unpractical.

Although different ceramic materials, grades and thicknesses were tested, no significant differences were seen concerning the deformation of the projectile core for the ceramic materials. When compared to the rigid steel wall, the tested tiles are still far of behaving as a rigid wall, possibly indicating an interest to use thicker tiles. However, this would increase the weight of the final solution. For the different ceramics tiles, we can see that the variation of thickness does not affect the erosion of the projectile. SiC ceramic tile seems to be the most

promising regarding the erosion and reduction of the speed of the projectile. The analysis presented in this chapter was applied to different ceramic solutions; this study leads to an optimised solution regarding the weight and the BFD upon impact.

It is necessary to cover the strike face to reduce the debris cloud produced upon impact as well as give more structural cohesion to the ceramic. The cover can be adequate to have the correct colour or camouflage properties. However, it is not possible to modify heavily or disrupt the projectile with a lightweight solution in the front face.

7 STUDY OF LOAD OF THE RIFLE IMPACT

7.1 Introduction

The optimised ceramic solution studied in the previous chapter has been mounted onto the BLSH, to study the load suffered by the user upon a rifle impact. The goal is to design the liner needed for protecting the head from the deforming cone of the composite armour and to compare it with the previously determined loads for the in-service helmet.

7.2 Experimental setup

The liner is the part of the structure that accommodates the helmet onto the head. Its functions are to keep the correct standoff between the head and the shell and to assure the comfort. There are two types of liners, foam padded and strap-netting interior. They have different performance regarding heat comfort and reducing the pressure field around the head while a blast or impact event occurs. Pads allow distributing the impact forces to broader areas, reducing the load of the head user (Li et al., 2010; Salimi Jazi et al., 2012). During compression, the cells compress and fracture preventing the impulse to be transferred to the body. Foam density plays a minor role in dissipating energy. Usually, low-density foam is more effective, but with small cell size (Liaghat et al., 2010; Nasirzadeh and Sabet, 2014).

The mechanical properties of the foam and the thickness behind the surface of impact define the absorbed energy. The gap between the helmet and the head is usually around 12 mm. The kinetic energy of the 7.62 x 39 mm projectile at 660 m/s is about 1750 J. Regarding the high value of energy that can potentially reach the head; the foam should have high plateau stress. Nevertheless, this means more material, and it will occupy more room when collapsed. Once the foam is collapsed, the impact force will load the head directly. Such compaction of the foam should be avoided.

Due to the small contact surface, and the high kinetic energy, high-stress foam is needed. Plastic foams and crushable structures can reach up to 2 MPa (Aare and Kleiven, 2007), while aluminium foams are able to reach higher values of stress while keeping the density low. Due

to the capability of manufacturing different types of aluminium foam and their mechanical characteristics, this material was selected for the feasibility study.

Metallic melts can be foamed in three ways: by injecting gas from an external source, by causing an in-situ gas reaction, or by causing the precipitation of gas which was previously dissolved in the liquid. The first way is used by Hydro Aluminium in Norway and by Cymat Aluminium Corporation in Canada. The densities of aluminium foams produced this way range from 69 kg/m^3 (2.5 % nominal aluminium density) to 540 kg/cm^3 (20 % nominal aluminium density), average pore sizes from 3 up to 25 mm and wall thicknesses from 50 μm to 85 μm.

In order to check the feasibility of this concept, two aluminium foams with different densities, 135 kg/m^3 and 405 kg/m^3 (respectively 5 % and 15 % of nominal aluminium density, Figure 7.1), were tested.

Figure 7.1.- Aluminium foams, 5 % (top) and 15 % (bottom) nominal aluminium density.

For a contact surface of 5 cm radius circle, the foam was able to absorb 30 N and 300 N, respectively for 5 % and 15 % of nominal aluminium density (for a thickness of 10 mm). It is not enough to dissipate the full energy of the projectile, but the energy that reaches this layer is less than the impact energy because the armour disperses part of it.

The stress-strain graph presented in Figure 7.2 outlines the typical compressive strength of the specific materials used for this research. The area under the curve represents the energy that the foam can absorb before being crushed.

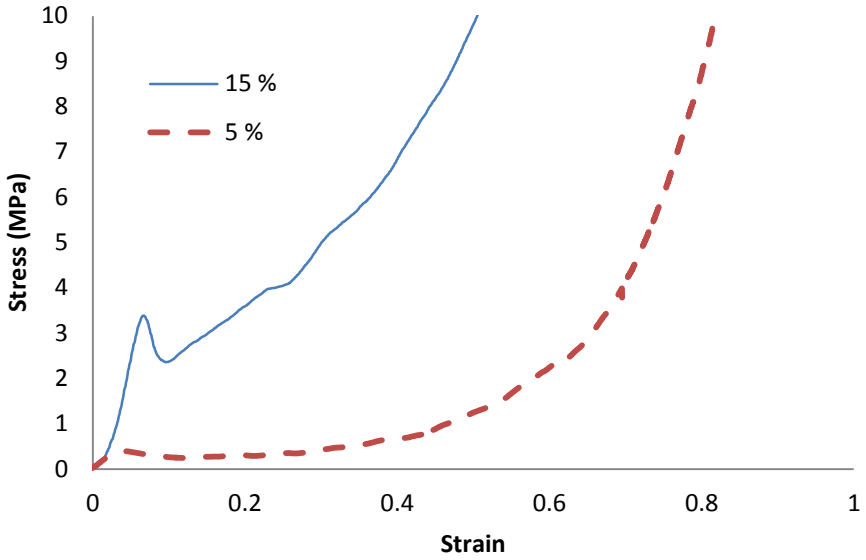

Figure 7.2.- Stress-strain curves – aluminium foams with 5 % and 15 % nominal aluminium density (CYMAT, 2009).

For a maximal force of 5000 N and a 5 % nominal aluminium density foam, as an example, depending on the affected surface, maximum absorbed energy would be 250 J with the stress of 0.7 MPa; from the Eq 10 and 12 (Figure 7.3). It means that the helmet has first to absorb more than 75 % of the kinetic energy of the projectile, muzzle energy of the 7.62 x 39 mm projectile is about 2150 J.

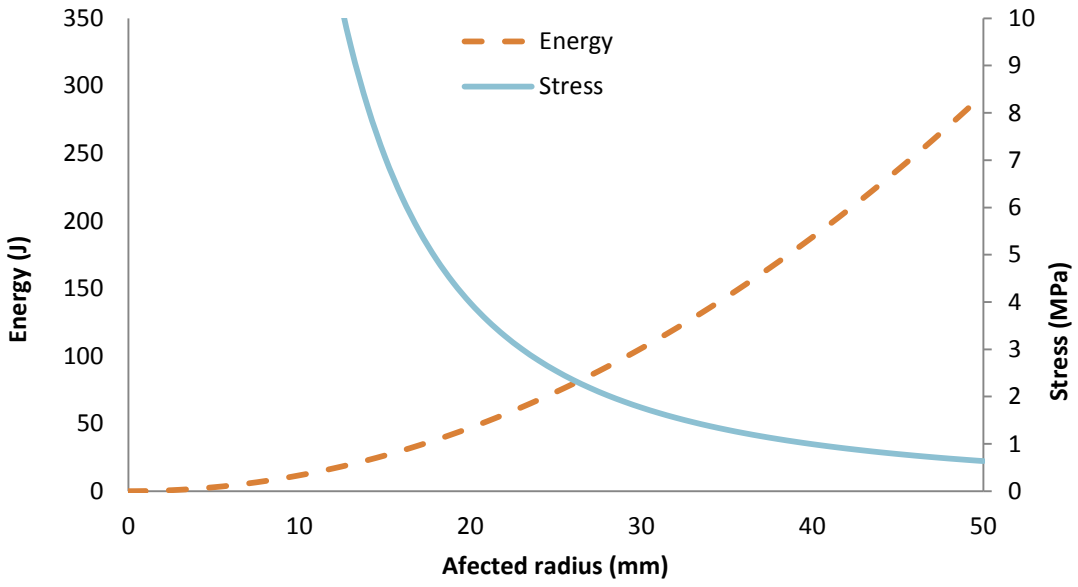

Figure 7.3.- Impact energy (J) and average stress (MPa) vs the affected surface of 5 % nominal aluminium density foam.

The larger affected surface improves the energy absorbed by the crushed layer. Still, it also implies that the average stress of the material has to be reduced, limiting the compression level of the layer.

7.3 Test procedure

First, four helmets from the Belgian Army mounted onto the BLSH were tested in order to know the actual limits and response of the system. The 9 x 19 mm projectile was fired into the helmet with a velocity ranging from 352 to 358 m/s. These are part of the results presented in the previous chapter.

Secondly, different armour configurations were tested to see the load transmitted to the head form for a rifle impact. To test the samples in the head form, support was designed to attach the samples to a regular helmet. The front part of the helmet was removed for placing flat samples. By using flat samples, the support and the manufacture of the targets are simplified. The final design of the support allowed varying the standoff between the head form and the helmet (Figure 7.4) from approximately 1.5 mm up to 50 mm. The basic configuration of the support system weighted 750 g. The test samples were shot with 7.62 x 39 mm M43 projectiles at velocities from 655 to 675 m/s. Only one shot was performed on each sample.

Figure 7.4.- Support and helmet.

Targets consisting of silicon carbide ceramic tiles backed by a composite and aluminium layer were tested. The strike face of the samples was composed of 50 x 50 mm ceramic tiles. The

ceramic tile was inserted in an aluminium frame. This frame was added to increase the level of confinement of the ceramic tiles, as the behaviour of a single small tile is different from a larger tile made out of the same material, or from an array of small tiles. Although the confinement conditions are essential (e.g. matching acoustic impedance (Savio et al., 2011b)), the addition of the aluminium frame should already partially replicate the real end-user conditions where larger tiles or arrays of tiles are used. Samples were firmly held on four sides; the support was attached with six bolts to the helmet shell. The helmet was tested for checking that it was able to support the load of the rifle projectile. A 7.62 x 39 mm projectile was fired at 745 m/s.

Due to their inherent brittleness, ceramics have to be used in conjunction with a back face material, e.g. a composite or metal backing to support the tile. For this research, an ultra-high molecular weight polyethylene (UHMWPE) composite layer was glued to the different ceramic tiles. Its thickness was chosen to always stop the considered projectile for velocities up to 675 m/s. This value is enough to achieve the secondary objective of the project. Finally, a thin layer of aluminium was glued to the composite for improving the contact forces between the clamp system and the target samples. This was a necessary precaution as otherwise, due to the low friction between the UHMWPE composite material and the metal clamp, the samples tended to slip out of the clamp system during impact. The UHMWPE presents more considerable back face deformation than other materials, like aramid. This effect will help to study the behaviour of the liner.

The target was aligned and placed on the surrogate, as explained in (National Research Center, 2014). Five different configurations were tested: the baseline armour close to the head, the baseline armour with an augmented standoff of 5 mm and 10 mm, the baseline armour with a standoff in 10 mm filled with 5 % and 15 % nominal aluminium density foam in the gap (Table 7.1).

	Number of tests	**Projectile**
Armour (Baseline)	8	7.39 x 39 mm M43
Armour + 5 mm	3	7.39 x 39 mm M43
Armour +10 mm	3	7.39 x 39 mm M43
Armour + 10 mm + 5 % AlF	3	7.39 x 39 mm M43
Armour + 10 mm + 15 % AlF	3	7.39 x 39 mm M43
Helmet	8	9 x 19 mm

Table 7.1.- Number of tests for each configuration.

7.4 Results and discussion

All the configurations were tested with rifle ammunition (Figure 7.5) and are compared to the values of an actual helmet tested with pistol ammunition (Figure 7.6). All the results have been normalised taking as a reference the first configuration, the baseline armour.

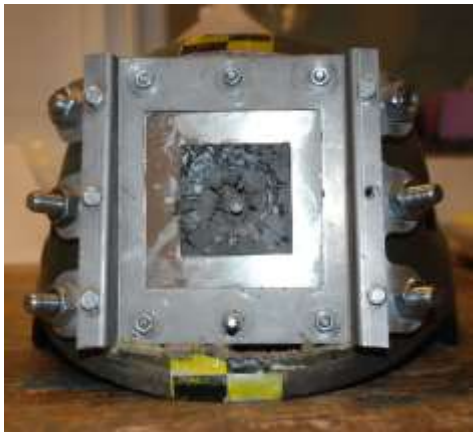

Figure 7.5.- Baseline armour configuration after rifle ammunition impact.

Figure 7.6.- Helmet after pistol ammunition impact.

The force measured by the BLSH is presented in Figure 7.7. Values are normalised for the baseline test.

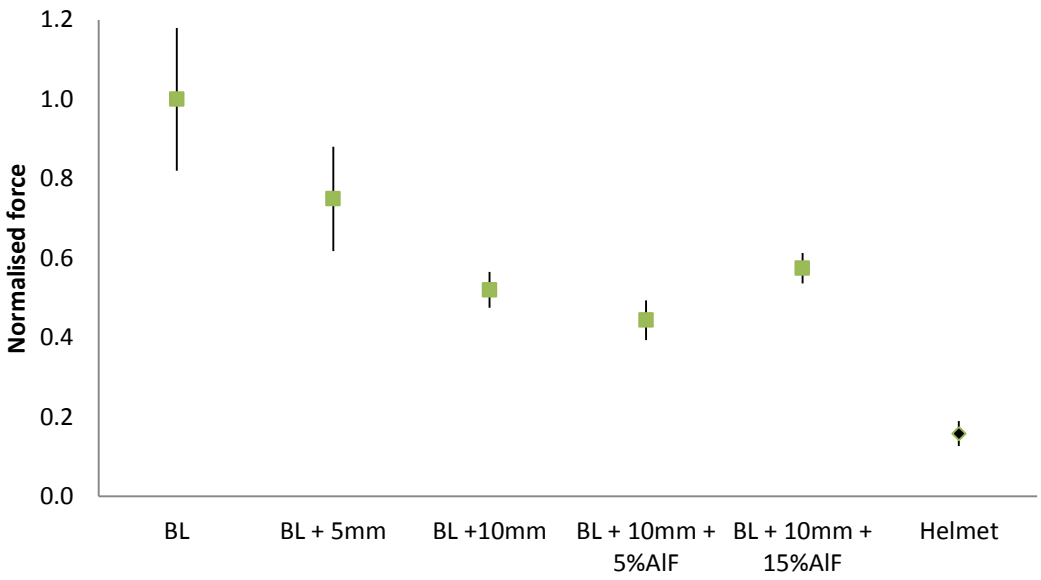

Figure 7.7.- Normalised force for the five configurations.

The load obtained with the BLSH was checked with the force measurement films, and the expected load was obtained (Figure 7.8).

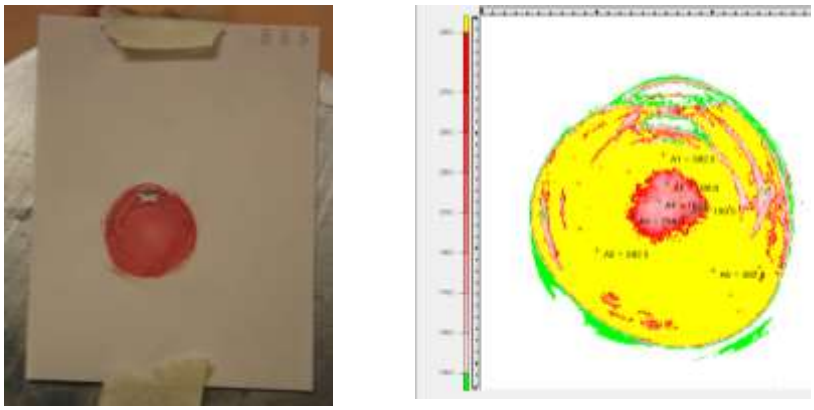

(a) Film after the test. (b) Analysis of the film.

Figure 7.8.- Pressure measurement film.

In Figure 7.7, the importance of the gap not only for thermal comfort but for ballistic protection is shown. For the baseline configuration, BC value is 4.3, which corresponds to an AIS 3. This shows the necessity to reduce it with other configurations. A gap of only 10 mm reduces the load by approximately 50 %. Increasing the gap reduces the force transmitted (Li et al., 2016). Adding 5 % nominal aluminium density reduces the forces even more, but this is not happening with 15 % nominal aluminium density. This might be because the foam collapses earlier; producing the densification of the sample and assisting in loading the head

form. Still, the total load is about three times higher than the load produced with the regular helmet against pistol ammunition.

An example of the acceleration offered by the BLSH is shown in Figure 7.9 for an impact of 9 x 19 mm ammunition into a helmet at 354 m/s. HIC is maximised for the time-lapse from 7.44 to 7.87 ms. The HIC values estimated from the BLSH are presented in Figure 7.10. Values are normalised for the baseline test.

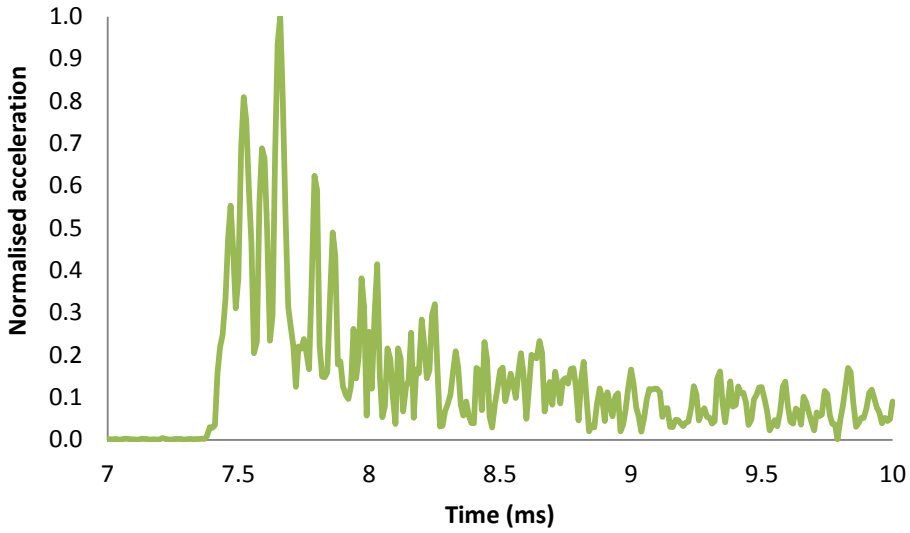

Figure 7.9.- Example of the total acceleration values normalised for an impact of 9 x 19 mm ammunition into a helmet at 354 m/s.

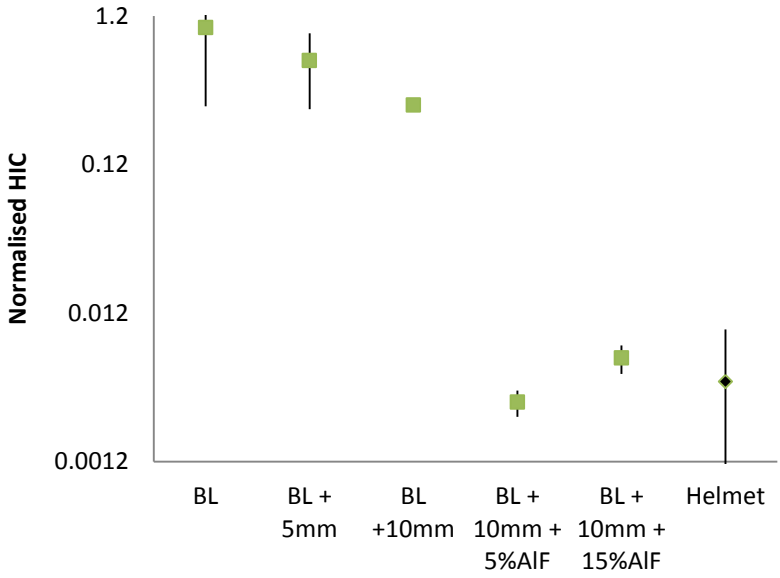

Figure 7.10.- HIC normalised.

There is a significant influence of the standoff for the acceleration of the head form, 10 mm standoff reduces about 70 % of the HIC. Unfortunately, this is not enough, and it is still a high value far away from the helmet reference. 5 % nominal aluminium density helps to reduce the HIC more effectively than the 15 % nominal aluminium density. With this material in the gap, the HIC values reach a similar level as with the helmet against pistol ammunition.

The mass of every armour and shield is critical, even more, if it is for personal protection. The estimated mass of a full helmet for each configuration tested is presented in Figure 7.11. Values are normalised for the baseline test.

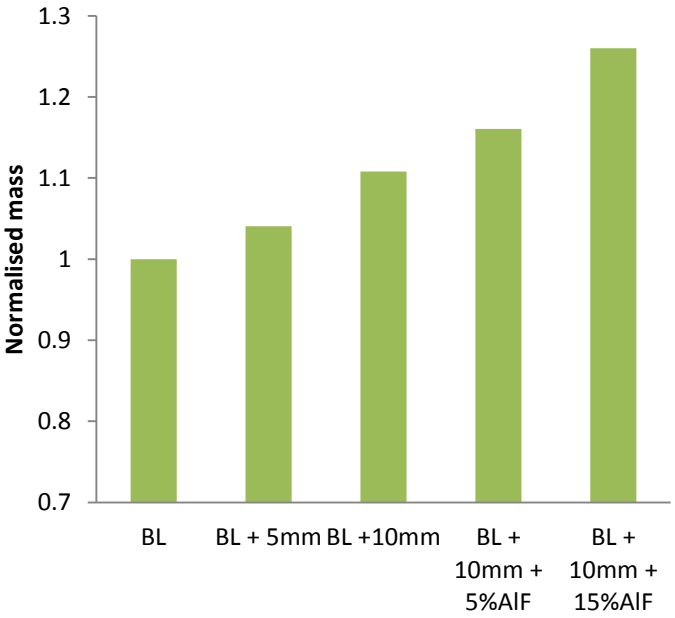

Figure 7.11.- Estimation of weight for a full helmet for each configuration, nomalised to baseline.

The disadvantage of this solution is the increase in weight, as shown in Figure 7.11. The standoff does not increase the weight in a linear ratio, because a helmet is not flat protection, but this shows that the gap should be kept as small as possible for a lightweight design.

Despite it was not an objective of this research, the fact that rifle ammunition was shot into a helmeted head form mounted on a flexible neck from the Hybrid III anthropomorphic test device allows studying the movement of the head and its influence on the neck. Neck injury

comes from tension and compression load, shear force and longitudinal bending moment (Nightingale et al., 2015). For this ballistic event, the neck might be load in compression, shear or bending moment. The tests done with pistol ammunition show almost no motion of the head form; and a movement of few mm for the tests performed with rifle ammunition. These tests indicate low risk of neck injury, despite the tests were not performed to load the neck.

7.5 Conclusions

In this study, the loads suffered by a user from two different ballistics impacts were compared. Firstly, 9 x 19 mm FMJ ammunition was impacted into a combat helmet; then the 7.62 x 39 mm ammunition threat impacted into a ceramic composite armour system. Loads of the impacts on the user were compared to study the difference between the rifle and the pistol ammunition threat. Several configurations were tested to reduce the load.

Two factors were studied for the back face of the armour, the standoff and the liner. The standoff helped to reduce the load effects on the user, and the foam reduced the acceleration suffered by the head. The 5 % nominal aluminium density performed better than the 15 % nominal aluminium density. This result opens the door to test optimised solutions of plastic structures because the suitable range of mechanical properties was determined.

Newness of this part studies a helmet liner able to deal with the load of rifle ammunition. With the correct balance between the standoff and the liner material, the new concept ballistic helmet can load a head similarly when stopping a rifle than an actual helmet does when stopping pistol ammunition. This study showed the reduction of accelerations from very high values to values similar to an actual helmet impacted with pistol ammunition. Correct loading of the skull could lead to a reduction of the thickness of the liner.

The neck is also a part to take in account when stopping powerful threats with a helmet. Experiments performed shows very little movement of the head; thus indicating very low risk of injury, if any. Despite these experiments were not done to study the risk of neck injury, the test shows that the idea of the head moving chaotically after the test is not accurate.

8 CONCLUSIONS & FUTURE WORK

In this research, a new concept helmet has been studied. It has to be able to defeat more powerful threats, rifle projectiles, with a similar mass than actual helmets. Study of ballistic impact into real helmet reveals the necessity to review the utility of the clay head form in assessing BHBT, as the BFS values have little correlation with the actual risk on injuries. It has been shown that force suffered by the user is not related to the position of the impact on the helmet, unlikely for the BFS. BFS is thus not associated with the force suffered by the user. However, the force exhibits a proportional behaviour to the velocity of the projectile, and it is possible to estimate the force with a certain probability level. Increasing the knowledge of the personal injuries threshold will improve the protection, as it will be easier to define accurate measurements when developing protection.

Throughout this research different solutions to improve the ballistic helmet and make it suitable to stop rifle ammunition were tested, and some solutions able to cope with the constraints were identified. Rake angle and confinement are some of the parameters studied to defeat the 7.62 x 39 M43 projectiles. Although they are not easy to modify, this might help to reduce the thickness of the ceramic layer in ballistic protection.

It is essential not only stopping the high-speed rifle ammunition, but on top, the survivability of the user needs to be granted. A correct layering of material and configuration was achieved to optimise the lightweight solution while keeping low the contact forces. With the correct standoff and foam properties, a helmet can overcome the defined constraints and liveable loads for the user. Loading the skull appropriately with the foam and the liner would reduce the standoff, and therefore the weight of the shell.

For the four objectives described for this project, proposed solution would cope with the primary goal for traumatic brain injury and for the ballistic protection resistance objectives. The secondary goals were achieved for the mass and skull fracture objectives. Further research could achieve a more audacious solution.

It might be remarkable to review the threat conditions, as the studied case is the worst scenario. It would be interesting to study the probability of a perfectly orthogonal impact in a

curved helmet, the distance and even to rethink the surface of the helmet. These theatre data are not available; a forensic study of each impact will help to create these statistics and adjust the requirements of the protection.

The solution herein proposed relies in large dimension ballistic grade ceramics. It is supposed that the larger the ceramic tile, the helmet would behave better than the small samples tested. Thus, the helmet built with large ceramic tiles or even one ceramic tile will weigh less than a helmet manufactured with small ceramic tiles. Therefore, it would be necessary to be able to improve the production process.

Conclusiones y trabajo futuro

Durante este proyecto de investigación, un nuevo prototipo para un casco de protección balística se ha estudiado. El requisito fundamental es mejorar la protección frente a amenazas más potentes, como es un proyectil de un rifle mientras se mantiene la masa de las soluciones actuales. El estudio de los impactos en cascos reales muestra la necesidad de revisar el criterio de la indentación en la cabeza de plastilina (BFS), usado comúnmente para mostrar el daño en la cabeza. Se ha mostrado la poca correlación entre el valor de la indentación con la velocidad de impacto del proyectil en el casco y por tanto con el posible riesgo de lesión. Se han estudiado otros parámetros, como la fuerza, la aceleración o la energía; siendo la fuerza el más útil. Esto es debido a que la fuerza está relacionada con la velocidad de impacto y es posible calcular la variabilidad y por tanto la probabilidad de alcanzar un cierto valor de carga en la cabeza. Una vez que se pueda determinar los umbrales de lesión para la cabeza, se podrá mejorar en el diseño y garantías que ofrece este tipo de protecciones.

A lo largo de la investigación, se han ensayado múltiples configuración para mejorar los cascos y adecuarlos a detener proyectiles disparados por rifles. Algunas soluciones fueron aceptadas para lograr este objetivo con las restricciones impuesta. Se estudiaron otros parámetros que influyen en el proyectil como es el ángulo de contacto entre el avance en la perforación del núcleo del proyectil o el confinamiento. Estos parámetros podrían ayudar a mejorar el diseño de las cerámicas para protección balística.

Hay que garantizar la supervivencia del usuario del casco, aunque la protección no este perforada. Se ha estudiado la solución para obtener una protección ligera y mantener las

fuerzas de contacto reducidas. Con la correcta separación entre la calota y la cabeza y el material apropiado, se puede asegurar la supervivencia del usuario. Distribuyendo las cargas apropiadamente en el cráneo, se puede obtener una solución más compacta y ligera.

De los cuatro objetivos marcados en el proyecto, se ha conseguido proponer soluciones para alcanzar el objetivo primario para los criterios de protección balística y lesión cerebral. Los objetivos secundarios fueron alcanzados para los criterios de masa de la protección y fractura craneal.

Sería interesante revisar la amenaza real, ya que el caso estudiado es el peor caso posible. Saber la distribución de probabilidad entre el ángulo del proyectil y el blanco, o la distancia podría llevar a modificar la forma de la calota. Estos datos extraídos de casos reales no están disponibles; de tal manera que un estudio pormenorizado de cada impacto real en los cascos ayudaría a conocer y ajustar los niveles de protección necesitados.

La solución propuesta se basa en gran parte en cerámicas de grado balístico, pero de pequeñas dimensiones. Cuanto más grande sea la superficie cubierta por una sola placa cerámica, mejor será la respuesta de la protección balística. Sería necesario mejorar el proceso de fabricación para grandes placas cerámicas.

9 BIBLIOGRAPHY

Aare, M., and Kleiven, S. (2007). Evaluation of head response to ballistic helmet impacts using the finite element method. Int. J. Impact Eng. *34*, 596–608.

Ackland, K., Anderson, C., and Ngo, T.D. (2013). Deformation of polyurea-coated steel plates under localised blast loading. Int. J. Impact Eng. *51*, 13–22.

Anderson Jr., C.E., and Walker, J.D. (2005). An analytical model for dwell and interface defeat. Int. J. Impact Eng. *31*, 1119–1132.

Attwood, J.P., Khaderi, S.N., Karthikeyan, K., Fleck, N.A., O′Masta, M.R., Wadley, H.N.G., and Deshpande, V.S. (2014). The out-of-plane compressive response of composites. J. Mech. Phys. Solids *70*, 200–226.

Avalle, M., Belingardi, G., and Montanini, R. (2001). Characterization of polymeric structural foams under compressive impact loading by means of energy-absorption diagram. Int. J. Impact Eng. *25*, 455–472.

Bandaru, A.K., and Ahmad, S. (2016). Modeling of progressive damage for composites under ballistic impact. Compos. Part B Eng. *93*, 75–87.

Behner, T., Heine, A., and Wickert, M. (2016). Dwell and penetration of tungsten heavy alloy long-rod penetrators impacting unconfined finite-thickness silicon carbide ceramic targets. Int. J. Impact Eng. *95*, 54–60.

Belenky, A., and Rittel, D. (2012). Static and dynamic flexural strength of 99.5% alumina: Relation to porosity. Mech. Mater. *48*, 43–55.

Ben-Dor, G., Dubinsky, A., and Elperin, T. (1999). On the order of plates providing the maximum ballistic limit velocity of a layered armor. Int. J. Impact Eng. *22*, 741–755.

Bottiglieri, S. (2012). The effect of microstructure in aluminum oxide ceramics on acoustic loss mechanisms. The State University of New Jersey. DOI: 10.7282/T3XG9Q5N

CENIEH, Computed Tomography , consulted 01/10/2019, https://www.cenieh.es/en/infrastructure/laboratories/microscopy-and-micro-computed-tomography-laboratory

CeramTec Ceramic Materials for light-weight Ceramic Polymer Armor Systems. Https://Www.ceramtec.com/Files/Et_armor_systems.pdf.

Chazot, C.A.C., and Hart, A.J. (2019). Understanding and control of interactions between carbon nanotubes and polymers for manufacturing of high-performance composite materials. Compos. Sci. Technol. *183*, 107795.

Chen, X. (2016). Advanced Fibrous Composite Materials for Ballistic Protection (Woodhead Publishing).

Chin, J., Forster, A., Clerici, C., Sung, L., Oudina, M., and Rice, K. (2007). Temperature and humidity aging of poly(p-phenylene-2,6-benzobisoxazole) fibers: Chemical and physical characterization. Polym. Degrad. Stab. *92*, 1234–1246.

Chocron, S., King, N., Bigger, R., Walker, J.D., Heisserer, U., and van der Werff, H. (2013). Impacts and Waves in Dyneema® HB80 Strips and Laminates. J. Appl. Mech. *80*, 031806–031806.

Chocron, S., Nicholls, A.E., Brill, A., Malka, A., Namir, T., Havazelet, D., Werff, H. van der, Heisserer, U., and Walker, J.D. (2014). Modeling unidirectional composites by bundling fibers into strips with experimental determination of shear and compression properties at high pressures. Compos. Sci. Technol. *101*, 32–40.

Composite World (2003). New Options In Personal Ballistic Protection, consulted 01/10/2019, https://www.compositesworld.com/articles/new-options-in-personal-ballistic-protection.

Croft, J., and Longhurst, D. (2007). Body Armour Standards for UK Police. HOSDB.

Cunniff, P.M. (1992). An Analysis of the System Effects in Woven Fabrics under Ballistic Impact. Text. Res. J. *62*, 495–509.

Cunniff, P., Vetter, E., and Sikkema, D.J. (2002). High performance "M5" fiber for ballistics structural composites. 23th Army Sci. Conf.

CYMAT (2009). Cymat - Technical Manual.

Dateraksa, K., Sujirote, K., McCuiston, R., and Atong, D. (2012). Ballistic performance of ceramic/S2-glass composite armor.

David, N. V., Sulian, A. S. and Majeed, A. P. P. A. (2011). Preliminary investigation of the impact resistance properties of a PASGT-type ballistic helmet. In 2011 International Symposium on Humanities, Science and Engineering Research, pp. 138–143.

Den Reijer, P.C. (1991). Impact on ceramic faced armour. Aerospace Engineering , TU Delft.

Dyneema® Stopping AK47 Mild Steel Core (MSC) With Dyneema® HB, consulted 01/10/2019, https://www.youtube.com/watch?v=np0AuYO3QJA

EASC (2017). GOST 34286-2017 Armored clothing. Classification and general specifications.

Eppinger, R., Sun, E., Kuppa, S., and Saul, R. (2000). Supplement: Development of Improved Injury Criteria for the Assessment of Advanced Automotive Restraint Systems – II, (NHTSA).

EUROPOL (2011). EU organised crime threat assesment (The Hage: Europol).

F. Zok, N.F. (2010). A Design Tool for Robust Composite Structures (Materials Department, University of California).

Florence, A.L., and Ahrens, T.J. (1967). Interaction of projectiles and composite armor.

Frank, F.C., and Lawn, B.R. (1967). On the Theory of Hertzian Fracture. Proc. R. Soc. Lond. Math. Phys. Eng. Sci. *299*, 291–306.

Frank, M., Bockholdt, B., Peters, D., Lange, J., Grossjohann, R., Ekkernkamp, A., and Hinz, P. (2011). Blunt Criterion trauma model for head and chest injury risk assessment of cal. 380 R and cal. 22 long blank cartridge actuated gundog retrieval devices. Forensic Sci. Int. *208*, 37–41.

Freitas, C.J., Mathis, J.T., Scott, N., Bigger, R.P., and MacKiewicz, J. (2014a). Dynamic Response Due to Behind Helmet Blunt Trauma Measured with a Human Head Surrogate. Int. J. Med. Sci. *11*, 409–425.

Freitas, C.J., Mathis, J.T., Scott, N., Bigger, R.P., and MacKiewicz, J. (2014b). Dynamic Response Due to Behind Helmet Blunt Trauma Measured with a Human Head Surrogate. Int. J. Med. Sci. *11*, 409–425.

FUJIFILM Prescale Fujifilm, consulted 01/10/2019, https://www.fujifilm.com/products/prescale/prescalefilm/

Gennarelli, T.A., and Wodzin, E. (2006). AIS 2005: A contemporary injury scale. Injury *37*, 1083–1091.

Ghajari, M., Peldschus, S., Galvanetto, U., and Iannucci, L. (2013). Effects of the presence of the body in helmet oblique impacts. Accid. Anal. Prev. *50*, 263–271.

Gobinet (2011). Significant Surpluses: Weapon and Ammunition Stockpiles in South-east europe (Geneva: Small Arms Survey).

Gorp et al (1993). A model for HPE based lightweight add-on armour. Int Symp on Ballistic.

Gotts P.L. (2015). Personal armour testing versus small arms ammunition when the test standard doesn’t fit. Probl. Mechatron. Armament Aviat. Saf. Eng.

Greenwald, R.M., Gwin, J.T., Chu, J.J., and Crisco, J.J. (2008). Head Impact Severity Measures for Evaluating Mild Traumatic Brain Injury Risk Exposure. Neurosurgery *62*, 789–798.

Grick, S.J. (1986). Helmet shell fabric layer and method of making the same.

Hamouda, A.M.S., and Hashmi, M.S.J. (1997). High speed impact of elastic-plastic work hardening material into a rigid boundary. Achiev. Mech. Mater. Eng. *64*, 189–197.

Hazell, P.J., Appleby-Thomas, G.J., Philbey, D., and Tolman, W. (2013). The effect of gilding jacket material on the penetration mechanics of a 7.62 mm armour-piercing projectile. Int. J. Impact Eng. *54*, 11–18.

Hazell, P.J., Appleby-Thomas, G.J., and Toone, S. (2014). Ballistic compaction of a confined ceramic powder by a non-deforming projectile: Experiments and simulations. Mater. Des. *56*, 943–952.

Hisley, D.M., Gurganus, J.C., and Drysdale, A.W. (2011). Experimental Methodology Using Digital Image Correlation to Assess Ballistic Helmet Blunt Trauma. J. Appl. Mech. *78*, 051022–051022.

Hogan, J.D., Farbaniec, L., Mallick, D., Domnich, V., Kuwelkar, K., Sano, T., McCauley, J.W., and Ramesh, K.T. (2017). Fragmentation of an advanced ceramic under ballistic impact: Mechanisms and microstructure. Int. J. Impact Eng. *102*, 47–54.

Holbourn, A.H.S. (1943). Originally published as Volume 2, Issue 6267 Mechanics of head injuries. The Lancet *242*, 438–441.

Holland, C.C., and McMeeking, R.M. (2015). The influence of mechanical and microstructural properties on the rate-dependent fracture strength of ceramics in uniaxial compression. Int. J. Impact Eng. *81*, 34–49.

Horsfall I., Ehsan N., and Bishop W. (2000). A comparison of the performance of various light armour piercing ammunition. J. Battlef. Technol.

Horsfall, I., Watson, C.H., and Champion, S.M. (2013). Optimizing the Stacking Sequence in Dual-Purpose Body Armors. J. Appl. Mech. *80*, 031901.

Hsieh, A.J., Chantawansri, T.L., Hu, W., Cain, J., and Yu, J.H. (2016). New insight into the influence of molecular dynamics of matrix elastomers on ballistic impact deformation in UHMWPE composites. Polymer *95*, 52–61.

Hudspeth, M., Nie, X., and Chen, W. (2012). Dynamic failure of Dyneema SK76 single fibers under biaxial shear/tension. Polymer *53*, 5568–5574.

Humpreys, F.J., and Haterly, M. (1995). Chapter 3 - The strucutre and energy of grain boundary. In Recrystallization and Related Annealing Phenomena, (Oxford: Pergamon), pp. 57–83.

ICRC (2015). War surgery: Working with limited resources in armed conflict and other situations of violence – Volume 2.

Izhevskyi, V.A., Genova, L.A., Bressiani, J.C., and Bressiani, A.H.A. (2000). Review article: silicon carbide. Structure, properties and processing. Cerâmica *46*, 4–13.

Jones, E.J.H. (1972). 21 - Negative Rake Machining. In Production Engineering (Eighth Edition), E.J.H. Jones, ed. (Newnes), pp. 258–265.

Jones, S.E., Foster, J.C., and Gillis, P.P. (1984). Impact of work-hardening cylinders on a rigid boundary. Int. J. Non-Linear Mech. *19*, 575–586.

Karthikeyan, K., Kazemahvazi, S., and Russell, B.P. (2016). Optimal fibre architecture of soft-matrix ballistic laminates. Int. J. Impact Eng. *88*, 227–237.

Karthikeyan, K., and Russell, B.P. (2014). Polyethylene ballistic laminates: Failure mechanics and interface effect. Mater. Des. *63*, 115–125.

Karthikeyan, K., Russell, B.P., Fleck, N.A., Wadley, H.N.G., and Deshpande, V.S. (2013). The effect of shear strength on the ballistic response of laminated composite plates. Eur. J. Mech. - ASolids *42*, 35–53.

Kaufmann, C., Cronin, D., Worswick, M., Pageau, G., and Beth, A. (2003). Influence of Material Properties on the Ballistic Performance of Ceramics for Personal Body Armour. Shock Vib. *10*, 51–58.

Kremkau, F.W. (2014). Sonography Principles and Instruments (Elsevier Health Sciences).

Kulkarni, S.G., Gao, X.-L., Horner, S.E., Zheng, J.Q., and David, N.V. (2013). Ballistic helmets – Their design, materials, and performance against traumatic brain injury. Compos. Struct. *101*, 313–331.

Laible Roy, C. (1972). Nonwoven fibrous felt ballistic armor material.

LaSalvia, J.C. (2015). Advances in Ceramic Armor XI: Ceramic Engineering and Science Proceedings, Volume 36 (John Wiley & Sons).

Li, J., Tan, H.-N.-S., and Seng, K.Y. (2010). A Biomechanical Computational Study of the Role of Helmet Pads in Mitigating Blast-Induced Traumatic Brain Injury. In 6th World Congress of Biomechanics (WCB 2010). August 1-6, 2010 Singapore, C.T. Lim, and J.C.H. Goh, eds. (Springer Berlin Heidelberg), pp. 1518–1521.

Li, X.G., Gao, X.-L., and Kleiven, S. (2016). Behind helmet blunt trauma induced by ballistic impact: A computational model. Int. J. Impact Eng. *91*, 56–67.

Li, Z., Wang, H., Yang, B., Sun, Y., and Huo, R. (2015). Three-dimensional graphene foams loaded with bone marrow derived mesenchymal stem cells promote skin wound healing with reduced scarring. Mater. Sci. Eng. C *57*, 181–188.

Liaghat, G.H., Nia, A.A., Daghyani, H.R., and Sadighi, M. (2010). Ballistic limit evaluation for impact of cylindrical projectiles on honeycomb panels. Thin-Walled Struct. *48*, 55–61.

Manjit Singh, D. Sood, R. Gupta, R. Kumar, P. Gautam, Bhupinder Sewak, A. Sharma, and Thomson Mathew (2008). Dynamic Yield Strength of Mild Steel under Impact Loading. Def. Sci. J. *58*.

Marjoux, D., Baumgartner, D., Deck, C., and Willinger, R. (2008). Head injury prediction capability of the HIC, HIP, SIMon and ULP criteria. Accid. Anal. Prev. *40*, 1135–1148.

Mashhadi, M., Taheri-Nassaj, E., and Sglavo, V.M. (2010). Pressureless sintering of boron carbide. Ceram. Int. *36*, 151–159.

Mauchant, D., Riley, M.A., Rice, K.D., Forster, A.L., Leber, D.D., and Samarov, D.V. (2011). Analysis of Three Different Regression Models to Estimate the Ballistic Performance of New and Environmentally Conditioned Body Armor. NIST InteragencyInternal Rep. NISTIR - 7760.

McIntosh, A., and McCrory, P. (2000). Impact energy attenuation performance of football headgear. Br. J. Sports Med. *34*, 337—341.

Medvedovski, E. (2010a). Ballistic performance of armour ceramics: Influence of design and structure. Part 1. Ceram. Int. *36*, 2103–2115.

Medvedovski, E. (2010b). Ballistic performance of armour ceramics: Influence of design and structure. Part 2. Ceram. Int. *36*, 2117–2127.

Mills, N. (2007). Chapter 21 - Rugby and soccer protection case study. In Polymer Foams Handbook, (Oxford: Butterworth-Heinemann), pp. 503–529.

Ministerio de Defensa de España (2017). NME-2815 Requisitos técnicos para la homologación del chaleco de protección balistica y anticuchillo.

Miranda-Vicario, A., Bravo, P.M., and Coghe, F. (2018). Experimental study of the deformation of a ballistic helmet impacted with pistol ammunition. Compos. Struct. *203*, 233–241.

Morye, S.S., Hine, P.J., Duckett, R.A., Carr, D.J., and Ward, I.M. (2000). Modelling of the energy absorption by polymer composites upon ballistic impact. Compos. Sci. Technol. *60*, 2631–2642.

Motherway, J.A., Verschueren, P., Van der Perre, G., Vander Sloten, J., and Gilchrist, M.D. (2009). The mechanical properties of cranial bone: The effect of loading rate and cranial sampling position. J. Biomech. *42*, 2129–2135.

N. A. (2012). Testing of Body Armor Materials: Phase III (Washington, D.C.: National Academies Press).

N.A. (1989). Real-time radiography inspection of Aramid (Kevlar) composite PASGT helmets feasibility study. NDT Int. *22*, 128.

Nasirzadeh, R., and Sabet, A.R. (2014). Study of foam density variations in composite sandwich panels under high velocity impact loading. Int. J. Impact Eng. *63*, 129–139.

National Institute of Justice (1981). NIJ Standard 0106.01 Ballistic Helmets. Law Enforc. Stand. Lab. Natl. Bur. Stand.

National Institute of Justice (1985b). NIJ Standard 0108.01 Ballistic Resistant Protective Materials. Law Enforc. Stand. Lab. Natl. Bur. Stand.

National Institute of Justice (1985a). NIJ Standard-0101.02 Ballistic Resistance of Police Body Armor. Law Enforc. Stand. Lab. Natl. Bur. Stand.

National Institute of Justice (2008). NIJ Standard-0101.06 Ballistic Resistance of Body Armor. Law Enforc. Stand. Lab. Natl. Bur. Stand.

National Research Center (2014). Review of Department of Defense Test Protocols for Combat Helmets.

NATO (1993). STANAG 4172 - 5.56 mm Ammunition.

NATO (2016). STANAG 2920 - Procedures for the evaluation and classification of personal armour- Bullets and fragmentation threats.

Nightingale, R.W., Myers, B.S., and Yoganandan, N. (2015). Neck Injury Biomechanics. In Accidental Injury: Biomechanics and Prevention, N. Yoganandan, A.M. Nahum, and J.W. Melvin, eds. (New York, NY: Springer New York), pp. 259–308.

Ohbuchi, Y., and Obikawa, T. (2005). Adiabatic shear in chip formation with negative rake angle. Int. J. Mech. Sci. *47*, 1377–1392.

Palomar, M., Lozano-Mínguez, E., Rodríguez-Millán, M., Miguélez, M.H., and Giner, E. (2018). Relevant factors in the design of composite ballistic helmets. Compos. Struct.

Palta, E., Fang, H., and Weggel, D.C. (2018). Finite element analysis of the Advanced Combat Helmet under various ballistic impacts. Int. J. Impact Eng. *112*, 125–143.

Pasquali, M., and Gaudenzi, P. (2017). Effects of curvature on high-velocity impact resistance of thin woven fabric composite targets. Compos. Struct. *160*, 349–365.

Payne, and O'Rourke (2017). Body armour Standard. Home Off.

Penn-Barwell, J.G., Sargeant, I.D., Penn-Barwell, J.G., Bennett, P.M., Fries, C.A., Kendrew, J.M., Midwinter, M., Bishop, J., Rickard, R.F., Sargeant, I.D., et al. (2016). Gun-shot injuries in UK military casualties – Features associated with wound severity. Injury *47*, 1067–1071.

Pintar, F.A., Philippens, M.M.G.M., Zhang, J., and Yoganandan, N. (2013). Methodology to determine skull bone and brain responses from ballistic helmet-to-head contact loading using experiments and finite element analysis. Med. Eng. Phys. *35*, 1682–1687.

Pittari III, J., Subhash, G., Zheng, J., Halls, V., and Jannotti, P. (2015). The rate-dependent fracture toughness of silicon carbide- and boron carbide-based ceramics. J. Eur. Ceram. Soc. *35*, 4411–4422.

Qu, G., Bai, Y., Zhang, Y., Jia, Q., Zhang, W., and Yan, B. (2009). The effect of multiwalled carbon nanotube agglomeration on their accumulation in and damage to organs in mice. Carbon *47*, 2060–2069.

Rafaels, K.A., Cutcliffe, H.C., Salzar, R.S., Davis, M., Boggess, B., Bush, B., Harris, R., Rountree, M.S., Sanderson, E., Campman, S., et al. (2015a). Injuries of the Head from Backface Deformation of Ballistic Protective Helmets Under Ballistic Impact. J. Forensic Sci. *60*, 219–225.

Rafaels, K.A., Cutcliffe, H.C., Salzar, R.S., Davis, M., Boggess, B., Bush, B., Harris, R., Rountree, M.S., Sanderson, E., Campman, S., et al. (2015b). Injuries of the Head from Backface Deformation of Ballistic Protective Helmets Under Ballistic Impact. J. Forensic Sci. *60*, 219–225.

Rahbek, D.B., Simons, J.W., Johnsen, B.B., Kobayashi, T., and Shockey, D.A. (2017). Effect of composite covering on ballistic fracture damage development in ceramic plates. Int. J. Impact Eng. *99*, 58–68.

Rammo, R.A., DeFazio, M.V., and Ross Bullock, M. (2012). Management of Migrating Intracranial Bullets: Lessons Learned from Surviving an AK-47 Bullet Through the Lateral Brainstem. World Neurosurg. *77*, 591.e19-591.e24.

Raymond, D. (2008). Biomechanics of Blunt Ballistic Temporo-parietal Head Impact (ProQuest).

Raymond, D., Van Ee, C., Crawford, G., and Bir, C. (2009). Tolerance of the skull to blunt ballistic temporo-parietal impact. J. Biomech. *42*, 2479–2485.

Rice, R.W. (1984). Ceramic fracture features, observations, mechanisms, and uses. Fractography Ceram. Met. Fail. 5–103.

Rimdusit, S., Jubsilp, C., and Tiptipakorn, S. (2013). Alloys and Composites of Polybenzoxazines: Properties and Applications (Springer Science & Business Media).

Roylance, D., Wilde, A., and Tocci, G. (1973). Ballistic Impact of Textile Structures. Text. Res. J. *43*, 34–41.

Rozenberg, Z., and Yeshurun, Y. (1988a). The relation between ballastic efficiency and compressive strength of ceramic tiles. Int. J. Impact Eng. *7*, 357–362.

Rozenberg, Z., and Yeshurun, Y. (1988b). The relation between ballastic efficiency and compressive strength of ceramic tiles. Int. J. Impact Eng. *7*, 357–362.

Sahoo, D., Deck, C., Yoganandan, N., and Willinger, R. (2015). Influence of stiffness and shape of contact surface on skull fractures and biomechanical metrics of the human head of different population underlateral impacts. Accid. Anal. Prev. *80*, 97–105.

Saint-Gobain Defense & Security | Ceramic Armor Protection, consulted 01/10/19, https://www.ceramicsrefractories.saint-gobain.com/markets/defense-security.

Salimi Jazi, M., Rezaei, A., Karami, G., Azarmi, F., and Ziejewski, M. (2012). A Study on the Impact of Helmet Padding Materials on the Brain Pressure Under Shock Loads. (ASME), p. 641.

Sapozhnikov, S.B., Kudryavtsev, O.A., and Zhikharev, M.V. (2015). Fragment ballistic performance of homogenous and hybrid thermoplastic composites. Int. J. Impact Eng. *81*, 8–16.

Savio, S.G., Ramanjaneyulu, K., Madhu, V., and Bhat, T.B. (2011a). An experimental study on ballistic performance of boron carbide tiles. Int. J. Impact Eng. *38*, 535–541.

Savio, S.G., Ramanjaneyulu, K., Madhu, V., and Bhat, T.B. (2011b). An experimental study on ballistic performance of boron carbide tiles. Int. J. Impact Eng. *38*, 535–541.

Schmitt, K.-U., Niederer, P.F., Cronin, D.S., Muser, M.H., and Walz, F. (2014). Head Injuries. In Trauma Biomechanics, (Springer Berlin Heidelberg), pp. 55–80.

Scott, B.R. (2006). 12 - New ballistic products and technologies A2 - Bhatnagar, Ashok. In Lightweight Ballistic Composites, (Woodhead Publishing), pp. 336–363.

Seshadri, S.G., and Srinivasan, M. (1984). Hertzian Fracture Testing of Ceramics. In Proceedings of the 8th Annual Conference on Composites and Advanced Ceramic Materials: Ceramic Engineering and Science Proceedings, W. Smothers, ed. (John Wiley & Sons, Inc.), pp. 583–595.

Shaktivesh, Nair, N.S., Sesha Kumar, C.V., and Naik, N.K. (2013). Ballistic impact performance of composite targets. Mater. Des. *51*, 833–846.

Sherman, D., and Brandon, D.G. (1997). The ballistic failure mechanisms and sequence in semi-infinite. supported alumina tiles. J. Mater. Res. *12*, 1335–1343.

Shin, Y., Chung, J., and Kim, J.-H. (2018). Test and estimation of ballistic armor performance for recent naval ship structural materials. Int. J. Nav. Archit. Ocean Eng. *10*, 762–781.

Siccardi, D., Cavaliere, R., Pau, A., Lubinu, F., Turtas, S., and Viale, G.L. (1991). Penetrating craniocerebral missile injuries in civilians: A retrospective analysis of 314 cases. Surg. Neurol. *35*, 455–460.

SM Group Armor Ceramic, consulted 01/10/19, http://smgroupindia.com/armor-ceramic.

Small Arms Survey (2001). Profiling the Problem (Geneva: Oxford Univresity Press Inc).

Speyer, R.F., and Lee, H. (2004). Advances in pressureless densification of boron carbide. J. Mater. Sci. *39*, 6017–6021.

Stefanopoulos, P.K., Hadjigeorgiou, G.F., Filippakis, K., and Gyftokostas, D. (2014). Gunshot wounds: A review of ballistics related to penetrating trauma. J. Acute Dis. *3*, 178–185.

Strassburger, E., Hunzinger, M., Patel, P., and McCauley, J.W. (2013). Analysis of the Fragmentation of AlON and Spinel Under Ballistic Impact. J. Appl. Mech. *80*, 031807-031807-11.

Sturdivan, L.M., Viano, D.C., and Champion, H.R. (2004). Analysis of Injury Criteria to Assess Chest and Abdominal Injury Risks in Blunt and Ballistic Impacts: J. Trauma Inj. Infect. Crit. Care *56*, 651–663.

Tan, P. (2014). Ballistic protection performance of curved armor systems with or without debondings/delaminations. Mater. Des. *64*, 25–34.

Tan, L.B., Tse, K.M., Lee, H.P., Tan, V.B.C., and Lim, S.P. (2012). Performance of an advanced combat helmet with different interior cushioning systems in ballistic impact: Experiments and finite element simulations. Int. J. Impact Eng. *50*, 99–112.

Tang, R.T., and Wen, H.M. (2017). Predicting the perforation of ceramic-faced light armors subjected to projectile impact. Int. J. Impact Eng. *102*, 55–61.

Tasdemirci, A., Tunusoglu, G., and Güden, M. (2012). The effect of the interlayer on the ballistic performance of ceramic/composite armors: Experimental and numerical study. Int. J. Impact Eng. *44*, 1–9.

Teng, X., Wierzbicki, T., Hiermaier, S., and Rohr, I. (2005). Numerical prediction of fracture in the Taylor test. Int. J. Solids Struct. *42*, 2929–2948.

Thévenot, F. (1990). Boron carbide—A comprehensive review. J. Eur. Ceram. Soc. *6*, 205–225.

Tse, K.M., Tan, L.B., Yang, B., Tan, V.B.C., and Lee, H.P. (2016). Effect of helmet liner systems and impact directions on severity of head injuries sustained in ballistic impacts: a finite element (FE) study. Med. Biol. Eng. Comput. 1–22.

Übeyli, M., Yıldırım, R.O., and Ögel, B. (2007). On the comparison of the ballistic performance of steel and laminated composite armors. Mater. Des. *28*, 1257–1262.

Vargas-Gonzalez, L.R., and Gurganus, J.C. (2015). Hybridized composite architecture for mitigation of non-penetrating ballistic trauma. Int. J. Impact Eng. *86*, 295–306.

VPAM (2009). VPAM APR 2006 General basis for ballistic material, construction and product testing.

VPAM (2010). VPAM HVN 2009 Bullet-resistant helmet with visor and neck guard.

Wetzel, E.D., Balu, R., and Beaudet, T.D. (2015). A theoretical consideration of the ballistic response of continuous graphene membranes. J. Mech. Phys. Solids *82*, 23–31.

Wilkins, M.L., and Guinan, M.W. (1973). Impact of cylinders on a rigid boundary. J. Appl. Phys. *44*, 1200–1206.

Willa, R.B. (1999). Ergonomic Prospective In The Land Warrior System - PASGT Helmet Design. US Army Cent. Health Promot. Prev. Med. DENIX.

Woolsey, P., Kokidko, D., and Mariano, S.A. (1989). Alternative Test Methodology for Ballistic Performance Ranking of Armor Ceramics.

Xue, L., Mock Jr., W., and Belytschko, T. (2010). Penetration of DH-36 steel plates with and without polyurea coating. Mech. Mater. *42*, 981–1003.

Yoganandan, N., Nahum, A.M., Melvin, J.W., and Inc, T.M.C. of W. (2014). Accidental Injury: Biomechanics and Prevention (Springer).

Zhang, T.G., Satapathy, S.S., Vargas-Gonzalez, L.R., and Walsh, S.M. (2015). Ballistic impact response of Ultra-High-Molecular-Weight Polyethylene (UHMWPE). Compos. Struct. *133*, 191–201.

Zinszner, J.L., Forquin, P., and Rossiquet, G. (2015). Experimental and numerical analysis of the dynamic fragmentation in a SiC ceramic under impact. Int. J. Impact Eng. *76*, 9–19.

(2008). Ceramics, Refractories, and Glasses. In Materials Handbook: A Concise Desktop Reference, F. Cardarelli, ed. (London: Springer London), pp. 593–689.

10 ANNEXES

Annex A: Statitical analysis of the BFS

First part of the statistical analysis is to separate the four families of impacts (regarding the impact position) to verify if they are part of the same population. For sake of comparison, data with similar impact velocity were selected to reduce the variability; their average and the standard deviation were calculated (Tables A.1 to 4):

Impact velocity (m/s)	Impact position	BFS (mm)
349	B	10.28
349	B	14.27
350	B	2.12
351	B	7.63
352	B	9.3
	MEAN	**8.7**
	STDEVP	**4.0**

Table A.1.- BFS for back position.

Impact velocity (m/s)	Impact position	BFS (mm)
347	F	4.68
350	F	10.7
351	F	10.43
355	F	13.83
	MEAN	**9.9**
	STDEVP	**3.3**

Table A.2.- BFS for front position.

Impact velocity (m/s)	Impact position	BFS (mm)
348	L	3.9
353	L	4
353	L	4.8
355	L	2.81
	MEAN	**3.9**
	STDEVP	**0.7**

Table A.3.- BFS for left position.

Impact velocity (m/s)	Impact position	BFS (mm)
345	R	5
346	R	2.01
349	R	1.85
352	R	4.9
358	R	2.1
	MEAN	**3.2**
	STDEVP	**1.5**

Table A.4.- BFS for right position.

Once the four families are characterised, they are going to be compared with a F-test of equality of variances and t-test of equality of means. Number of samples in the population is very low, and conclusions have to be reviewed with the full population.

F – tests assumes that the populations follow a normal distribution, samples have been produced randomly, and observations are independent. All of the assumptions are valid for the tests. The hypotesis to validate is whether the variance are equal for two populations. This test have to be calculated for comparing the four populations present:

H_0: $\sigma_1 = \sigma_2$

H_a: $\sigma_1 \neq \sigma_2$

For significance level of 0.10

The test statistic is

$$F = s^2_1 / s^2_2 \qquad \text{Eq A.1}$$

Rejection region: Reject H_0 if $F(\alpha / 2 , n_1 - 1 , n_2-1) < F < F(1 – \alpha / 2 , n_1 - 1 , n_2-1)$.

Probabilities for all the events are show in the table, and have to be rejected if values are smaller than the significance level (0.05) or greater than 1 - 0.05 (Table A.5).

	B	F	R	L
B	0.5	0.626	**0.978**	**0.997**
F		0.5	**0.949**	**0.994**
R			0.5	0.906
L				0.5

Table A.5.- Probability for the test statistic for all the cases.

From the table, the results show that back and left are not related, back and right are not related, front and left are not related and front and right are in the border of the significance level. It will be assumed that they are not related. Thus, front and back can be related, and left and right can be related.

Next step is to compare the two different populations to verify if they have the same mean. It will be done with a t-test. The test assumes that the population in normal and infinite, the population variance is unknown, the mean is known, observations are random and independent and the sample is small. The hypotesis to check is if the mean are equal for two populations, for all the cases front and back; and right and left:

H_0: $\mu_1 = \mu_2$
H_a: $\mu_1 \neq \mu_2$
For and significance level of 0.05

The statistic test is

$$t = \frac{\mu_1 - \mu_2}{\sqrt{\frac{s_1^2}{n_1} + \frac{s_2^2}{n_2}}} \qquad \text{Eq A.2}$$

Rejection region: Reject H_0 if $t(\alpha , n_1 + n_2\text{-}2) < t < t(1\text{-}\alpha , n_1 + n_2\text{-}2)$.
Probability for the comparison of the populations front and back is 0.68 and for the populations left and right is 0.81. Therefore, front and back can be related, and left and right can be related.

Once the populations were characterized with its normal distributions, it was possible to calculate the probability of the BFS for each specific impact; connecting and arranging each test to its percentile. Data was standardised by subtracting each point values form the expected value of the regression, and dividing it by the standard deviation of the sample, and then transformed to the standard normal distribution to calculate the Z-value. The cumulative distribution was calculated adding to each point a constant probability value (1/24, because there are 24 samples in the population). Then, the cumulative distribution calculated is

compared with the standard cumulative distribution. Comparison is very similar ($R^2 = 0.99$), it is the corroboration to assure the normal distribution of the population (Figure A.1)

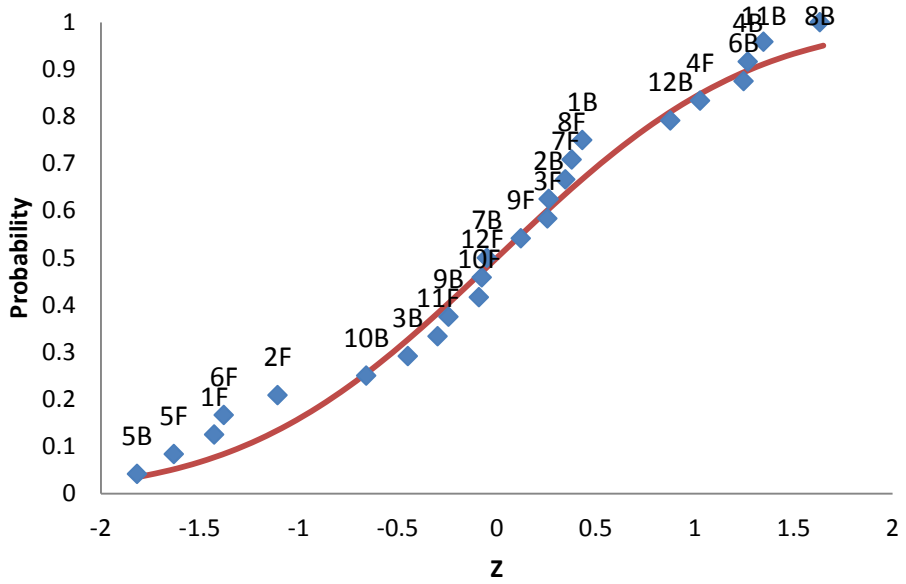

Figure A.1.- Standardised values of the BFS as a function of impact velocity for both front and back compared with the normal cumulative distribution ($R^2 = 0.99$)

Annex B: Estimation of the residual energy for the BLSH

For the estimation of the maximum residual energy reaching the head, only the projectile is going to be considered (thus, a mass of 8,5 g, even lower that the nominal 9 g to take in account the worst case scenario). This means that there is no part of the helmet involved in contact with the head form.

Helmet	Position	Velocity (m/s)	Force (N)	Impulse (N s)	Mass (kg)	Bulge velocity (m/s)	Afected radius (m)	Energy (J)
J	R	276	1545	0.7	0.0085	82		29
J	L	288	1273	0.65	0.0085	76		25
H	F	314	2970	1.06	0.0085	125		66
F	F	315	3674	1.49	0.0085	175		131
B	B	317	4098	1.36	0.0085	160		109
F	B	318	3021	0.96	0.0085	113		54
G	F	318	3038	1.19	0.0085	140		83
H	B	325	3076	1.45	0.0085	171		124
E	F	326	4525	1.39	0.0085	164		114
F	R	327	2570	1.29	0.0085	152		98
G	L	327	4169	1.61	0.0085	189		152
G	B	327	3490	1.69	0.0085	199		168
H	R	327	2143	1.13	0.0085	133		75
H	L	328	1882	0.78	0.0085	92		36
F	L	329	1763	0.88	0.0085	104		46
E	L	332	3222	1.35	0.0085	159		107
G	R	333	4829	1.8	0.0085	212		191
B	R	334	4056	1.71	0.0085	201		172
D	B	351	5344	2.06	0.0085	242		250
A	F	352	3058		0.0085			
C	B	354	3923	1.61	0.0085	189		152
J	F	354	4958	1.6	0.0085	188		151
A	B	356	2569	1.22	0.0085	144		88
B	B	356	5827	2.1	0.0085	247		259
D	F	356	3513		0.0085			
A	R	358	2634	1.13	0.0085	133		75
B	L	358	5759	1.89	0.0085	222		210
I	F	358	4117	1.54	0.0085	181		140
C	R	359	4091	1.85	0.0085	218		201
A	L	360	2031	1.02	0.0085	120		61
D	R	364	4301	1.65	0.0085	194		160
C	L	365	4240	1.79	0.0085	211		188
D	L	368	3625	1.45	0.0085	171		124
E	R	369	6047	2.15	0.0085	253		272

Table B.1.- Data of the maximum residual energy reaching the head.

For the estimation of the minimim residual energy reaching the head, the projectile plus a radius of the affected helemt of 0.029 mm is going to be considered (thus, a mass of the projectile of 9 g plus 23 g of the helmet). The radio has been chosen to be bigger than the actual contact surface of the indentation shown in clay head form (around 20 mm) .

Helmet	Position	Velocity (m/s)	Force N	Impulse (N s)	Mass (kg)	Bulge velocity (m/s)	Afected radius (m)	Energy (J)
J	R	276	1545	0.7	0.032	22	0.0292	8
J	L	288	1273	0.65	0.032	20	0.0292	7
H	F	314	2970	1.06	0.032	33	0.0292	18
F	F	315	3674	1.49	0.032	47	0.0292	35
B	B	317	4098	1.36	0.032	43	0.0292	29
F	B	318	3021	0.96	0.032	30	0.0292	14
G	F	318	3038	1.19	0.032	37	0.0292	22
H	B	325	3076	1.45	0.032	45	0.0292	33
E	F	326	4525	1.39	0.032	43	0.0292	30
F	R	327	2570	1.29	0.032	40	0.0292	26
G	L	327	4169	1.61	0.032	50	0.0292	41
G	B	327	3490	1.69	0.032	53	0.0292	45
H	R	327	2143	1.13	0.032	35	0.0292	20
H	L	328	1882	0.78	0.032	24	0.0292	10
F	L	329	1763	0.88	0.032	28	0.0292	12
E	L	332	3222	1.35	0.032	42	0.0292	28
G	R	333	4829	1.8	0.032	56	0.0292	51
B	R	334	4056	1.71	0.032	53	0.0292	46
D	B	351	5344	2.06	0.032	64	0.0292	66
A	F	352	3058		0.032			
C	B	354	3923	1.61	0.032	50	0.0024	41
J	F	354	4958	1.6	0.032	50	0.0024	40
A	B	356	2569	1.22	0.032	38	0.0024	23
B	B	356	5827	2.1	0.032	66	0.0024	69
D	F	356	3513		0.032			
A	R	358	2634	1.13	0.032	35	0.0024	20
B	L	358	5759	1.89	0.032	59	0.0024	56
I	F	358	4117	1.54	0.032	48	0.0024	37
C	R	359	4091	1.85	0.032	58	0.0024	53
A	L	360	2031	1.02	0.032	32	0.0024	16
D	R	364	4301	1.65	0.032	52	0.0024	43
C	L	365	4240	1.79	0.032	56	0.0024	50
D	L	368	3625	1.45	0.032	45	0.0024	33
E	R	369	6047	2.15	0.032	67	0.0024	72

Table B.2.- Data of the minimum residual energy reaching the head.

For the best estimation residual energy reaching the head, the CT performed to the helmet after the test is going to be considered (Figure B.1 and Figure B.2). The projectile is stopped in the second (out of nine) layer of composite; therefore, not all the mass of the affected surface of the helmet takes part in loading the head, due to the delamination. Secondly, it is going to be considered a contact surface of 0.0207 mm (thus, a mass of the projectile of 9 g plus 9 g of the helmet.) The radio has been chossen to be accordly to the clay head form. It is remarkable the small part of the helmet that actually loads the head, taking in account that the more surface engaged in this action would reduce the severity of the load. A comparison of the three estimations is made in Figure B.3.

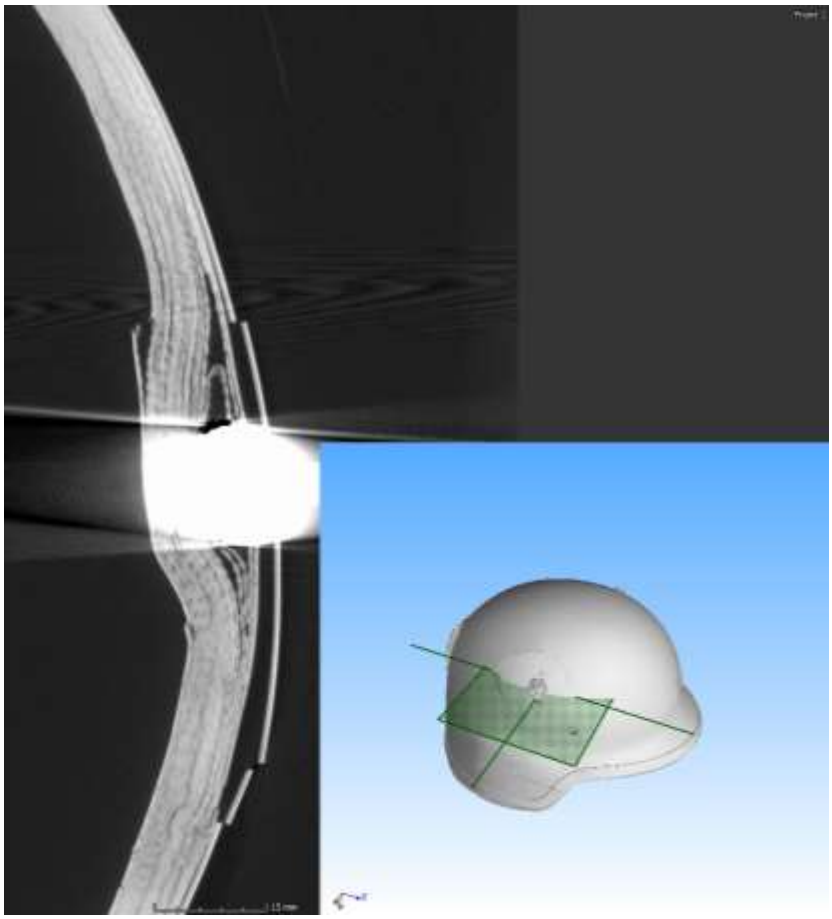

Figure B.1.- CT of a helmet impacted with 9 x 19 mm (right position)

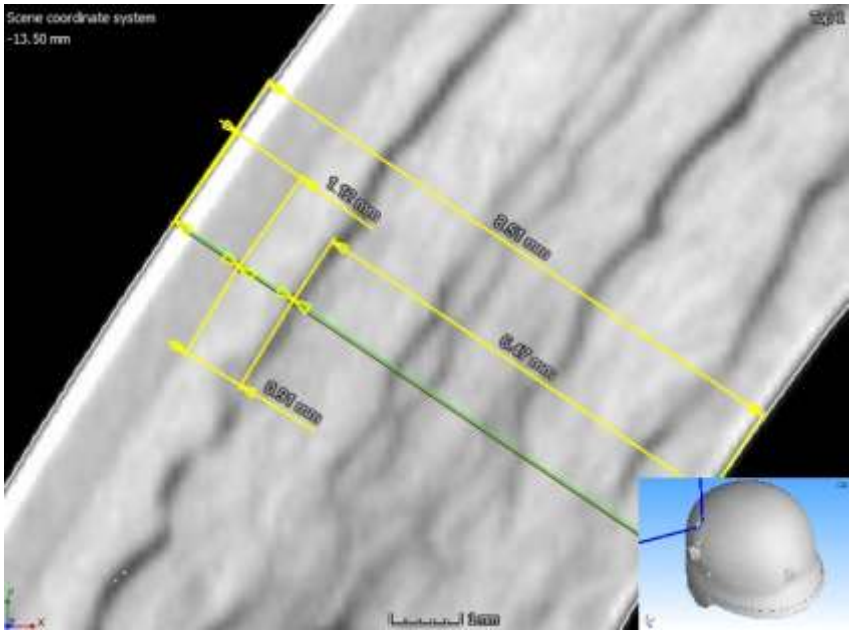

Figure B.2.- Detail of the delamination of a helmet impacted with 9 x 19 mm (right position)

Helmet	Position	Velocity (m/s)	Force N	Impulse (N s)	Mass (kg)	Bulge velocity (m/s)	Afected radius (m)	Energy (J)
J	R	276	1545	0.7	0.018	39	0.0207	14
J	L	288	1273	0.65	0.018	36	0.0207	12
H	F	314	2970	1.06	0.018	59	0.0207	31
F	F	315	3674	1.49	0.018	83	0.0207	62
B	B	317	4098	1.36	0.018	76	0.0207	51
F	B	318	3021	0.96	0.018	53	0.0207	26
G	F	318	3038	1.19	0.018	66	0.0207	39
H	B	325	3076	1.45	0.018	81	0.0207	58
E	F	326	4525	1.39	0.018	77	0.0207	54
F	R	327	2570	1.29	0.018	72	0.0207	46
G	L	327	4169	1.61	0.018	89	0.0207	72
G	B	327	3490	1.69	0.018	94	0.0207	79
H	R	327	2143	1.13	0.018	63	0.0207	35
H	L	328	1882	0.78	0.018	43	0.0207	17
F	L	329	1763	0.88	0.018	49	0.0207	22
E	L	332	3222	1.35	0.018	75	0.0207	51
G	R	333	4829	1.8	0.018	100	0.0207	90
B	R	334	4056	1.71	0.018	95	0.0207	81
D	B	351	5344	2.06	0.018	114	0.0207	118
A	F	352	3058					
C	B	354	3923	1.61	0.018	89	0.0207	72
J	F	354	4958	1.6	0.018	89	0.0207	71
A	B	356	2569	1.22	0.018	68	0.0207	41
B	B	356	5827	2.1	0.018	117	0.0207	123
D	F	356	3513					
A	R	358	2634	1.13	0.018	63	0.0207	35
B	L	358	5759	1.89	0.018	105	0.0207	99
I	F	358	4117	1.54	0.018	86	0.0207	66
C	R	359	4091	1.85	0.018	103	0.0207	95
A	L	360	2031	1.02	0.018	57	0.0207	29
D	R	364	4301	1.65	0.018	92	0.0207	76
C	L	365	4240	1.79	0.018	99	0.0207	89
D	L	368	3625	1.45	0.018	81	0.0207	58
E	R	369	6047	2.15	0.018	119	0.0207	128

Table B.3.- Data of the best estimation residual energy reaching the head.

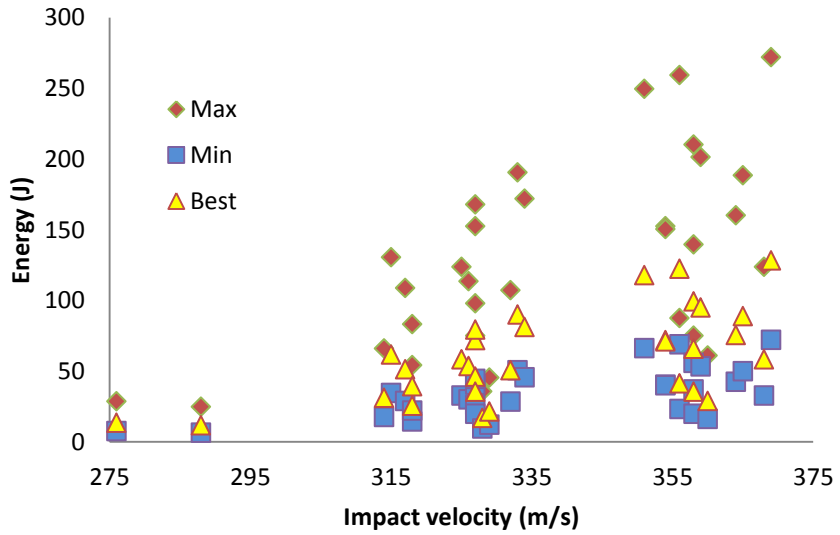

Figure B.3.- Residual energy for the three estimations.